Mechanical Properties and Thermal Stability of Nanocrystalline High-entropy Alloys

TECHNISCHE
UNIVERSITÄT
DARMSTADT

Doctoral dissertation approved by
the Department of Materials and Geosciences,
Technical University of Darmstadt
in fulfilment of the requirements for the degree of
Doktor-Ingenieurs
(Dr.-Ing.)

by
Yemao Lu
M.Sc. in Material Science and Engineering
Born on August 17, 1992 at Zhongxiang, Hubei, China
Referee: Prof. Dr. -Ing. Horst Hahn
Co-referee: Prof. Dr. rer. nat Christian Kübel
Date of submission: 23.01.2023
Date of oral exam: 22.05.2023

Yemao Lu: Mechanical Properties and Thermal Stability of Nanocrystalline High-entropy Alloys

Darmstadt, Technische Universität Darmstadt

Year thesis published in TUprints 2023

Date of the viva voce 22.05.2023

Published under CC BY-SA 4.0 International

https://creativecommons.org/licenses/

Erklärung zur Dissertation

Hiermit versichere ich, dass ich meine Dissertation selbständig und nur mit den angegebenen Quellen und Hilfsmitteln angefertigt habe. Die Arbeit wurde bisher keiner anderen Prüfungsbehörde vorgelegt und noch nicht veröffentlicht.

Karlsruhe, 12.12.2022
Yemao Lu

Abstract

High entropy alloys (HEAs) have been the subject of numerous investigations during past 20 years. Various alloy systems have been explored to identify HEA systems with improved property combinations, leading to an extraordinary growth of this field. Equiatomic single face-centered cubic (FCC) structured CoCrFeMnNi alloy, also known as Cantor alloy, has attracted increased attention in the past decades largely because of its excellent mechanical properties. The most remarkable feature of this alloy is the superior combination of ductility and strength at cryogenic temperatures in comparison with that at room temperature, especially in a fine-grained state. Generally, CoCrFeMnNi alloy exhibits a dramatic ductility and strong work hardening performance at cryogenic temperature but lacks comparable strength.

To improve the strength, CoCrFeMnNi alloys with reduced Cr content and with the addition of different contents of carbon as interstitial impurity were synthesized for following study. High-pressure torsion (HPT) process, as the most effective severe plastic deformation (SPD) method, was performed to obtain nanocrystalline HEAs. Meanwhile, the evolution of microstructure and hardness was investigated during HPT process. Subsequently, the mechanical properties were analyzed in specimen with saturated microstructure. Based on electron microscopy characterization, the microstructure and composition fluctuation were investigated on the nanocrystalline HEAs. The results indicated that carbon interstitial alloying significantly promoted the grain refinement, dislocation density increase, improvement of yield strength and the carbon segregation at the grain boundaries. Herein, the mechanism of the grain fragmentation, deformation behavior and strengthening and fracture mechanisms were discussed in the following chapters. The C segregation behavior during HPT at room and cryogenic temperature were studied in detail. The results of this work could be a good reference for the production of high strength HEAs using SPD methods.

Post deformation annealing has been used in SPD processed alloys to gain comprehensive performance avoiding the brittle fracture. Hence, the exploration of thermal stability of the C alloyed nanocrystalline HEAs is essential to promote the improvement of the mechanical properties. Using electron microscopy, the elemental segregation, nucleation of precipitates, decomposition of matrix phase decomposition and grain growth were illustrated after annealing at different temperature. The results suggested that the single FCC phase nanocrystalline HEA is thermally stable up to 400 °C. Significant co-segregation of alloy constituent elements and precipitation occur from 500 to 600 °C. New phases such as CoFe B2 phase, NiMn FCC phase and M_7C_3 carbides formed during the annealing at the medium temperature interval from 500 to 600 °C. The development of the precipitation process and the effect of precipitates on the mechanical properties are unveiled in following chapters. Consequently, the results in the present work optimized the current inference on the thermal stability of nanocrystalline HEAs and proposed a theoretical model for the precipitation process.

Zusammenfassung

Hochentropie-Legierungen (HEAs) waren in den letzten 20 Jahren Gegenstand zahlreicher Untersuchungen. Es wurden verschiedene Legierungssysteme erforscht, um HEA-Systeme mit verbesserten Eigenschaftskombinationen zu identifizieren, was zu einem außerordentlichen Wachstum dieses Bereichs führte. Die CoCrFeMnNi-Legierung mit äquiatomarer, kubisch-flächenzentrierter (FCC) Struktur, die auch als Cantor-Legierung bekannt ist, hat in den letzten Jahrzehnten vor allem wegen ihrer hervorragenden mechanischen Eigenschaften große Aufmerksamkeit auf sich gezogen. Das bemerkenswerteste Merkmal dieser Legierung ist die überlegene Kombination aus Duktilität und Festigkeit bei kryogenen Temperaturen im Vergleich zu Raumtemperatur, insbesondere im feinkörnigen Zustand. Im Allgemeinen weist die CoCrFeMnNi-Legierung eine dramatische Duktilität und eine starke Kaltverfestigung auf, vor allem bei kryogenen Temperaturen, aber es fehlt ihr an vergleichbarer Festigkeit.

Um die Festigkeit zu verbessern, wurden für die folgende Studie CoCrFeMnNi-Legierungen mit reduziertem Cr-Gehalt und mit unterschiedlichen Gehalten an interstitiellem C synthetisiert. Das Hochdruck-Torsionsverfahren (HPT), die effektivste Methode der schweren plastischen Verformung (SPD), wurde an den Versuchslegierungen durchgeführt, um nanokristalline HEAs zu erhalten. Währenddessen wurden die Mikrostruktur und die Härteentwicklung im laufe des HPT-Prozesses untersucht, und im Anschluss weitere mechanische Eigenschaften. Anhand der elektronenmikroskopischen Charakterisierung wurden die Mikrostruktur und die Schwankungen der Zusammensetzung der nanokristallinen HEAs untersucht. Die Ergebnisse zeigten, dass die interstitielle C-Legierung die Kornverfeinerung, die Erhöhung der Versetzungsdichte, die Verbesserung der Zugfestigkeit und die C-Segregation an den nanokristallinen Korngrenzen erheblich fördert. Die Mechanismen der Kornfragmentierung, des Bruchs und der Verfestigung wurden in den folgenden Kapiteln diskutiert. Das C-Segregationsverhalten während der HPT bei Raum- und Tiefsttemperatur wurde im Detail untersucht. Die Ergebnisse dieser Arbeit könnten eine gute Referenz für die Herstellung hochfester Legierungen mit SPD-Methoden sein.

Das Glühen nach der Verformung ist bei SPD-verarbeiteten Legierungen üblich, um eine verbesserte Leistung zu erzielen und Sprödbrüche zu vermeiden. Daher ist die Erforschung der thermischen Stabilität der C-legierten nanokristallinen HEAs für die Verbesserung der mechanischen Eigenschaften sehr bedeutend. Durch elektronenmikroskopische Untersuchungen wurden die Entmischung der Elemente, die Keimbildung von Ausscheidungen, die Zersetzung der Matrixphase und das Kornwachstum nach dem Glühen in einem breiten Temperaturintervall veranschaulicht. Die Ergebnisse deuten darauf hin, dass die nanokristalline Hochentropie-Legierungen in einer FCC-Phase bis 400 °C thermisch stabil ist. Zwischen 500 und 600 °C kommt es zur Ausscheidung von sekundären Phasen und

Bildung von Korngrenzenssegregationen. In diesem Temperaturintervall bildeten sich neue Phasen, wie die CoFe B2-Phase, die NiMn FCC-Phase und M_7C_3-Karbid. Die Entwicklung der phasen und die Auswirkungen auf die mechanischen Eigenschaften durch die zahlreichen Ausscheidungen werden in den folgenden Kapiteln vorgestellt. Infolgedessen optimierten die Ergebnisse der vorliegenden Arbeit die derzeitigen Erkenntnisse über die thermische Stabilität von nanokristallinen HEAs und schlagen ein theoretisches Modell für den Ausscheidungsprozess vor.

Contents

Abstract III

1 Introduction 1

2 Fundamentals 5

- 2.1 High entropy alloys characteristics 5
- 2.2 Mechanical properties of FCC HEAs 7
  - 2.2.1 Solid solution effect 8
  - 2.2.2 Grain size effect (Hall-Petch in HEAs) 10
  - 2.2.3 Dislocation effect 12
  - 2.2.4 Precipitation effect 13
  - 2.2.5 Deformation twinning effect 16
- 2.3 Severe plastic deformation on HEAs 17
  - 2.3.1 SPD methods 17
  - 2.3.2 Microstructure refinement mechanism at SPD 22
  - 2.3.3 Influence of various factors on grain refinement by SPD 27
- 2.4 Nanocrystalline HEAs 29
  - 2.4.1 Deformation behavior in nanocrystalline state 29
  - 2.4.2 Thermal stability of nanocrystalline HEAs 32
- 2.5 Motivation and objectives 34

3 Experimental 38

- 3.1 Experimental material 38
  - 3.1.1 Materials synthesis 38
  - 3.1.2 HPT process 38
  - 3.1.3 Post deformation anneal 39
- 3.2 Characterizations 40
  - 3.2.1 Sample preparations 40
  - 3.2.2 X-ray diffraction 41
  - 3.2.3 Scanning Electron Microscopy 41
  - 3.2.4 Transmission Electron Microscopy 42
  - 3.2.5 Atom Probe Tomography 48
- 3.3 Mechanical test 52
  - 3.3.1 Microhardness 52

3.3.2 Tensile test 52

4 Influence of carbon alloying on the microstructure evolution of CoCrFeMnNi HEA processed by high pressure torsion at room and cryogenic temperatures 54

4.1 Materials and experimental methods 54

4.2 Results 55

4.2.1 Microstructures of C-alloyed HEAs before HPT 55

4.2.2 Microstructures evolution of C-HEAs during HPT at RT 57

4.2.3 Comparison of saturation microstructures of C2N3 alloy deformed at room and liquid nitrogen temperature 63

4.3 Discussion 66

4.3.1 Mechanisms of grain refinement and carbide dissolution 66

4.3.2 Carbon segregation behavior at room and liquid nitrogen temperature 68

4.4 Conclusions 71

5 Thermal stability of nanocrystalline carbon alloyed high entropy alloy 72

5.1 Materials and experimental methods 72

5.2 Results 73

5.2.1 Microstructures after heat treatment at different temperatures 73

5.2.2 FCC phase decomposition during annealing 73

5.2.3 Characterization of precipitate structures 82

5.3 Discussion 84

5.3.1 The elemental segregation and formation of the precipitate after annealing 84

5.3.2 Elements segregation and new phase nucleation process during the annealing 85

5.4 Conclusions 89

6 Mechanical properties of nanocrystalline carbon alloyed high entropy alloys 90

6.1 Materials and experimental methods 90

6.2 Results 90

6.2.1 Mechanical properties of HPT deformed nanocrystalline HEAs with carbon additions 90

6.2.2 Mechanical properties of annealed nanocrystalline 2 at. % C-HEAs 93

6.3 Discussion 95

6.3.1 Strengthening mechanisms in nanostructured CxN3 HEAs 95

6.3.2 Heat treatments effect on strengthening of C2N3 HEA 99

6.4 Conclusions 102

7 Summary and outlook 104
7.1 Summary 104
7.2 Outlook 105
List of Figures 106
List of Tables 110
List of abbreviations 111
References 113
Curriculum Vitae 125
List publications 126
Acknowledgements 127

1 Introduction

Since the Bronze Age, human beings have been altering the properties of metallic materials by forging and adding alloying elements. For example, the bronze sword of Goujian is renowned for its unusual sharpness, intricate design and remarkable corrosion resistance [1]. This blade still keeps sharp and tough even though it is around 2500 years old. At modern era, iron and steels are widely used in all industrial fields. Subsequently, elements such as carbon, chromium, and nickel are added for strength and corrosion resistance, respectively. Nowadays, according to the basic alloying method of adding relatively less amount of other elements to a primary element, the alloys are divided into different categories: magnesium alloys, aluminum alloys, ferrous alloys, titanium alloys and so on.

However, in the past twenty years, a new approach based on mixing multiple principal elements has been suggested, which stands in strong contrast with traditional ways. Jien-Wei Jeh and co-authors have introduced the concept of High Entropy alloys (HEAs) in 2004 [2] where they proposed the increased entropy of mixing as a possible reason for solid solution stability in multi-principal element alloys. They gave a definition of HEAs as follows: High entropy alloys are composed of five or more principal elements whose concentration are between 5 and 35%. According to the Boltzmann's hypothesis on the relationship between entropy and system complexity [3], completely utilizing the advantage of high mixing entropy in liquid state one can obtain alloys with highly uniform composition. Therefore, a simplified problem is that all the considered solid solution are ideal. In this case, the ideal entropy of mixing is given by the equation:

$$\Delta S_{mix} = -\mathrm{R}\Sigma x_i \ln x_i \tag{1.1}$$

where R is the gas constant and x_i is the mole fraction of the i^{th} element. When the compositions of the alloys are equiatomic, $x_1 = x_2 = x_3$ and so on. Then the equation can be simplified to:

$$\Delta S_{mix} = \mathrm{R}\ln n \tag{1.2}$$

where n is the number of elements in the alloy. For instance, ΔS_{mix} for equiatomic alloys with 3, 4, 5 and 6 elements are 1.10R, 1.39R, 1.61R and 1.79R, respectively. Therefore, Yeh divided all alloys into three groups according to the ΔS_{mix} value. 1R is recommended as a borderline for medium and low entropy alloys while 1.5R is recommended for a borderline between high and medium entropy alloys (MEAs) [4]. Based on the definition, some typical alloys are schematically shown in Figure 1.1.

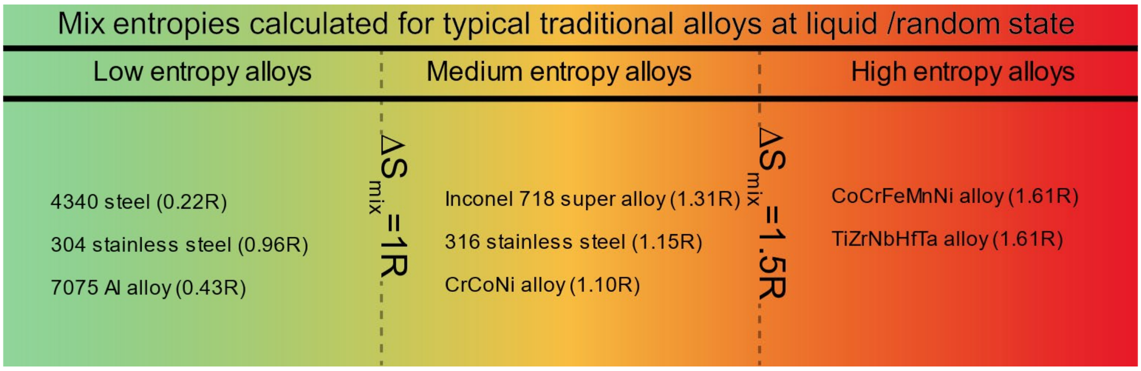
Mix entropies calculated for typical traditional alloys at liquid /random state
Low entropy alloys
Medium entropy alloys
High entropy alloys
ΔS mix =1R
ΔS mix =1.5R
4340 steel (0.22R)
304 stainless steel (0.96R)
7075 Al alloy (0.43R)
Inconel 718 super alloy (1.31R)
316 stainless steel (1.15R)
CrCoNi alloy (1.10R)
CoCrFeMnNi alloy (1.61R)
TiZrNbHfTa alloy (1.61R)

Figure 1.1 Configurational entropies calculated for typical alloys at random state [5].

Due to the ambiguity in the definition of HEAs, some researchers prefer other terms such as multi-principal elements alloys (MPEAs), multi-component alloys (MCAs) and complex concentrated alloys (CCAs) [6]. However, these terms are somewhat beyond the restrictions for entropy-based alloy design. Therefore, for the historic reasons, HEAs is the prevalent term used by now, not necessarily restricted to its original definitions.

The multicomponent alloy $Fe_{20}Cr_{20}Mn_{20}Ni_{20}Co_{20}$, which shows a single solid solution with a face centered cubic (FCC) structure was introduced by B. Cantor and co-workers in 2004 [7]. This is the first introduced and the most well-known and widely investigated composition, which is usually used with the name of Cantor alloy. The recent researches about the family of Cantor alloy will be presented in **Chapter 2**.

However, it was found that this kind of single FCC phase HEAs normally exhibits excellent ductility but lack of practical strength [8–10]. One of the approaches to improve the strength directly is alloying with interstitial elements. The invasion of the interstitial atoms deforms the alloy's lattice, leading to local stress fields that impedes dislocation motion to strengthen the alloy [11]. The elements commonly used as interstitials include carbon, boron, oxygen, nitrogen and hydrogen. Carbon is the one of the widely used interstitial element in ferrous alloys, starting from very early times, from Iron Age. Nowadays, small amounts of carbon are also used to alloy HEAs, especially in single FCC structured HEAs to improve the strength while increasing or at least not decreasing the ductility [12–14].

Severe plastic deformation (SPD) is now widely used for processing bulk ultrafine-grained (UFG) alloys. The general principle of SPD method has been proposed since the 30s of last century [15], but the procedure has become of general scientific interest only within the last 30 years. The methods receiving the most attention are equal-channel angular pressing (ECAP) [16], accumulative roll-bonding (ARB) [17] and high-pressure torsion (HPT) [18]. The detailed mechanism of HPT and synthesis procedure of the studied materials will be introduced in **Chapter 3** of this thesis.

Due to increasing the volume fraction of grain boundaries and triple junctions introduced by SPD methods, the physical and mechanical properties of UFG alloys can be outstandingly altered according to Hall-Petch relationship [19,20], according to the following formula,

$$\sigma = \sigma_0 + kd^{-1/2} \tag{1.3}$$

where σ_0 is the friction stress needed to move individual dislocations in defect-free lattice, k is a material constant and d is the average grain size. For instance, some of available data collected from several metallic alloys systems are summarized in a Hall-Petch plot shown in Figure 1.2 [21]. It was found that the grain size exponent for relatively large grains appears to be very close to -1/2 and this tendency usually lasts to ultrafine grain regime. The reported data show three different regions: (1) a region from single crystal to a grain size of about 1 mm where the classical Hall-Petch description can be used; (2) a region for grain sizes ranging from about 1 mm to about 30 nm where the Hall-Petch relation roughly holds, but deviates from the classical -0.5 exponent to a value near zero (to ascertain such behavior, a wide range of grain sizes extending into the ultra-fine grain size regime is required); and (3) a region beyond a very small critical grain size where the Hall-Petch slope is essentially zero, with no increase in strength on decreasing grain size or where the strength actually decreases with decreasing grain size, also known as inverse Hall-Petch relationship. This relationship between nano-grained microstructure of HEAs and mechanical properties will be discussed in **Chapter 4** and **Chapter 6**.

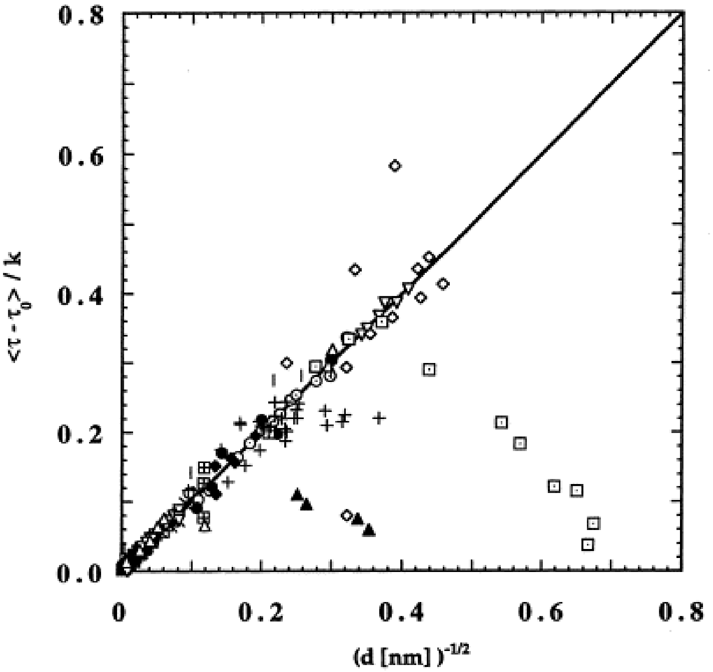

Figure 1.2 Compilation of yield stress data for several metallic systems [21].

Owing to the high-volume fraction of grain boundaries, the nano-structured alloys normally have a relatively high strength but poor ductility. Based on this consideration, post deformation annealing processing is required to obtain strength-ductility balanced mechanical properties. Therefore, further investigation on the thermal stability of SPD HEAs is necessary, which can reveal the microstructure evolution of the UFG HEAs. In this case, it will be helpful to find a balance of strength and ductility. This will be discussed in **Chapter 5** and **6**.

The aim of this dissertation is to understand the structure-property relationship of nanocrystalline single FCC structure HEAs with additional C interstitial alloying produced by SPD method. To achieve this goal, the research was focused on comprehensive microstructure characterization and mechanical tests. Firstly, we studied the microstructure evolution based on SPD process and interstitial addition into Cantor type HEA. Subsequently, the tensile test and microhardness measurements were conducted and the results were discussed combining with the microstructures. To obtain a balanced performance of mechanical properties, post deformation annealing process was carried out on the alloy deformed after HPT. Meanwhile, the thermal stability of nanocrystalline HEAs is investigated during the annealing process. Finally, the mechanical properties corresponding to the samples annealed at different temperatures were explored. Ultimately, the real engineering applications of HEAs can be accelerated based on the present research.

2 Fundamentals

HEAs as a new family of alloys were first referred to by Yeh et al. in 2004 and equiatomic CoCrFeMnNi single solid solution HEA was introduced by Cantor et al. at the same time [2,7]. However, Prof. Yeh and Prof. Cantor have already spent decades of years on the research of HEAs and multi-principal elements alloys before these publications. Without their excellent persistence and endurance, the HEAs would not receive the current world-wide attention.

2.1 High entropy alloys characteristics

The quinary CoCrFeMnNi alloy was the first one of the single-phase FCC solid solution alloys and the most widely investigated one. Therefore it also exhibits the four core effects of HEAs, which are high-entropy, severe lattice distortion, sluggish diffusion and cocktail [4].

The high entropy effect is said to be the signature concept of HEAs as it can enhance the formation of solid solutions and makes the microstructure much simpler than expected. According to the Gibbs free energy equation, increasing entropy of the mix will decrease the total free energy:

$$\Delta G_{mix} = \Delta H_{mix} - T\Delta S_{mix} \tag{2.1}$$

where ΔH_{mix} and ΔS_{mix} are enthalpy and entropy of mixing, respectively, therefore a higher number of elements would potentially lower the mixing free energy. However, it should be pointed out that adding a new element may lead to a formation of intermetallic phases more stable than solid solution [22]. According to a rough calculation from Miracle et al, ΔS_{mix} of HEAs may be sufficient to destabilize 5%-10% of intermetallic compounds at room temperature (RT) [23]. They also believed that the effect will also provide a new approach to control the microstructure and properties by formation of the precipitation-strengthened HEAs, such as an eutectic dual-phase AlCoCrFeNi HEA with homogenous distribution of BCC and FCC lamellar phases [24] and FeNiAlTi medium-entropy alloy with nanoprecipitates [25].

If it is considered as an ideal solution, the effect of enthalpy of mixing can be neglected comparing to the ΔS_{mix}. In such case, the change in Gibbs free energy leads to a change in the configurational entropy [26]:

$$\Delta G_{mix} = -T\Delta S_{mix} = \mathrm{R}T\sum x_i \ln x_i \tag{2.2}$$

where R is the ideal gas constant (8.314J $\text{mol}^{-1}\text{K}^{-1}$) and x_i is the concentration of component i in the mixture. This equation is valid in the case of any given multi-component alloy, the constituents would have to be such that they do not introduce significant enthalpy and non-configurational entropy contributions. For equiatomic component alloys, the configurational entropy of mixing reaches its maximum and can be written as follows:

$$\Delta S_{mix} = R\ln n \tag{2.3}$$

where n is the number of elements. For the quinary CoCrFeMnNi alloy the ΔS_{mix} is 1.61R. Since these elements in the multicomponent solid solutions have a different atomic radius, it was suggested that their incorporation into a single crystal structure would result in a larger number of atoms being statically displaced from their ideal positions (local lattice strain), than would be found in a compositionally simpler solid solution phase, thus leading to the severe lattice distortion effect [27]. For an example in Figure 2.1, the ideal single element alloy shows a monatomic distribution at the left and a HEA at the right side [27,28]. Consequently, it can be expected that the high distortion is one of the core principles of HEA. Even though HEAs contain a strong internal distortion, the structure of HEAs remains a long-range average crystalline structure which show well-defined Bragg reflation. Therefore, lattice distortion can cause an increase in X-ray diffuse scattering effect [29]. The evidence of lattice distortion obtained by this kind of analytic methods was later disputed because of the confounding effects from thermal vibration and crystallographic texture on the diffraction peak intensity [30]. Owen et al. systematically investigated the lattice distortion using neutron diffraction in Ni, $NiCr_{(20/25/33)}$, $Co_{37.5}Cr_{25}Ni$ and CoCrFeMnNi [31]. They found that the lattice strain in CoCrFeMnNi is larger than in pure Ni, nonetheless, the magnitude of the lattice strain is not significant and similar to that in NiCr and $Co_{37.5}Cr_{25}Ni$. Tong et al. presented a similar result regarding the lattice distortion in CoCrFeMnNi and CoCrFeNiPd HEAs by X-ray total scattering and extended X-ray absorption fine structure[32]. They indicated that the lattice distortion is rather low in CoCrFeMnNi but large in CoCrFeNiPd alloy due to the large radius of Pd atom. The study of lattice distortion is still in process by researchers to fully understand this fundamental question of HEAs.

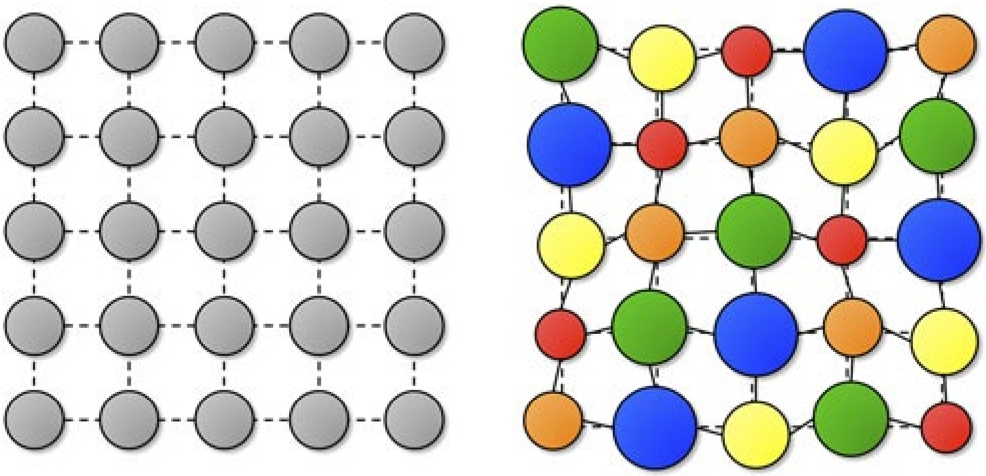

Figure 2.1 Schematic illustration of an ideal monatomic material (on the left) and of HEA (on the right). Colored spheres with different atomic radii indicate individual atomic species [27].

It was proposed that a sluggish diffusion effect is due to atomic level variation of the individual jump barriers induced by the mixture of different elements leading to a decrease of the diffusion rates Presumably this effect stabilizes the HEAs from phase decomposition or coarsening of nano-precipitates [33]. Normally, two types of diffusion are distinguished: interdiffusion and self-diffusion. Therefore, self-diffusion was usually investigated by means of tracer-diffusion techniques to verify the sluggish diffusion effect. The slow diffusion coefficients lead to exceptional temperature strength, impressive high-temperature structural stability, and formation of nanostructures [34–36]. Tsai et al. initially analyzed the diffusion behavior in the CoCrFeMnNi solution system and they found that the sequence in the order of decreasing diffusion rate was Mn, Cr, Fe, Co, and Ni [34]. The sluggish diffusion effect was determined in experiments on interdiffusion using pseudo-binary diffusion and extrapolated tracer diffusion coefficients based on ideal solution behavior of CoCrFeMnNi alloy. Later, it was challenged by Paul regarding the calculation and analysis [37]. The tracer diffusion coefficients in CoCrFeMnNi system alloys were investigated by some researchers [38–41]. They suggested that the diffusion is not anomalously slow with respect to absolute temperatures, however, it may be such when examined with the respect to homologous temperatures. Some results confirmed the sluggish diffusion effect in HEAs [42] while some others believe that sluggish diffusion effect cannot be generalized for all of HEAs [43–45]. The sluggish diffusion as one of core effects in HEAs have attracted enormous attention. However, more careful diffusion measurements are still needed to discover the exciting results. By now the term “sluggish” has to be considered with a historical respect [46].

The cocktail effect is also a matter for discussions. It was initially proposed by Ranganathan that mixing of at least five major elements should lead to a synergic effect far beyond a simple sum of properties of constitutive metals [47]. However, the multi-metallic cocktail effect, which provides new opportunities for designing metallic alloys with a balanced combination of high strength and high ductility, has not been widely approved so far [48].

2.2 Mechanical properties of FCC HEAs

Like other polycrystalline metals and alloys, HEAs derive their basic strengths from the intrinsic lattice resistance to dislocation motion and additional strengths from various incremental strengthening mechanisms. The yield strength (YS) of an alloy can be calculated as follows,

$$\sigma_y = \sigma_{ss} + \sigma_{fr} + \sigma_\rho + \sigma_{gb} + \sigma_{ppt} + \sigma_{tb} + \sigma_{pht} \tag{2.4}$$

where, σ_{ss} is solid solution strengthening including substitutional and interstitial solid solution strengthening , σ_{fr} is the friction strengthening, σ_ρ is the dislocation strengthening deduced from pre-existing dislocations, σ_{gb} is grain boundary strengthening, σ_{ppt} is the precipitation strengthening, σ_{tb} is the twin boundary strengthening , σ_{pht} is the phase-transformation induced strengthening and σ_y is the yield strength summation of above all [11]. Generally, the strengthening calculation may not include all of the mechanisms but depending on the alloy design and strategy adopted and processing applied. For instance, the strength of the, Fe–Ni–Al–Ti medium-entropy alloy is a combined effect of σ_{fr}, σ_{ss}, σ_{gb}, σ_{ppt} and σ_{pht} [25]. Each mechanism of the strengthening will be introduced in detail.

2.2.1 Solid solution effect

The CoCrFeMnNi alloy was one of the first equiatomic HEAs reported to crystallize as a single phase FCC solid solution [7]. Normally, pure FCC metals don't show temperature dependence of yield strength from 77 K to 500 K [49]. However, in the FCC CoCrFeMnNi, Cantor alloy and other FCC HEAs and MEAs exhibit relatively strong temperature dependence of yield strength with almost a factor of four increase as the temperature is decreased from 700 to 77 K [50,51]. While this behavior is different from that of pure FCC metals, it is by no means unique if we consider the broad swath of FCC alloys, for instance, the Cu-Zn and Cu-Al binary FCC solid solutions system. Figure 2.2 shows the temperature dependence of yield strength of FCC HEAs and MEAs. It shows obviously temperature dependence of yield strength. Additionally, one more point can be found in Figure 2.2 is that solid solution strengthening differences are driven by atomic size misfit. Normally, it is often predicted that high-entropy alloys should be stronger than conventional alloys or alloys with fewer elements because of enhanced solid solution strengthening from the large number of constituent elements. However, it is hard to explain with Figure 2.2 where CrCoNi ternary MEA indicated the highest yield strength. In addition, the alloys being compared should all have the same phase composition and their relevant microstructural features should be similar. Upon this point, the first study that met these criteria showed that increasing the number of elements from four in CrFeCoNi to five in CoCrFeMnNi did not change the yield strength significantly [52]. Subsequently, a more detailed study were produced on all the singe-phase FCC subsets of the Cantor alloy [51]. The alloys were thermomechanically processed to have roughly the same grain size. Clearly, strength does not increase monotonically with the number of alloying elements or entropy. Alloys with the same number of elements had significantly different strengths: FeNiCoCr is much stronger than FeNiCoMn, CrCoNi is much stronger than MnFeNi and FeNi is much stronger than NiCo. In other words, strength is not determined by the sheer number of alloying elements, rather the type of element matters.

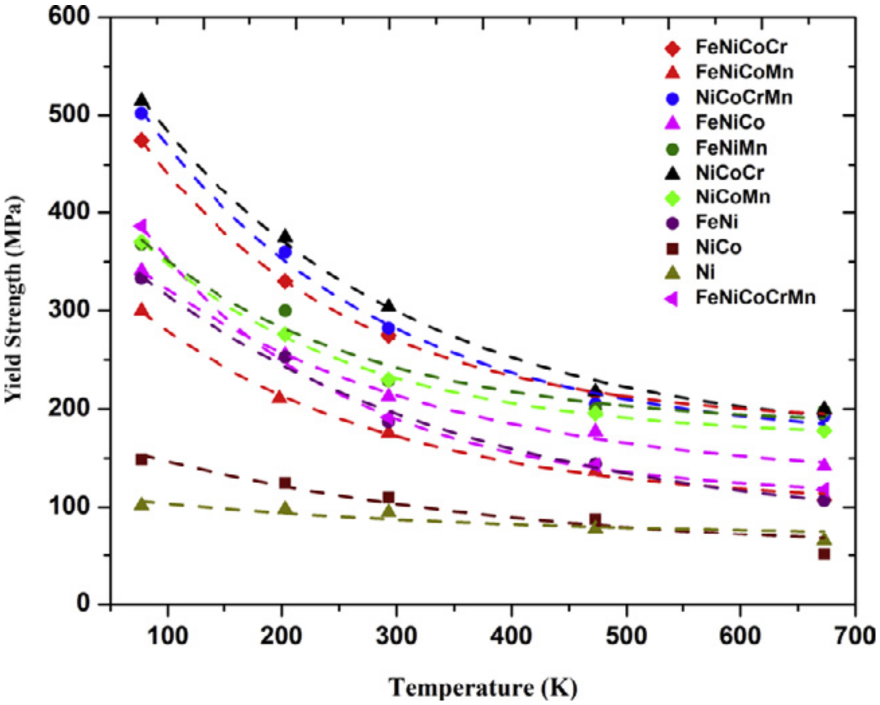

Figure 2.2 The temperature dependence of the 0.2 % offset yield stress of the equiatomic alloys and pure Ni [51].

In order to explore the most effective elements in the complex concentrated solid solutions, some researchers tried to find out the volume misfit which can be determined by atomic displacement parameter (ADP) [53]. It is the sum of squares of the constituent atoms displacement from the mean positions due to vibrations and the static displacements of the mean positions form the ideal lattice points. For CoCrFeMnNi alloy, the values for the ADP at 25 and 300 K were found to be approximately 24 and 59 pm^2, respectively, while it is 24 pm^2 at 25 K calculated by first principles calculations [53]. The results from the above publication revealed that Cr with the largest effective radius has the biggest effect on solid solution strengthening.

Interstitial solid solutions form by squeezing small solute atoms into interstitial sites between the solvent atoms. Carbon is one of the most commonly used elements for interstitial strengthening. Interstitial solutes normally cause a tetragonal distortion to the lattice, producing a shear field that strongly interacts with the edge, screw, and mixed dislocations [11].

Fleischer proposed the yield strength increase by interstitial strengthening as follows [54,55]:

$$\sigma_{iss} = \frac{MG\Delta\varepsilon c^{1/2}}{3} \tag{2.5}$$

where M= 3.06 is the Taylor factor, G is the shear modulus, c is the concentration of the soluted interstitials and $\Delta\varepsilon$ is the difference between the longitudinal and transverse strains of the tetragonal distortion source.

Li et al. alloyed 0.5 at % carbon into FeMnCoCr MEA which leaded to a significant increasing of yield and ultimate strength but a slightly lower elongation in comparison with not-alloyed state [56]. Additionally, the tensile strength of the grain-refined interstitially-alloyed HEA is nearly twice that of the corresponding single-phase equiatomic CoCrFeMnNi alloy, while their elongation values under tensile load are identical. Figure 2.3 shows the exceptional strength-ductility combination found for interstitially alloyed HEAs. Furthermore, the alloys exhibit a substantial damage tolerance, characterized here in terms of total elongation multiplied by ultimate tensile strength, exceeding that of most metallic materials. Stepanov et al. prepared a set of CoCrFeMnNi containing 0, 2.0, 3.4 and 4.8 at. % of carbon [57]. Carbides were formed in alloys with higher carbon concentration and less than 1.38 at. % of carbon can be dissolved in CoCrFeMnNi alloy according to thermodynamic predictions. Nevertheless, the microhardness increases with the increasing of carbon content in the alloys from 160 HV of the CoCrFeMnNi alloy to 275 HV of the $CoCrFeMnNiC_{0.25}$ alloy. Similarly, Chen et al. and Wu et al. also investigated the carbon-containing CoCrFeMnNi alloys and have the approximate conclusions that both yield strength and ultimate tensile strength were increased by minor C addition while high uniform elongations to fracture are still maintained [13,14]. However, an overdose of carbon can still maintain the interstitial strengthening effect but will deteriorate ductility significantly, partly because of the precipitation of carbides such as M_7C_3 and $M_{23}C_6$ at grain boundaries or in grain interiors [13,45,57].

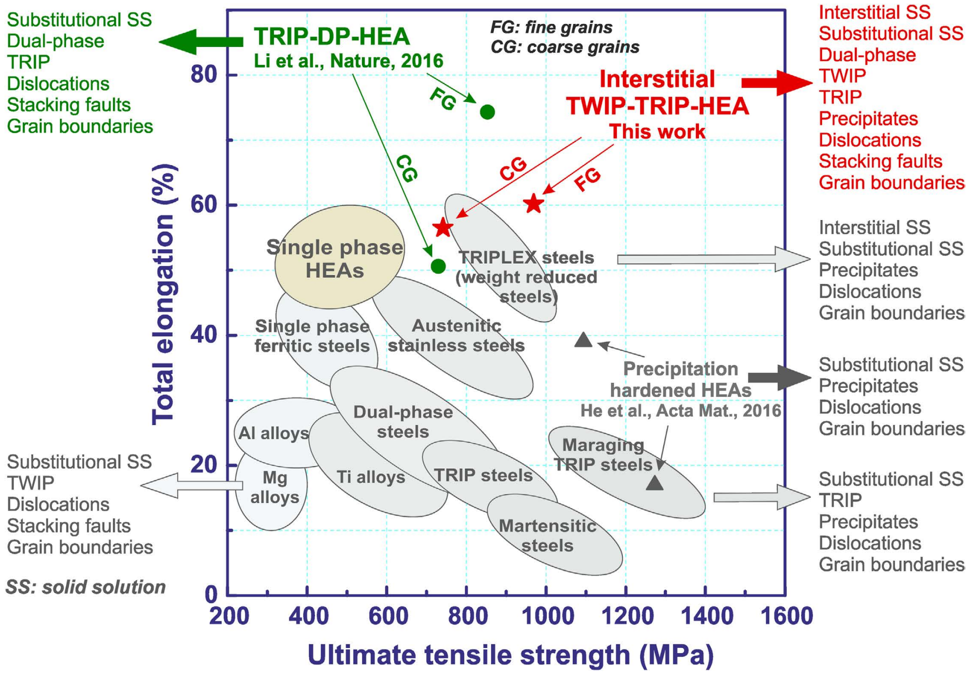

Figure 2.3 Strength-ductility profiles of various classes of metallic materials including HEAs [56].

2.2.2 Grain size effect (Hall-Petch in HEAs)

As HEAs are normally polycrystalline solids, the grain boundary strengthening often needs to be taken into considerations which does not remain constant but depends on the average grain size. The increase of the yield strength with the decreasing grain size, σ_{gb}, can be described by the Hall-Petch strengthening [19,20],

$$\sigma_{gb} = kd^{-1/2} \tag{2.6}$$

where k is the Hall-Petch strengthening coefficient and d is mean grain size. The k value can be rigorously estimated by linear fitting procedure using the full Hall-Petch relation which has been mentioned in Chapter 1, equation (1.3).

The Hall-Petch relationship of CoCrFeMnNi was initially reported by Liu et al. using Vickers hardness measurements [58]. Subsequently the tensile measurements were performed to investigate the Hall-Petch relationship from 77 to 873 K [9]with the grain sizes of 4.4, 50, and 155 μm. The k coefficients were found to vary from ~530 to ~420 MPa μm $^{-1/2}$ which shows a decreasing with temperature increasing and it is 494 MPa μm $^{-1/2}$ at RT. Afterwards, a series of samples of fully recrystallized CoCrFeMnNi alloy with grain sizes in a range from 0.5 to 88.9 μm were produced to measure the Hall-Petch slope at RT [59]. Figure 2.4 (a) shows the tensile engineering stress-strain curves of the CoCrFeMnNi HEA specimens with different grain sizes and Figure 2.4 (b) reveals the typical Hall-Petch relationship fitted between the yield strength and the inverse square root of grain size. The k slope of this result is close to the one above, which is 490 MPa μm $^{-1/2}$. In the ternary CoCrNi alloy, the value of the slope is 265 MPa μm$^{-1/2}$ measured with fully recrystallized FCC single phase with various grain size from 0.2-111 μm [60].

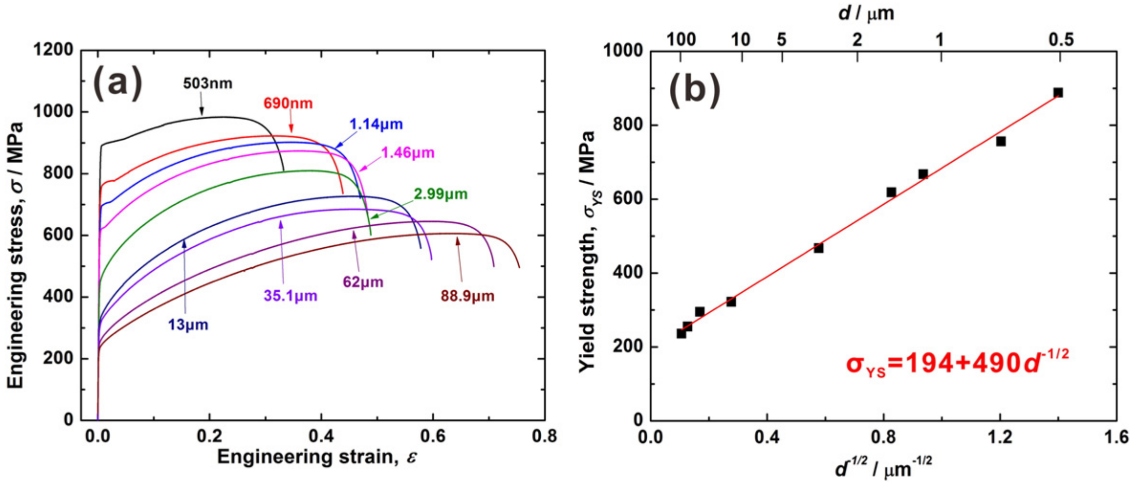

Figure 2.4 (a) Tensile engineering stress-strain curves of the fully recrystallized CoCrFeMnNi HEA with different grain sizes. (b) Plots of yield strength against inverse square root of grain sizes for the CoCrFeMnNi[59].

In general, we can find that HEAs have both higher σ_0 and k values than their pure metal counterparts [61]. The higher σ_0 value in HEAs is originated from their enhanced solid solution strengthening compared to pure metals, attained by the severe size and modulus mismatch of different atomic species [60,62,63].The higher k slope in the HEAs is an implication of harder slip transfer between grains and more significant grain boundary strengthening, which is caused by the fact that curvy due to the severe lattice distortion dislocation lines in HEAs slip harder than the straight ones in pure metals [58]. Some researchers suggested that k slope was initially affected by stacking fault energy (SFE) and shear modulus, analogous to the correlation in other alloy systems [51,64,65]. Meanwhile, the alloys with a large shear modulus usually require larger shear stress to glide dislocations through the lattice and lager dislocations pile ups at grain boundaries leading to a high k slope [65].

2.2.3 Dislocation effect

Expect the ideal perfect crystal, all metallic materials contain the pre-existing dislocations to varying extent. Dislocations from specific slip planes interact with each other while the stress is applied. This dislocation interaction mechanism essentially constitutes the core of dislocation strengthening. The higher the number of dislocations in a material, the higher the strength increase from the dislocation strengthening. Based on this theory, the strengthening from dislocation can be described by Taylor model,

$$\sigma_\rho = M\alpha_T G b \rho^{1/2} \tag{2.7}$$

where M=3.06 is the Taylor factor, G is the shear modulus, α_T is a constant approximated to 0.2 for FCC alloys, b is the magnitude of the Burgers vector and ρ is the dislocation density. Once we have known the Young's modulus E, and Poisson's ratio ν, G can be calculated from $G = E/2(1+\nu)$. The value of b is calculated knowing the lattice structure. In order to determine the dislocation density, ρ , following equation may be used [66–68],

$$\rho = \frac{2\sqrt{3}\varepsilon}{db} \tag{2.8}$$

where d is the mean crystallite size and ε is the micro-strain (lattice strain) in the materials. Or with the equation proposed by Williamson and Smallman [69],

$$\rho = 16.1^{\frac{\varepsilon^2}{b^2}} \tag{2.9}$$

Both microstrain and crystallite size can be determined from the analysis of the line broadening of the X-ray diffraction (XRD) peaks, for example, using Williamson-Hall method [69,70].There are also some other methods to retrieve the density of dislocations, such as from Transmission Electron Microscopy (TEM) images using Ham's method [71].

However, the dislocation density in fully recrystallized and slow cooled alloys is very low which can be neglected sometimes comparing with cold worked alloys. Woo et.al compared the dislocation density between CrCoNiFe and CrCoNi MEAs deformed at 293 and 140 K with in-situ neutron diffraction [72]. In CrCoNiFe alloy, the dislocation density of as-received alloy increased from ~6.3× 10^{14} m^{-2} up to 3.4

$\times 10^{15}$ m^{-2} with a strain of 0.6 at RT while the dislocation density had significantly increased from 1.9 to 9.7 $\times 10^{15}$ m^{-2} in the CrCoNi at 293 K, as shown in Figure 2.5. Thirathipviwat et al. performed the high energy synchrotron XRD studies on pure Ni, FeNiCo and CoCrFeMnNi after cold swaging processing and post deformation annealing [73]. The results shows that dislocation density in CoCrFeMnNi, FeNiCo and Ni after cold-swaging process is 12 $\times 10^{14}$ m^{-2}, 6.7 $\times 10^{14}$ m^{-2} and 2.8$\times 10^{14}$ m^{-2}, respectively and the level of dislocation accumulation it related to the number of constituent elements and the intrinsic properties. Fu et al. calculated the dislocation strengthening in nanocrystalline $Co_{25}Ni_{25}Fe_{25}Al_{7.5}Cu_{17.5}$ alloy fabricated using mechanical alloying followed by spark plasma sintering [74]. Consequently, the calculated dislocation strengthening is ~600 MPa, 33 % of yield strength.

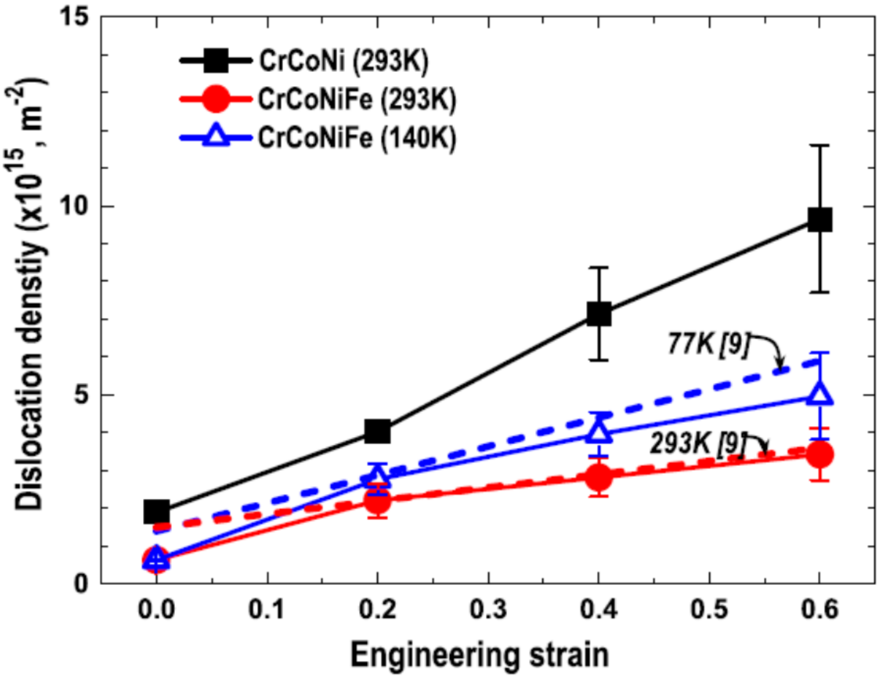

Figure 2.5 Microstructure related parameters dislocation density as a function of engineering strain in MEAs at indicated temperatures [72].

2.2.4 Precipitation effect

Precipitation strengthening was first discovered in aluminum alloys by Alfred Wilm, a German metallurgist in 1901. Nowadays, people developed a series of methods to improve the balanced mechanical properties of alloys, including HEAs, by utilizing precipitates by composition design and heat treatment process. Due to complex chemical composition and limitation of solute-element solid solubility, various precipitates including coherent precipitates formed from oversaturated matrix, which can also cause the strength increase without simultaneous decrease of plasticity. The strengthening effect of precipitates essentially stems from their blockages to dislocation motion. The way that precipitates interact with and thus retard moving dislocations determines how a material is strengthened. Depending on the size and the lattice coherency with the matrix material, precipitates may impede dislocation motions in two broadly distinct ways. One is particle shearing mechanism (type I) and the other is Orowan by-pass mechanism (type II), which mainly depends on the size and strength of the precipitates [75]. In shearing progress, the size of precipitates is normally small and it is affected by the coherency strain, SFE, ordered structure, modulus effect, interfacial energy and morphology, and lattice friction stress [11]. Since the precipitates grow up, the dislocation moves to bend around the particle until it is enclosed completely and the dislocation can move on, leaving a dislocation loop around the by-passed particle.

At present, the small-sized nanoprecipitates in HEAs mainly include the carbides ($M_{23}C_6$ and M_7C_3) [57,76,77], γ' phase with a $L1_2$ structure [78–80], γ'' phase with a $D0_{22}$ structure [81], B2 phase precipitate [82], hard σ phase [83] and μ phase [84]. Typical cuboidal AlNb $L1_2$ nano-precipitates are shown in Figure 2.6 in bright field (BF) and dark field (DF) TEM image from the [001] zone axis in (a) and (b), respectively [80]. Figure 2.6 (c) indicates the composition distribution maps of each element acquired from Atom probe tomography (APT). In Figure 2.7, a BF-TEM micrograph of a NbC particle in $CoCrFeNiNb_{0.8}C_{0.8}$ HEA and corresponding High-resolution transmission electron microscopy (HRTEM) image indicate the coherent relationship between the FCC matrix and the NbC particles [77].

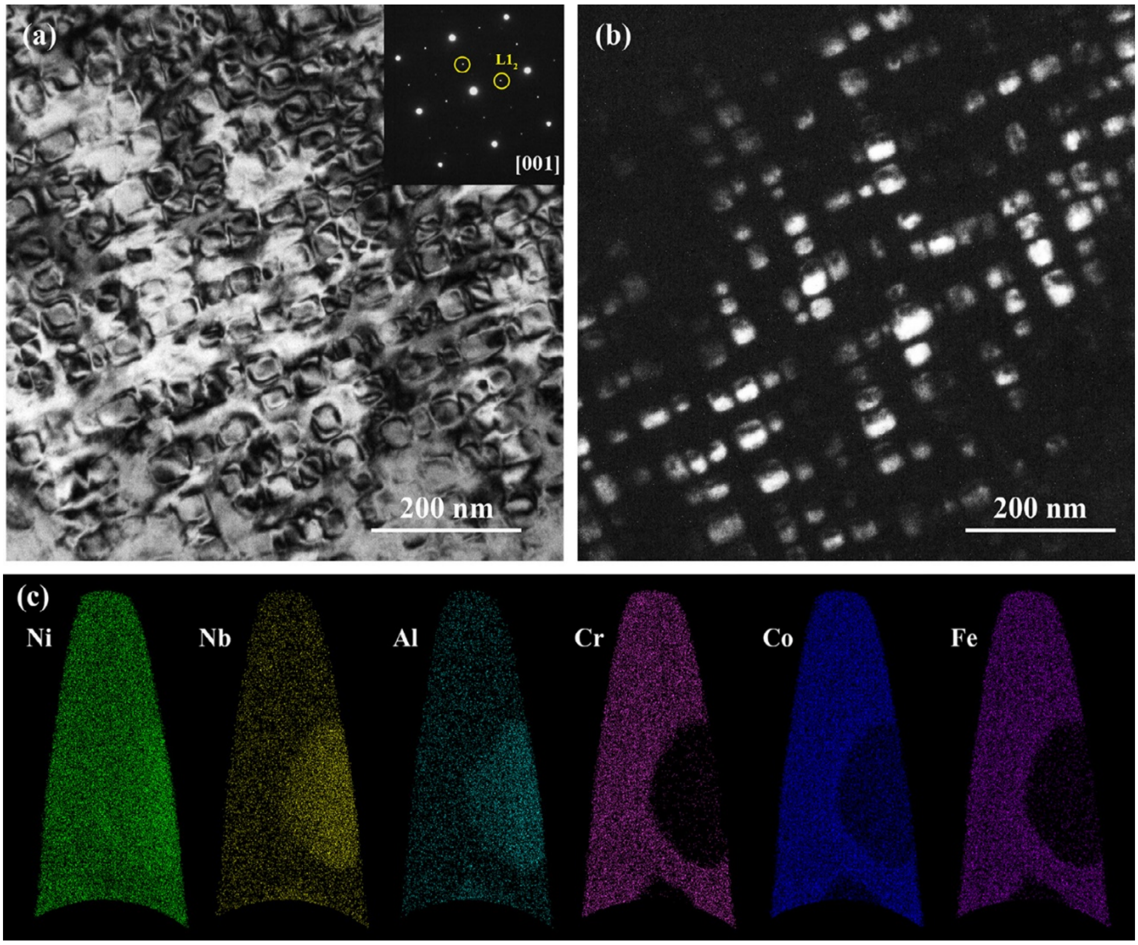

Figure 2.6 (a) Typical bright-field micrograph showing the microstructure of the $(NiCoFeCr)_{92}Al_4Nb_4$ HEA. (b) Dark-field micrograph obtained from the superlattice spot corresponding to the ordered structure. (c) Ion maps of the individual elements from APT [80].

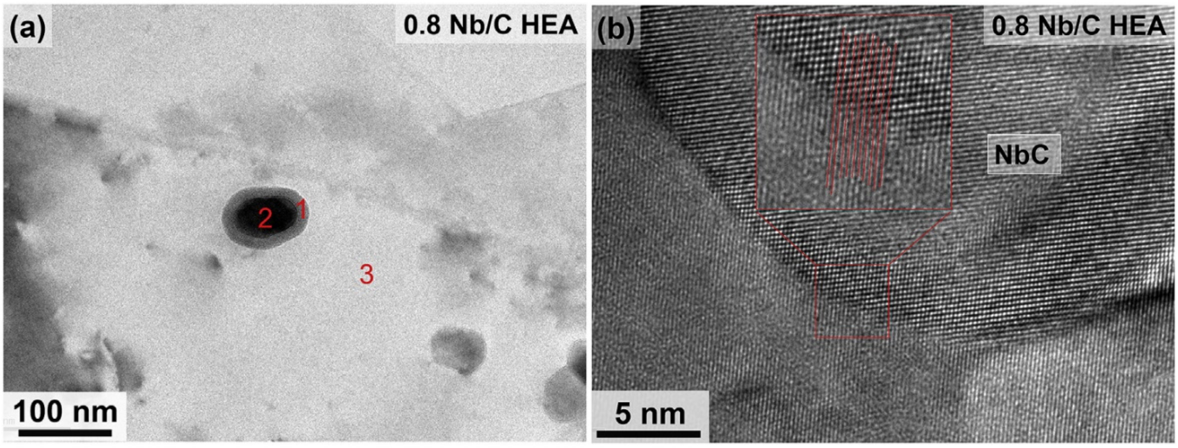

Figure 2.7 Intragranular nanoscale NbC precipitates in the CoCrFeNiNb$_{0.8}$C$_{0.8}$ HEA: (a) BF-TEM image and (b) HRTEM image showing coherency between the matrix and NbC particle [77] .

As mentioned before, there are two mechanisms of interaction between dislocations and second phase particles, the overall strengthening can be combined as follow [68],

$$\sigma_{ppt} = f_{\mathrm{I}}\Delta\sigma_p^{\mathrm{I}} + f_{\mathrm{II}}\Delta\sigma_p^{\mathrm{II}} \tag{2.10}$$

where $\Delta\sigma^{\mathrm{I}}$ and $\Delta\sigma^{\mathrm{II}}$ are the precipitation strengthening resulting from the type I and II particle and f_{I} and f_{II} are the volume fractions of the regions containing the type I and II particles. Three contributing factors are considered and they are particle-matrix coherency (σ_{CS}), modulus mismatch (σ_{MS}) and atomic ordering (σ_{OS}) [85–87]. The former two make contributions prior to the shearing, while the latter one contributes in the process of cutting through particles. The equations for the type I contributions are as follows,

$$\sigma_{CS} = M\alpha_{\varepsilon}(G\varepsilon_a)^{\frac{3}{2}}\left(\frac{rf_P}{0.5Gb}\right)^{1/2} \tag{2.11}$$

and

$$\sigma_{MS} = 0.0055M\Delta G^{\frac{3}{2}}\left(\frac{2f_P}{G}\right)^{1/2}\left(\frac{r}{b}\right)^{\frac{3m}{2}-1} \tag{2.12}$$

where α_{ε} =2.6 for FCC structure, ε_{a} is the constrained lattice parameter misfit with the lattice parameter difference between the precipitates and the matrix; r is the average particle radius; f_{P} is the volume fraction of the precipitates; ΔG is the shear modulus mismatch between the precipitates and the matrix; m is a constant taken to be 0.85.

The strength increment is primarily dictated by atomic ordering for type II particles, given by

$$\sigma_{OS} = M0.81\frac{\gamma_{APB}}{2b}\left(\frac{3\pi f_P}{8}\right)^{1/2} \tag{2.13}$$

where γ_{APB} is the anti-phase boundary energy of the precipitates.

He et al. designed $(FeCoNiCr)_{94}Ti_2Al_4$ precipitation-hardened HEA with coherently $L1_2$ structured $Ni_3(Ti, Al)$ precipitates in the FCC matrix [68]. With proper thermomechanical processing, the particle size are 12.6 nm and 46.3 nm while the contributions are 305.6 MPa and 371.9 MPa, respectively.

2.2.5 Deformation twinning effect

It is known that high density of twin boundaries in FCC alloys imparts a high tensile strength while keeping a considerable ductility which is attributable to the blockage of twin boundaries to dislocation motion [88]. More specifically, twins generated during deformation gradually introduce new interfaces to reduce the dislocation mean free path and thus contribute to strengthening [89–91]. That mechanism is deformation-induced twinning, which starts to appear sporadically in some grains after reaching the critical stress for twinning normally in FCC alloys such as CoCrFeMnNi HEA [9]. With increasing strain, the thickness and volume fraction of twins increase. It has been suggested that mechanical twins contribute to strengthening by dividing the grains into progressively smaller grains which is called dynamic Hall–Petch effect [92,93]. This deformation induced twinning provides a source of high, sustained work hardening that postpones the onset of necking instability to higher strains [52]. As a result, the effect is able to increase both strength and ductility simultaneously. Since the strengthening effect of twins is due to the blockage of twin boundaries to dislocation motion, it is easy to imagine that the twin boundary strengthening in the first place depends on the twin spacing. Thus, the strengthening effect from twins can be described as follows [88,94,95],

$$\sigma_{tb} = f_{\mathrm{t}} k_{tb} \lambda_t^{-1/2} \tag{2.14}$$

where f_t is the volume fraction of the grains that contain twins, k_{tb} is the twin boundaries coefficient and λ_t is the average twin thickness.

Su et al. evaluated the strengthening from twin boundaries contribution in $Fe_{50}Mn_{30}Co_{10}Cr_{10}C_{0.5}$ carbon alloyed MEA after cold deformation and heat treatment, as shown in Figure 2.8 [94], which indicates that one third of yield strength is contributed by twin boundaries in 400 °C for 10 min sample.

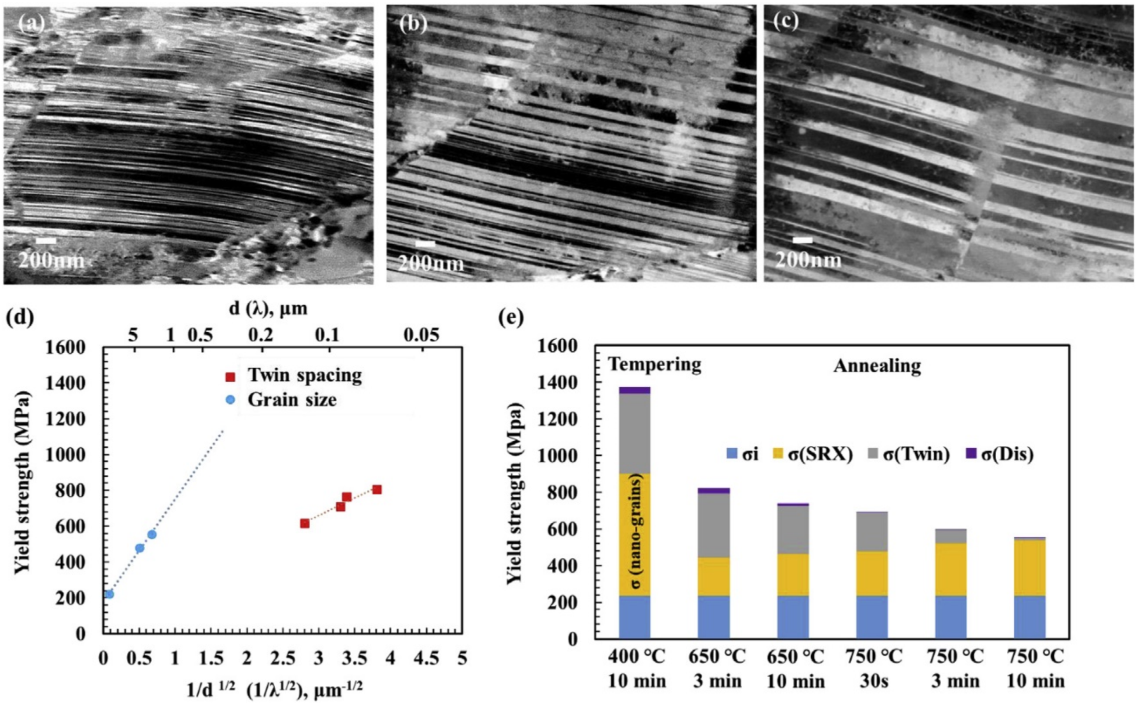

Figure 2.8 ECC images showing nano-twins in specimens annealed at (a) 650 °C for 3 min, (b) 650 °C for 10 min and (c) 750 °C for 3 min. (d) Relations of the increase of the yield strength with grain size and twin spacing of the annealed specimens and (e) increase of the yield strength due to nanograins, SRX, twins and dislocations of the specimens subjected to tempering and annealing [94].

One factor that can affect twinning ability is SFE [96]. Experimentally measured SFE of ternary equiatomic alloy CrCoNi is ~22 ± 4 mJ m $^{-2}$, while SFE of CoCrFeMnNi HEA is ~30 ± 5 mJ m $^{-2}$ at RT [53,97]. As a result of this, the CrCoNi alloy exhibits better strength and ductility. The temperature, as well, has an effect on both, critical stress for twinning and SFE [8,98]. Twinning can be expected in CoCrFeMnNi HEA at RT if higher strain is applied, such as cold rolling [99]. The axial stress at which twins appear at 77 K is ~720 MPa, however, such high flow stress cannot be achieved at RT [8]. One more factor that is known to affect twinning is grain size: deformation twinning is reduced as the grain size is decreased [100].

2.3 Severe plastic deformation on HEAs

SPD is effective in producing bulk UFG and nanostructured materials with large densities of lattice defects [101]. The SPD technology is presently the most effective procedure to produce nanomaterials and it includes different processing techniques and their modifications, HPT, ECAP, ARB, twist extrusion (TE), multi-directional forging (MDF) and so on [101–103]. Nowadays, with the development and attraction on HEAs, SPD technologies are widely applied to new type of alloys to improve their physical and mechanical properties.

2.3.1 SPD methods

Percy W. Bridgman won the Nobel Prize in physics in 1946 and he is considered as the first scientist who developed the technique allowing to apply simultaneously high pressure and large strain to metals

[104]. Based on this technique, a SPD method, which is now known as high-pressure torsion was developed [15]. During HPT process, the materials are torsionally strained under high pressure between two anvils, as shown in the schematic in Figure 2.9. The sample, in the form of a disk, is located between two anvils where it is subjected to a compressive pressure at RT or at an elevated/cryogenic temperature and simultaneously to a torsional strain which is imposed through a rotation of the lower anvil. Surface frictional forces therefore deform the disk by shear so that deformation proceeds under a quasi-hydrostatic pressure [105].

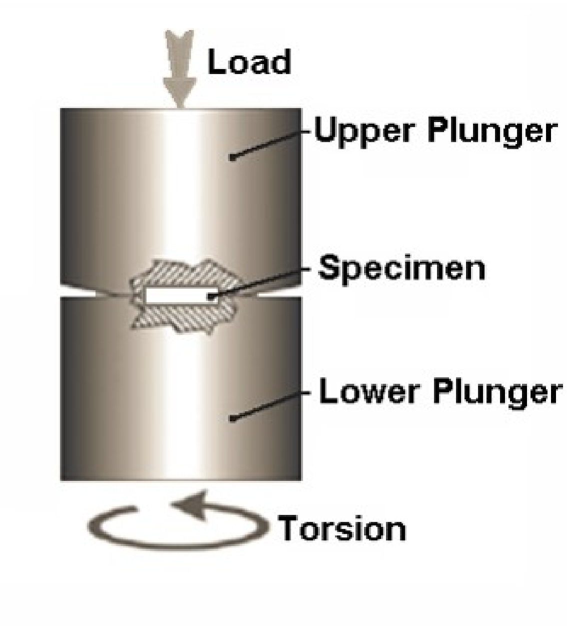

Figure 2.9 Schematic illustration of HPT processing[106].

The shear strain at HPT can be calculated as follows [105],

$$\gamma = \frac{2\pi N r}{h} \tag{2.15}$$

where N is the number of revolutions, r is the radius from disk center and h is the thickness of the disk. Then, it is also possible to convert the shear strain to equivalent von Mises strain given by

$$\varepsilon = \gamma/\sqrt{3} \tag{2.16}$$

The HPT method is undoubtedly the most efficient SPD method for fundamental studies because of two main reasons. One is that the processing parameters such as strain, strain rate, pressure and temperature can be easily controlled. On the other hand, the pressure applied during HPT is quite high enough and offers a unique opportunity to handle almost all types of materials including hard and brittle ones such as silicon or diamond [107]. Hebesberger et al. investigated the deformed microstructure in pure copper by HPT [108]. A sequence of Backscattered electrons (BSE) images of microstructures is presented with increasing shear strains from 1.7 up to 880 in Figure 2.10 (axial direction), which indicated the strain effect on the grain refinement. This is a proper example to exhibit the advantage of

HPT that can be controlled well combined with microstructure evolution. Despite HPT has such advantages for fundamental studies, the size of samples severely deformed with HPT are much smaller than those deformed with other methods.

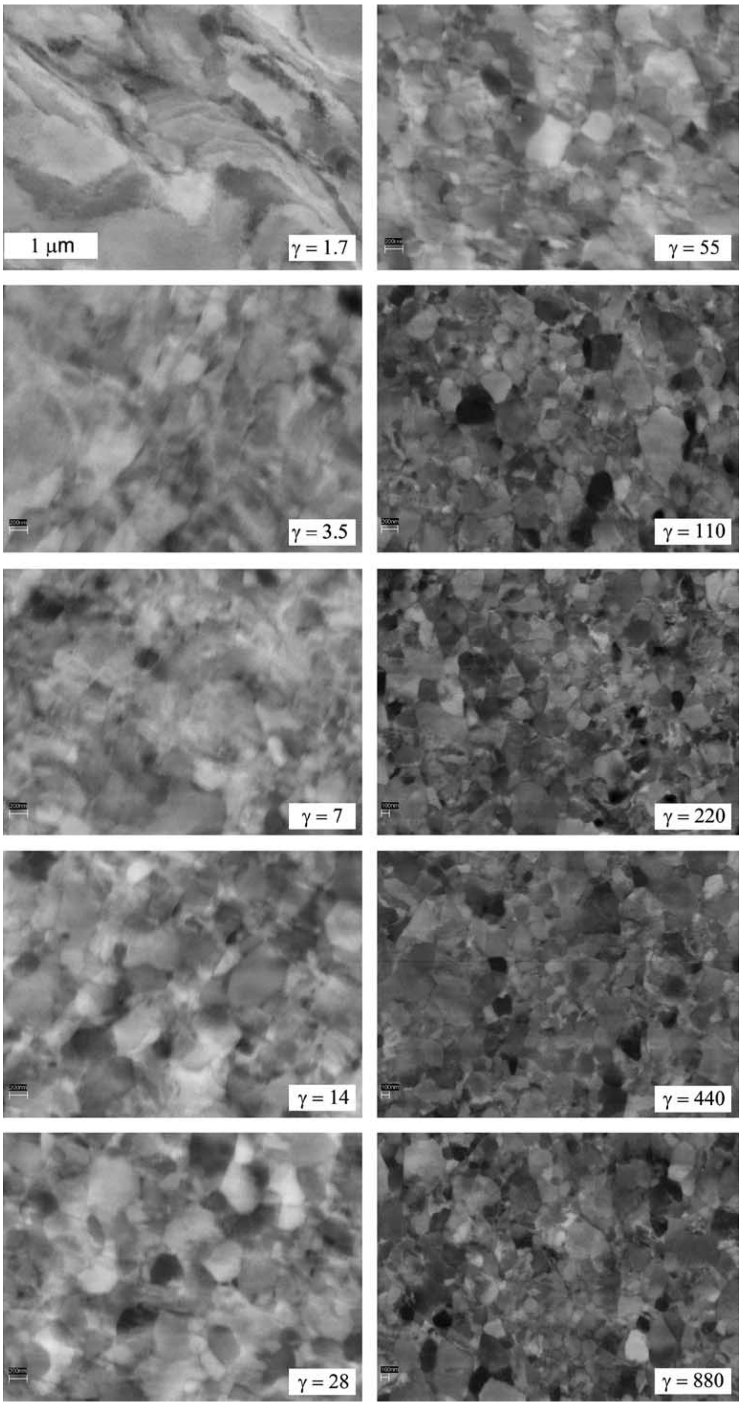

Figure 2.10 BSE micrographs in axial direction (deformed at 2 GPa, RT), magnification is the same in all micrographs [108].

The method of ECAP realizing deformation of massive billets via pure shear was developed by Segal and co-workers in the beginning of 80s last century [102]. The schematic illustration of ECAP method is shown in Figure 2.11[109]. Its goal was to introduce intense plastic strain into materials without changing the cross-section area of billets. As a result of this, multiple passes of the deformation are required for accumulating strains and obtaining the UFG structure.

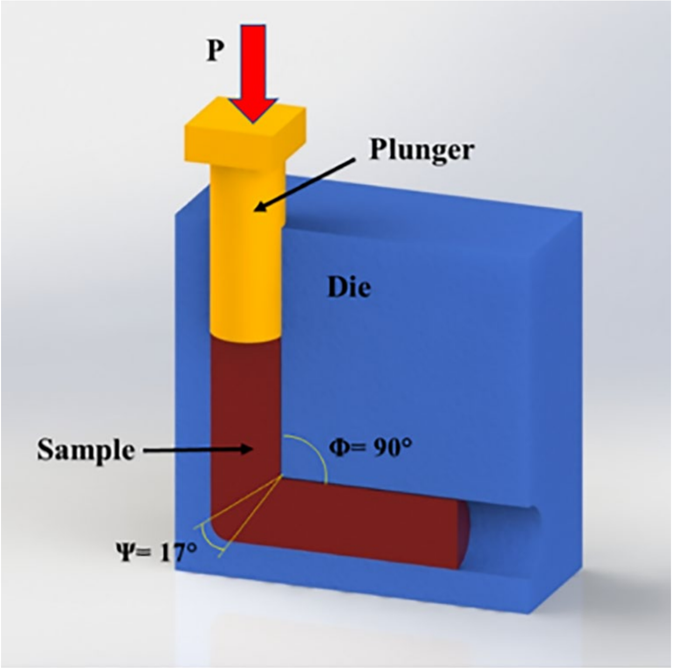

Figure 2.11 Schematic illustration of ECAP die including inner angle Φ and outer angle Ψ[109].

The shear strain value increment for each pass through the channel is given by [102,110],

$$\varepsilon_N = N \frac{2\cot\left(\frac{\phi+\psi}{2}\right)+\psi \operatorname{cosec}\left(\frac{\phi+\psi}{2}\right)}{\sqrt{3}} \tag{2.17}$$

where N is the number of passes, ϕ is the inner angle, ψ is the outer angle.

It looks like that accumulation of strain is unlimited if the number of passes is adequate. However, a deformation in ECAP process is not uniform. Because of a complex deformation mode operative in the ECAP process, there exists a gradient from the top to the bottom part of the ECAP deformed billet by simple shear in a narrow zone along the die intersection plane [111]. Therefore, the strain at one ECAP path is generally not high enough to completely overprint the microstructure existing at the beginning of each pass. After multi-pass ECAP processing leading to a certain strain, a steady state microstructure develops.

The ARB process was developed by Saito et al. in the late of 90s last century [17]. The schematic representation of ARB process is presented in Figure 2.12. First of all, a strip of a metal is neatly placed on top of another strip. The interfaces of the two strips are surface treated in advance in order to enhance bonding strength. The two layers of material are joined together by rolling, as in a conventional roll-bonding process. Then, the length of rolled material is sectioned into two halves. The sectioned strips are again surface-treated, stacked and roll-bonded. The whole process is repeated again and again. Consequently, arbitrarily large deformation is possible by the ARB process. The von Mises equivalent strain after N cycles of ARB process is given by

$$\varepsilon_N = -\frac{2N}{\sqrt{3}}\ln(1-r) \tag{2.18}$$

where r is the reduction in thickness per cycle. For example, if the process is repeated seven times, the initial thickness is reduced to 1/128. The 1.0 mm thickness reduces to 7.8 µm. The achieved total reduction is 99.2 % and the total equivalent plastic strain is 5.6. It is easy to introduce ultra-high strain into materials by the ARB process. Hence, ARB is basically applicable to all kinds of metals and alloys deformable in rolling, and UFG structures are achievable in such bulky metals and alloys.

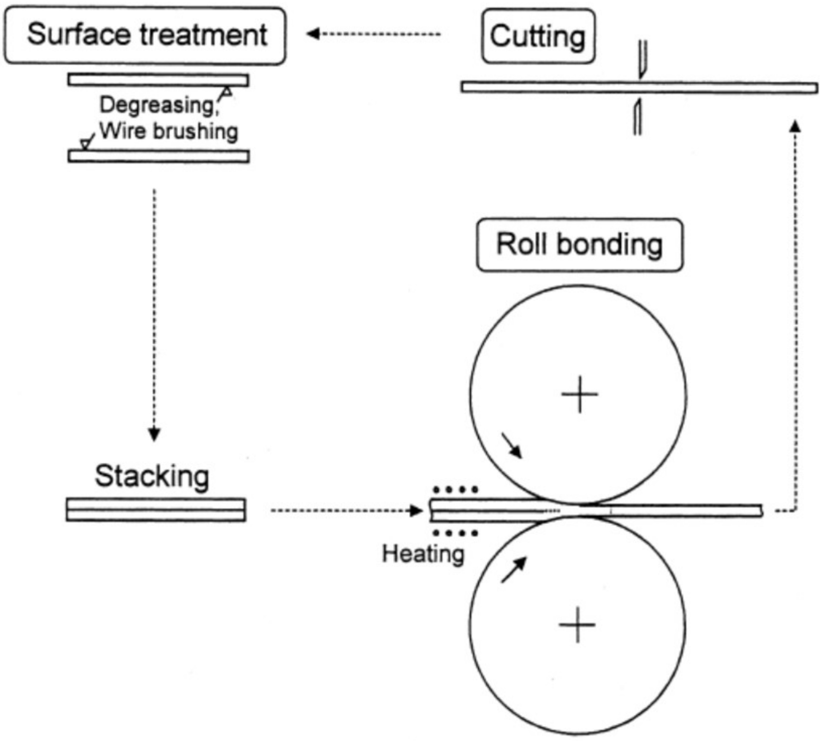

Figure 2.12 Schematic illustration of the accumulative roll-bonding (ARB) process [17].

Due to the limitation of sample size of HPT, a new scaling up the HPT process, so-called High Pressure Torsion Extrusion (HPTE) has been presented by Ivanisenko et al. [112]. Comparing to the SPD methods above, it allows to implement simple shear conditions and high hydrostatic pressure in a rod shape specimen, and to accumulate a large strain in only one single pass. The schematic illustration of HPTE is shown in Figure 2.13. The strain accumulated in a specimen after one pass can be controlled according to the equation,

$$\varepsilon = 2\ln\frac{D_1}{D_0} + 2\ln\frac{D_1}{D_2} + \frac{\varpi R}{\sqrt{3}\nu}\frac{D_1}{D_2} \tag{2.19}$$

where the D_0 and D_2 are the inlet and outlet diameter of the container channels, D_1 is the diameter of extrusion container channels, ν is the translational velocity and ω is velocity of rotational motions.

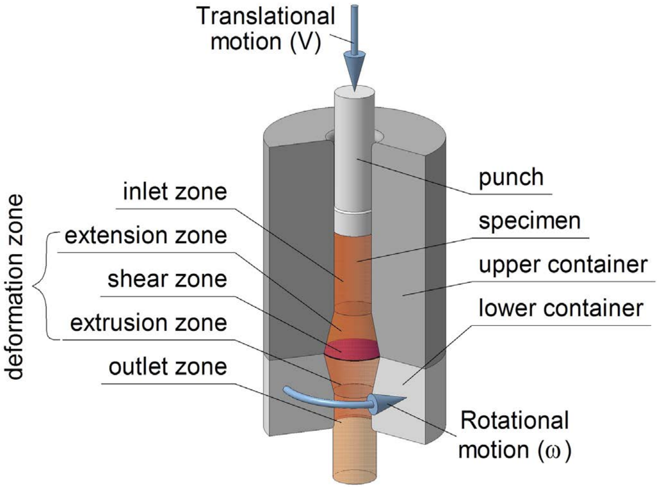
Translational motion (V)
deformation zone
inlet zone
extension zone
shear zone
extrusion zone
outlet zone
punch
specimen
upper container
lower container
Rotational motion (ω)

Figure 2.13 Schematic diagram of the HPTE process [112].

Because of the limitation of the section, I would not introduce all the SPD methods. It is expected that the gradient structured materials produced by various SPD methods in the future will be employed for an extended range of functional applications.

2.3.2 Microstructure refinement mechanism at SPD

It is known that the two major deformation mechanisms in coarse grain materials at low homological temperatures and moderate strain rates are dislocation slip and deformation twinning. Dislocations can nucleate and slip under stress to accommodate the applied plastic deformation. A single dislocation line can glide on a densely packed atomic plane called slip plane along any direction but the resulting crystallographic slip is along a particular direction called slip direction. Depending on orientation relationships between dislocation lines and their Burgers vectors, edge dislocations, screw dislocations and mixed dislocations are classified. Slip system is a combination of a slip plane and a slip direction. Slip systems depend on the crystal structure of the material in a way that the atomic distortion that accompanies the motion of a dislocation is kept to a minimum. Therefore, the slip plane is normally the most densely packed plane and the slip direction is the most closely packed direction. Table 2.1 indicates the slip systems in FCC and BCC structures [113].

Table 2.1 Common slip systems in FCC and BCC structures [113].

Crystal structure	Slip system
FCC	{111}<110> {001}<110> {110}<110>
BCC	{110}<111> {211}<111> {321}<111>

Principally, the most commonly accepted models of grain refinement due to large strain induced by SPD are based on the notion that a dislocation cell structure, which forms already in the early stages of plastic deformation, gradually transforms to the final fine grain structure [114]. Kocks and Mecking described the deformation behavior of metals and alloys in terms of a single internal variable of the total dislocation density [115]. Prinz, Argon and Nix adopted the approach proposed by Mughrabi, that the cell walls and cell interiors are treated as two distinct phases of a ‘composite’ [116–119]. Estrin et al. and Zehetbauer et al. proposed constitutive models based on Mughrabi’s composite principle and detailing the evolution of the dislocation densities in the cell walls and cell interiors, including interactions between the two “phases” of the composite [120–122], which is a useful platform for modelling SPD processes.

Upon the dislocation theory above, the grain refinement induced by SPD of FCC materials can be categorized into 5 stages according to the dominant microstructural features at each stage. At the stage I, the individual grain are subdivided fast to some volume elements delineated by dense dislocation walls [123]. These dense dislocation walls, are also called geometrically necessary boundaries (GNBs) which misorientation is controlled by the difference in dislocation slip induced by lattice rotation in neighboring volumes [124]. Each volume in the grain is determined as a cell block [125]. The active slip systems in these cell blocks are different from each other and can operate collectively to fulfil the von Mises criterion for strain accommodation [126]. Dislocations from neighboring cell blocks meet at a GNB, leading to dislocation interactions, entanglement and rearrangement [127,128]. As dislocations from neighboring cell blocks are from different slip systems, the cell blocks will rotate in different ways, leading to increasing misorientation across the GNB. Meanwhile, a large number of dislocation cells formed at the interior of each cell block [126]. A cell wall may look similar to a dense dislocation wall, but it is formed primarily by the mutual and statistical trapping of incidental glide dislocations, and thereby named as incidental dislocation boundary [129,130].The formation mechanism of these cell walls can be explained in a way that dislocations are trapped into positions of local energy minima in which stress-screening between dislocations occurs [131,132]. At the start of the stage II, numerous dislocations accumulate at cell walls and dense dislocation walls which results in higher misorientation across these cell walls.

Consequently, cell walls may transform into dense dislocation walls and some early formed dense dislocation walls may split into new dense dislocation walls parallel. As a result, large amounts of cell blocks and micro bands with reduced sizes are formed. In addition, dense dislocation walls have a tendency to align with the macroscopically most stressed planes to delineate comparatively long and regularly spaced slip bands [133,134]. At stage III, large amounts of lamellar sub-grains enclosed by lamellar boundaries form, as a result of continuous reduction of cell block sizes and significant increase of misorientation angles across dense dislocation walls. Within these lamellar sub-grains are interconnecting boundaries, dislocation clusters and individual dislocations. With the further strain increasing, the stage IV develops, when the lamellar boundaries and interconnecting boundaries gradually sharpen and become thinner, and the misorientation across the boundary increases [135,136]. Finally, the grain refinement reaches a steady state at the stage V, which usually presents equiaxed grains. However, the microstructure observed at stage V may differ in different materials and conditions of SPD methods. Figure 2.14 presents schematic diagrams summarizing the SPD-induced microstructural evolution [126]. The grain subdivision mechanisms and corresponding development of dislocation structures govern the microstructural evolution of the materials under SPD processing, and five grain refinement stages are involved in the process. To summarize the whole procedure of the grain refinement, it then can be simplified as follows, I: formation of large size dislocation cell blocks containing dislocations and dislocation cell structures; II: formation of microbands and transformation of some early dislocation cells into cell blocks; III: formation of lamellar sub-grains containing large quantities of dislocations; IV: formation of well-developed lamellar sub-grains and some equiaxed sub-grains; V: homogeneous distribution of equiaxed ultrafine grains or nano-grains.

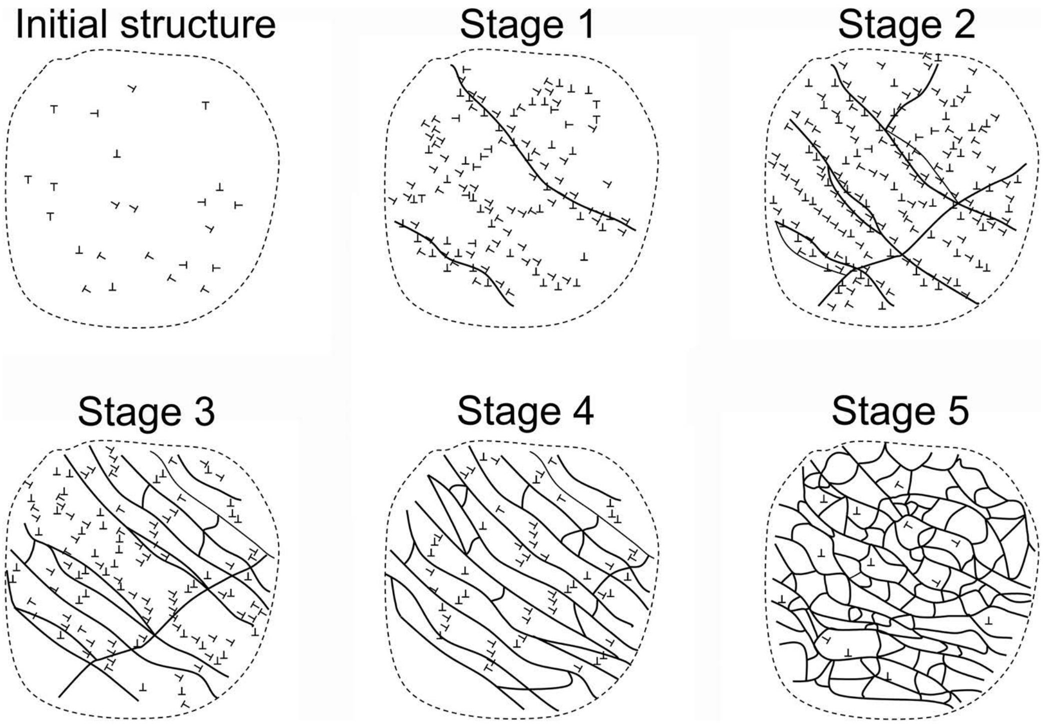

Figure 2.14 Schematic illustration of the five grain refinement stages, formed sequentially throughout the microstructural evolution during SPD [126].

However, this dislocation slip controlled mechanism works in materials which have high SFE and medium values of SFE. In contrast to such metals, grain refinement in materials with low SFE is primarily achieved through twin fragmentations since their deformation involves not only dislocation glide but also deformation twinning [137–139]. With the SFE decrease in the materials such as CuAl binary alloys [138], the competition between dislocation glide and deformation twinning becomes more pronounced during SPD. According to dislocation theory, twinning stress remarkably decreases with a reduction of SFE, while slip stress is relatively insensitive to SFE [113]. When the SFE is below a critical value, the deformation mechanism is primarily governed by twinning activities at RT and at a low strain rate.

In addition, experimental conditions can affect the microstructural evolution and the final mean grain size as well. Generally, the mutual influences of strain rate and temperature on deformation behavior can be expressed through a single parameter Z (Zener–Hollomon parameter) [140] as

$$\ln Z = \ln \dot{\varepsilon} + \frac{Q}{RT} \tag{2.20}$$

where $\dot{\varepsilon}$ is the strain rate, Q is the activation energy for diffusion, R is the gas constant, and T is the deformation temperature. Tao et al. [141] found that as Z increases, the grain size decreases and the tendency for twinning increases in pure Cu and a large fraction of deformation twins reduces the overall GB energy, which suggests that high strain rates and cryotemperatures provoke twinning and grain refinements.

According to studies with ECAP method from An et al., the grain refinement evolution in low/medium SFE Cu-Al binary alloy (i.e. 7 mJ m^{-2} for Cu-4.5 wt. % Al and 37 mJ m^{-2} for Cu-2 wt. % Al) is as follows [142]. At the first stage I, dislocation slip played a decisive role in shaping the microstructures finally characterized by ultrafine grains. The main grain refinement mechanism in materials with high SFE such as Al and Ni (SFE values of 166 and 128 mJ m^{-2}, respectively) is predominantly controlled by extensive dislocation activities [143–145] and is nearly independent on external loading conditions (lnZ) with values from 20 to 70 endowed by most SPD processing [146–148]. At stage II, the competition between dislocation slips and deformation twinning leads to a mixed microstructure of nanoscale twins, nanosized grains, and ultrafine grains. The volume fraction of twins and nanograins significantly increased with a decreasing SFE or enhanced ln Z. At stage III where the value of ln Z was beyond a critical value that decreased with lowering SFE and the effect of ln Z was dysfunctional because of the low level of SFE, although dislocation activities were still observed, deformation twinning primarily engraved the post deformation microstructures, labeling nanoscale twins and nanograins as typical microstructural features.

Wang et al. also investigated a low SFE alloy, Cu–30 wt. % Zn, processed with HPT to observe different deformation stages from UFG to nano-grain sizes and concluded the grain refinement process by five steps [126,149]. At step 1, equiaxed ultrafine grains are divided into twin lamellae. At step 2, continuous accumulation of dislocations at the twin boundaries gradually bends the originally atomically flat coherent twin boundaries and transforms the twin boundaries into semi-coherent twin boundaries. At step 3, under further straining the semi- coherent twin boundaries completely lose the coherency and transform into high angle grain boundaries. At step 4, secondary stacking faults and twins subdivide the lamellar grains into rhombic domains. At step 5, the secondary twin boundaries transform into incoherent high angle grain boundaries as noted earlier for the primary twin boundaries, and equiaxed nanograins are formed. The mechanism is illustrated schematically in Figure 2.15.

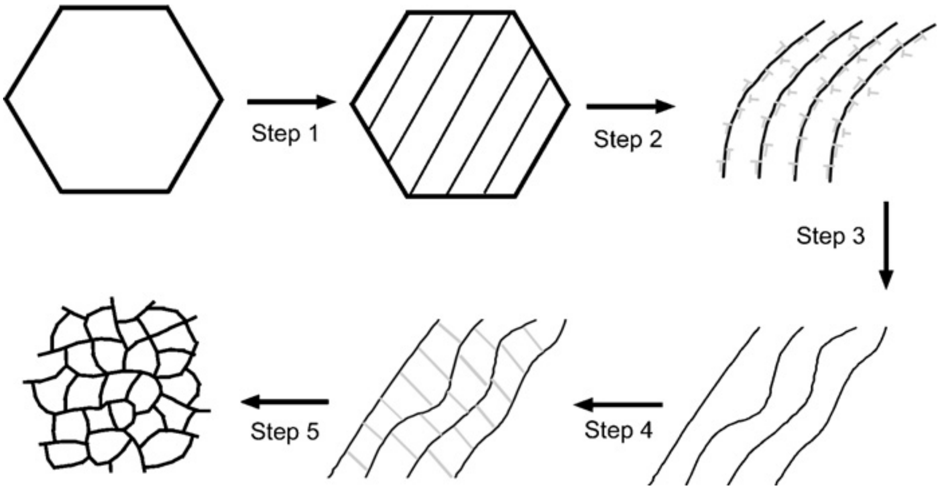

Figure 2.15 Schematic illustration of the grain refinement mechanism for the Cu–30 wt. % Zn alloy processed by HPT [149].

In this section, extensive dislocation activities-controlled grain refinement mechanism in high SFE materials and twinning fragment interaction-controlled grain refinement mechanism in low SFE materials is presented, respectively. This deformation and microstructure maps not only provide us with an excellent opportunity to profoundly comprehend deformation behavior and the nature of grain refinement during SPD but also present promising strategies to finely tune microstructures to achieve superior properties for technological applications.

2.3.3 Influence of various factors on grain refinement by SPD

Although SPD methods are extremely effective to refine grains by applying large strains, there are some limitations existing in the SPD processing which can affect the saturation grain size, such as temperature, pressure, alloying elements and so on.

Pressure is one parameter which can be easily controlled with using HPT. The HPT experiments under different pressure were performed with Armco iron and copper by Wetscher et al. [150]. The microstructure evolution of during deformation under different hydrostatic pressures (1.9, 3.7 and 5.7 GPa) was analyzed. They found that the grain size is somewhat smaller at higher pressures, however, the effect is, even if, very small. Additionally, only a very small influence of the hydrostatic pressure on the resulting microstructure and the tensile strength on Armco iron and copper samples deformed by HPT could be observed. Zhilyaev et al. described the influence of the applied pressure from 1 to 9 GPa on the microstructure of Ni [151]. With higher pressure applied, the microstructures are more similar both at the periphery and in the center of the disk which indicates that a saturation was reached earlier. Hence, the accumulated strain could be the core factor which lead to the microstructure evolution.

Deformation temperature can affect the atomic diffusion and the microstructure evolution and subsequently the average grain size [148,152,153]. Rathmyar et al. investigated the influence of deformation temperature on pure Ni (99.99) and Ni (99.79) with added impurity elements (C, Cu, Fe, Mn and Si) [154]. Ni99.79 deformed at liquid nitrogen temperature (LNT) achieved the finest microstructure with an average grain size of about 50 nm while around 200 nm at 400 °C, shown in Figure 2.16. The largest grains were observed in the Ni99.99 deformed at 400 °C with an average grain size about 1.4 μm whereas the mean grain size is ~200 nm deformed at -196 °C, much smaller than 400 °C sample. Wang et al. studied the effect of deformation temperature on the microstructure developed in high-purity aluminum processed by ECAP at different temperatures [155]. The results indicated that the grain sizes are 0.55, 0.59, 0.9 and 2.2 μm increasing with the deformation temperature increasing from 298 K to 523 K. Similar results were also found in pure Fe, a high alloyed ferritic steel and an austenitic steel [156]. However, dynamic recovery, dynamic recrystallization and GB migration are thermally activated at evaluated temperature which can lead to grain growth [157–160]. One should be aware that low temperature SPD can significantly increase the stored energy in materials. The high stored energy in the form of lattice defects decreases the activation energy and increases the rate of recrystallization [161]. In addition, one other factor that affects the minimum grain size at SPD can be established from the analysis of Figure 2.16, namely, the influence of the impurities or alloying comparing of pure Ni99.99 and solutes atoms added Ni99.79. Ni99.99 had larger grain size than Ni99.79 after processing by HPT both at -196 °C and at 400 °. In Table 2.2, the most important parameters influencing the minimum size of the crystallites under certain SPD conditions and the necessary strain to reach the saturation point have been evaluated by Pippan et al. [156].

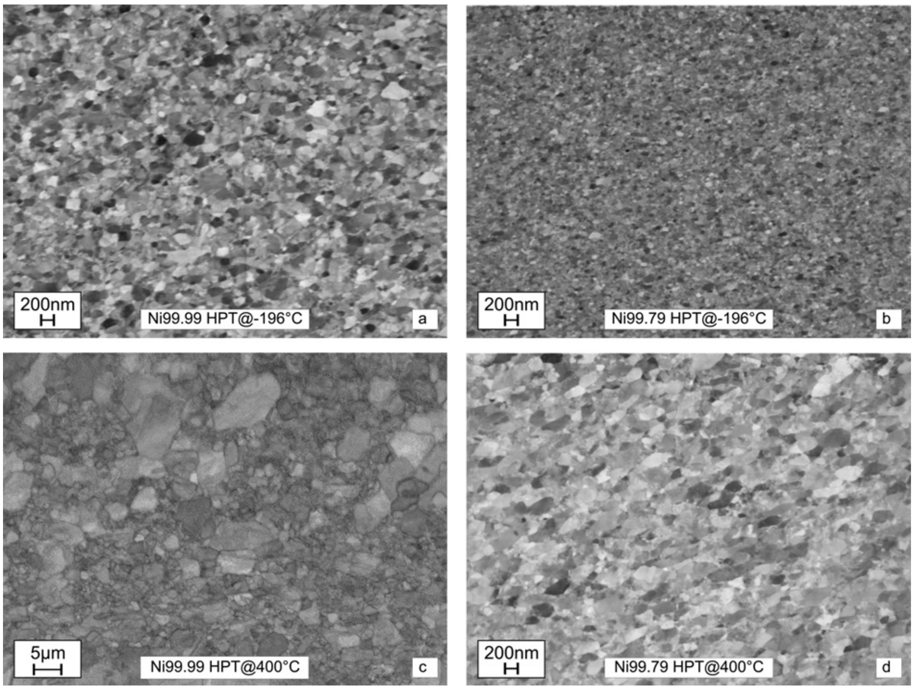

Figure 2.16 BSE images of saturation microstructure of Ni99.99 and Ni99.79 at -196 and 400 °C [154].

Table 2.2 Effect of different parameters on the onset strain of saturation and the size of the structural elements, grain size, in the saturation region [156].

	Grain size at saturation	onset strain of saturation
temperature	very high	very high
strain rate	medium	medium
strain path	high	medium
pressure	low-medium	low
alloying	very high	medium
precipitations	high	?
crystal structure	low	medium
stacking fault energy	medium	?

2.4 Nanocrystalline HEAs

Cantor type FCC HEAs have attracted increased attention in the past decade largely because of its excellent mechanical properties, especially at cryogenic temperature [7–9,59,162–167]. Commonly, the FCC structured Cantor alloy system shows much higher ductility but lower strength. Therefore, a number of investigations of FCC HEAs processed by SPD methods were performed to obtain high strength and reasonable ductility with subsequent annealing procedure [168–176]. For instance, the yield strength value of nano-grained CoCrFeMnNi alloy can reach 1.0 GPa and 1.75 GPa directly after ECAP and HPT, respectively [171,173,174]. Han et al. produced nanocrystalline CoCrFeMnNi alloy by means of ARB and subsequent annealing treatment at 800 °C [167]. The resulting samples demonstrated a superior combination of RT strength and ductility with a yield strength of 700 MPa and a 54 % uniform elongation. However, various precipitates were formed in the nano crystalline CoCrFeMnNi alloy processed by HPT during the annealing in temperature range from 450 to 750 °C [174], which led to a brittle fracture in tensile test. Deformation mechanisms and microstructure stability issues of nanocrystalline metallic materials will be presented in the next subsection.

2.4.1 Deformation behavior in nanocrystalline state

Mechanical behavior of nanocrystalline materials has been studied for decades. Generally, the contributions of nanocrystalline structure to the strength can be obtained/estimated from Eq. (2.4). However, very strong grain refinement may lead to lower yield stress as shown in Figure 1.2 in Chapter 1. The inverse Hall–Petch behavior was first reported by Chokshi et al. by performing measurements on nanocrystalline Cu and Pd samples made by IGC, when both metals exhibited a negative slope of the "Yield Strength vs. $d^{-1/2}$" plot [177], which was subsequently observed in other materials by other researchers [178–181]. The Hall–Petch trends for a range of grain sizes from the micro to the nano scale are plotted in Figure 2.17 for Cu, Fe, Ni and Ti [182]. Note that the data points in the conventional polycrystalline range for the majority of such plots overlap while they are more spread out in the nanocrystalline range. The Hall–Petch plot for the nanocrystalline range clearly shows a deviation from the regular trend in the microcrystalline range. There is a significant decrease in the slope for small grain sizes. However, there is no agreement about the nature of such behavior at grain sizes below ~10–15 nm. Though researchers have debated the existence of the negative Hall Petch effect, there is insufficient information to validate the existence of this effect. The most probable behavior is that the yield strength plateaus below a critical grain size. Although the strengthening and deformation mechanism in conventional coarse/fine/UF grained materials are well understood, there is still some widespread disagreement in nanostructured materials since inverse Hall–Petch phenomenon was proposed by Chokshi et al. [177].

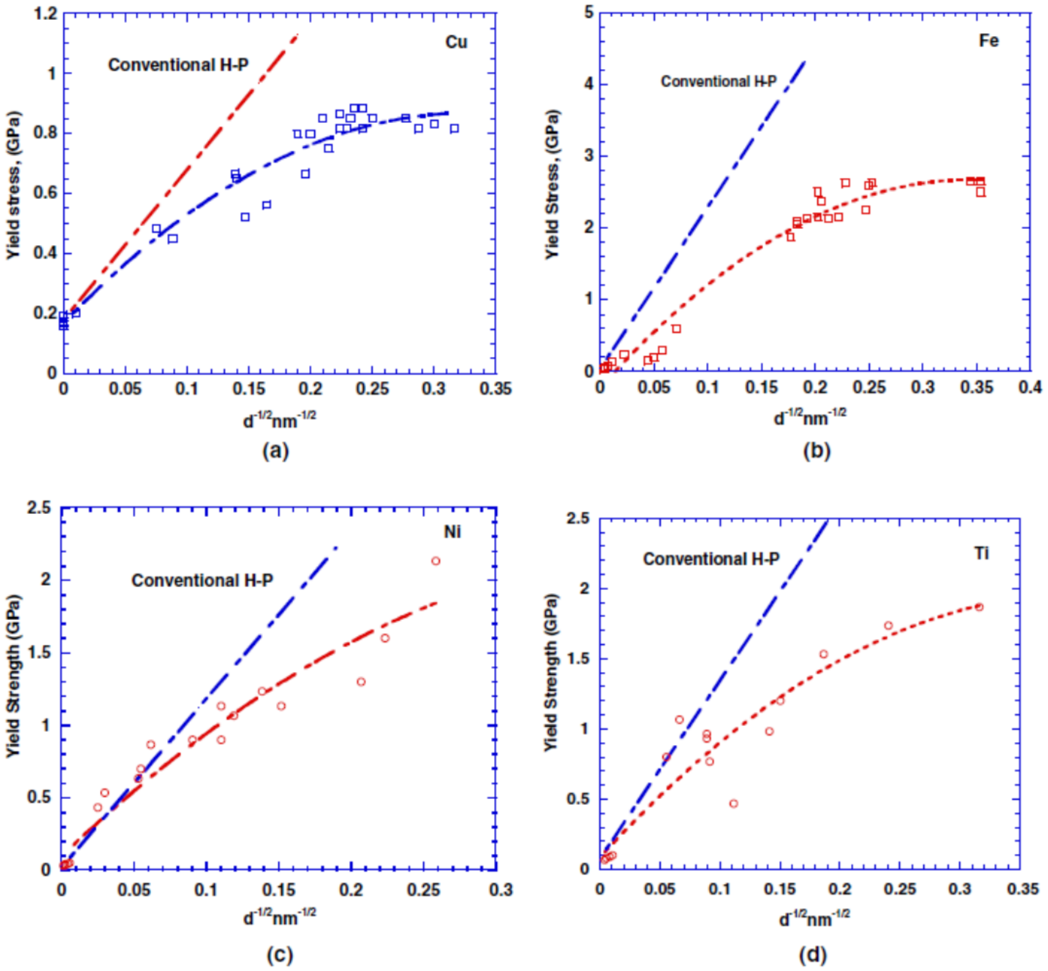

Figure 2.17 Plots showing the trend of yield stress with grain size for different metals as compared to the conventional Hall–Petch response: (a) copper, (b) iron, (c) nickel and (d) titanium [182].

In order to explain the deviation from the Hall–Petch relationship in nanocrystalline materials, a concept of the dislocation pile-up breakdown was generally accepted. As the grain size is decreased, the number of dislocations piled up against a grain boundary also decreases, at a fixed stress level, since this number is a function of the applied stress and of the distance to the source. Conversely, an increased stress level is needed to generate the same number of dislocations in the pile-up with decreasing of the distance to the source. At a critical grain size, the concept of a pile-up cannot be used any more to explain the plastic flow [182]. As the grain size is reduced to the nanocrystalline regime, the number of dislocations in the pile-up is eventually reduced to one. Thus, the multiplying effect on the stress field is lost [183,184]. Wadsworth, Nieh [185] and Pande [184] predicted the model to explain at which grain size the Hall–Petch relationship would break down by assuming the critical condition.

Grain-boundary sliding is another important deformation mechanism [186], which is in principle to explain the phenomenon of super plasticity. For nanocrystalline materials, this has been proposed to be the dominant deformation mechanism at grain sizes <50 nm. Hahn et al. proposed two hardness relationships as follows [187],

$$H_\mathrm{v} = H_0 + \frac{k}{\sqrt{d}} \tag{2.21}$$

$$H_\mathrm{v} = H_{\mathrm{v}0} - \frac{m_1}{d}(d - m_2)^{\frac{1}{2}} \tag{2.22}$$

where m_1, m_2, and k are material parameters, d is the mean grain size. Eq. (2.21) is used in the dislocation dominated regime while Eq. (2.22) is valid in the grain boundary sliding regime. Raj and Ashby [42] proposed that plastic deformation between neighboring grains occurs by diffusion alone [186]. Taking the grain boundary diffusion and bulk diffusion into account, one can get the grain boundary sliding rate as,

$$\dot{u} \approx \frac{2\delta\Omega D_B}{kT}\tau_\alpha\left(\frac{1}{h^2}\right) \tag{2.23}$$

where δ is the thickness of the grain boundary, Ω is the atomic volume, and h is the amplitude of the wave, τ_α is the shear stress and D_B the boundary diffusion coefficient. If it was assumed that the grain boundary generates identical sliding rate and h is taken as $d/4$, one can get the strain-rate after simplification,

$$\dot{\gamma} = \left(\frac{1}{\eta_e}\right)\tau_\alpha \tag{2.24}$$

where η_e is an effective viscosity. This is the equation for Newtonian viscous flow. Along with the decrease of h, the strain-rate will increase, suggesting that shear localization tends to occur in the nanomaterials. Attributed to this theory, it is concluded that grain-boundary sliding can contribute to the plastic deformation at grain sizes less than 10 nm [181,188,189].

Ma and co-workers proposed that nano grains can rotate during plastic deformation and coalesce along directions of shear, creating larger paths for dislocation movement [190–192]. The planes with highest Schmid factor were represented by the short dark lines inside the grains in Figure 2.18 (a). The applied shear stress could make the neighboring nano grains to rotate from the closer to the same orientation as shown in Figure 2.18 (b). The elimination of grain boundaries as represented by Figure 2.18 (c) could provide the larger free path for dislocation motion. However, this mechanism leads to the strain softening and localization as observed in the nanocrystalline materials. It was suggested as an alternative deformation mechanism to grain boundary sliding [193].

There are also other mechanisms which are regarded to operate in nanocrystalline materials such as shear-band formation [194], twinning [190,195] and grain boundary dislocation nucleation and annihilation [196,197], but they are not presented in this section.

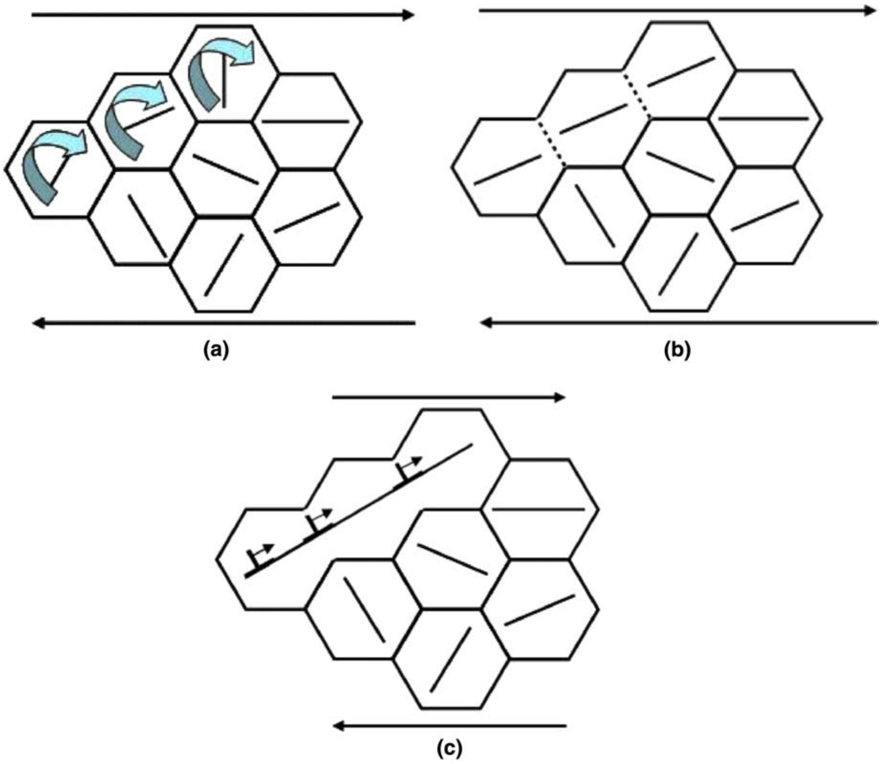

Figure 2.18 Model of (a) the rotation of nano grains, (b) annihilation of grain boundary, and (c) coalescence of nano grains [182].

2.4.2 Thermal stability of nanocrystalline HEAs

CoCrFeMnNi HEA was one of the first equiatomic HEAs reported to crystallize as a single phase FCC solid solution, however, it was later discovered that it decomposes into metallic (Cr-rich BCC) and intermetallic ($L1_0$-NiMn and B2- CoFe) phases after a 500-day anneal at 500 and 700 °C [198]. The decomposition and phase transformations can occur very quickly reported by Schuh et al. when the alloy is in the nanocrystalline state [174]. The results point out that after 5 min anneal at 450 °C, particles of NiMn and Cr rich precipitated in the nanograined matrix and a CoFe phase formed after 15 h. The chronological sequence of the precipitation of these phases can be rationalized by considering their relative diffusivities. Tsai et al. presented the interdiffusion coefficient in CoCrFeMnNi system HEAs and showed that the sequence of elements in the order of decreasing diffusion rate is: Mn, Cr, Fe, Co and Ni [34]. The element that diffuses fastest at a fixed temperature is Mn, which is consistent with the formation of the MnNi phase first. The second phase to form has a very high Cr concentration, which has the next highest diffusion coefficient. Only after longer annealing times the CoFe phase forms, which consists of elements that have the next highest diffusion coefficients after Mn and Cr [174]. Additionally, the intrinsic nature of nanocrystalline grains also contributes to the kinetics of phase formation. This fast formation of new phases can be attributed to the role of grain boundaries in diffusion controlled precipitation and phase formation processes in nanocrystalline alloys [199,200]. The abundant grain boundaries in the nanocrystalline HPT-processed CoCrFeMnNi alloy offered many fast diffusion pathways and nucleation sites to facilitate the phase decomposition. Mantha et al. utilized in-situ transmission electron microscope heating to elucidate the sequence of phase decomposition of nanocrystalline $Co_{26}Cu_{10}Fe_{27}Mn_{10}Ni_{27}$ HEA processed by HPT [201]. The alloy was heated from 100 to 420 °C within 7 h which showed that the diffusion of elements starts at 250 °C, initially with Ni, Cu and Co segregating to the grain boundaries and Fe and Mn are depleted from the grain boundaries. Subsequently, B2 precipitates were observed to form at triple junctions at 340 °C and their size continued to increase till 400 °C, whereas Ni, Cu and Mn were still segregated at the grain boundaries. Li et al. investigated a segregation behavior in a fully recrystallized CoCrFeMnNi HEA aged at 450 °C for 6, 18 and 48 h [202]. A following sequence for phase decomposition at grain boundaries was supposed: (i) Ni and Mn co-segregate to the grain boundaries; (ii) at other grain boundaries regions which are devoid of Ni and Mn segregations, Cr is the first of these elements that starts segregating to the grain boundaries; (iii) with further uphill diffusion inside the grain boundaries plane during aging, the Gibbsian enrichment in solutes, mainly Ni and Mn, shifts the local thermodynamic state of the grain boundaries into a Spinodal regime of the reference phase diagram which leads to a Spinodal decomposition at 450 °C; (iv) these local Spinodal enrichments forming at the grain boundary planes act as compositional precursor states to the more stable equilibrium phases, one being the NiMn phase and the other one possibly being a Cr-rich phase.

According to the above researches, it seems that all the significant segregation processes occur during 300-700 °C in CoCrFeMnNi type FCC HEA, no matter coarse grained ones or nanocrystalline. Significant segregations of Co, Ni and Cu to the grain boundaries occurred in a low temperature range from 250 °C to 300 °C in nanocrystalline FCC structured CoCuFeMnNi alloy [201]. They observed the formation of NiMn, Cr and CoFe multiple secondary phases of nanocrystalline CoCrFeMnNi after heat treatments at 450-500 °C. They showed that the Cr rich σ phase can have detrimental effect on the mechanical properties.

The recrystallization phenomenon occurred after anneal at 750 °C was observed previously, which lead to a single FCC phase was observed in [167,171,173,174]. Normally when recrystallization occurs during heat treatment of cold deformed alloys, the generation of small grains is observed, which grow continuously and eventually replace the deformed microstructure. In this process, characterized by nucleation and nucleus growth, is referred to primary recrystallization. It involves dislocation recovery, annihilation and sub-grain formation as shown in Figure 2.19. Since the dislocation density in the material is not recovered homogeneously but discontinuously at moving grain boundaries, it is also termed as discontinues recrystallization. In contrast, after severe plastic deformation or in case that grain boundary migration is strongly impeded, for instance by dispersion of a second phase, strong recovery can occur. Due to the high volume fraction of grain boundaries, however, the nanocrystalline materials are in relatively high energetic states and have a relatively strong tendency to reduce the total grain boundary area to diminish the internal energy, which produces high susceptibility to grain coarsening [203–205]. Grain growth at low temperature, even RT, has been observed in many nanocrystalline metals that limits engineering applications of this kind of materials Therefore, studying the thermal stability of nanocrystalline materials has been becoming a highly important topic in the field of nano-processing and application.

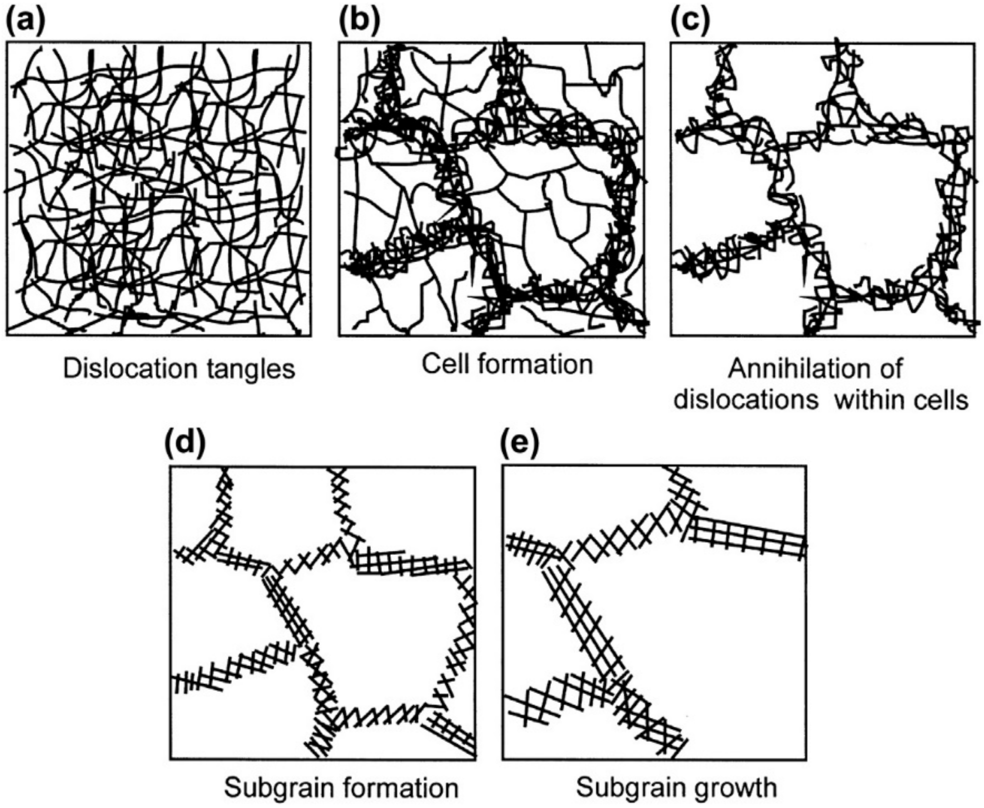

Figure 2.19 Various stages in the recovery of a plastically deformed material [206].

2.5 Motivation and objectives

Since the CoCrFeMnNi single FCC phase HEA was discovered, numerous attempts were undertaken to improve its mechanical properties. For examples, applying following strategies: SPD in combination with anneal [167,170,173,174,176], interstitial alloying [14,54,56,57,94,207] and precipitation by minor composition tuning [68,77,79,82,83]. Nevertheless, it seems that all the methods still have limitations for further improvement of a combination of the strength and ductility.

Carbon, as the most effective and common interstitial atom, not only contributes to the solid solution strengthening, but also increases the lattice friction stress leading to a disturbance of a local stress field, finally promoting an increase of strength and maintaining the ductility [13,14]. As interstitial carbon possesses a much larger mobility compared to substitutional elements, it should preferentially interact with dislocations or grain boundaries [208]. Thus, carbon can outperform the effect of other substitutional elements in the process of SPD. For example a saturation grain size of 160 nm was reached in pure nickel after HPT, whereas the mean grain size in nickel containing1200 ppm carbon was reduced to 90 nm at the same deformation conditions [154]. Excessive dose of carbon content will still donate to the interstitial strengthening effect, however, it will deteriorate ductility significantly due to the precipitation of carbides at grain boundaries [207]. During SPD, carbides also play an important role in the process. In pearlitic steel, plates or lamellae of cementite can be severely deformed to very high degrees of plastic strain and even dissolve, resulting in lamellar structures consisting of a carbon-rich interlayers allowing the stabilization of lamellae with ~10 nm spacing and the carbon-rich boundaries [209,210]. As a whole, appropriate carbon content alloying can effectively reduce the grain size after SPD providing effective obstacles to grain boundary motion and expanding the thermal stability range. The saturation microstructures of the HEAs after SPD may differ as the carbon content increasing.

One can expect that carbon content in the nano/ultra-fine-grained alloys processed by SPD may lead to completely different mechanical properties. For example, carbon alloying can significantly reduce the grain size of the alloy after SPD processing, which will result in the increase of yield strength according to the Hall-Petch law.

As mentioned above, the CoCrFeMnNi alloy demonstrates a yield strength up to 1.75 GPa after SPD with a rather low fracture elongation [171,173,174] To balance the strength and ductility of the SPD processed HEAs, subsequent anneals are usually performed. However, in the nanocrystalline CoCrFeMnNi alloy, a large number of hard precipitates appeared after annealing in the temperature range 450-750 °C leading to a brittle fracture in tensile tests [174]. These precipitates are CoFe phase, Cr rich sigma phase and NiMn phase [174]. Though there are some indications of annealing induced hardening in the SPD processed alloys, the information about the precipitation and segregation behaviors of the nanocrystalline HEA is still sporadic [174,201,211–213]. In particular, carbon alloyed nanocrystalline HEAs haven't been systemically investigated in respect of their mechanical properties and thermal stability so far.

Utilizing the Thermo-Calc software, the equilibrium phase diagrams in CoCrFeMnNi-C system were calculated as shown in Figure 2.20 [99]. One can clearly see that a decrease in the Cr molar fraction from 1 to 0.25 greatly extended the single FCC phase field towards the higher carbon concentrations, as Cr is a strong carbide forming element [57]. Given a strong solid solution strengthening effect of carbon, a reduction in the Cr content with an addition of carbon can be considered as a promising alloying strategy.

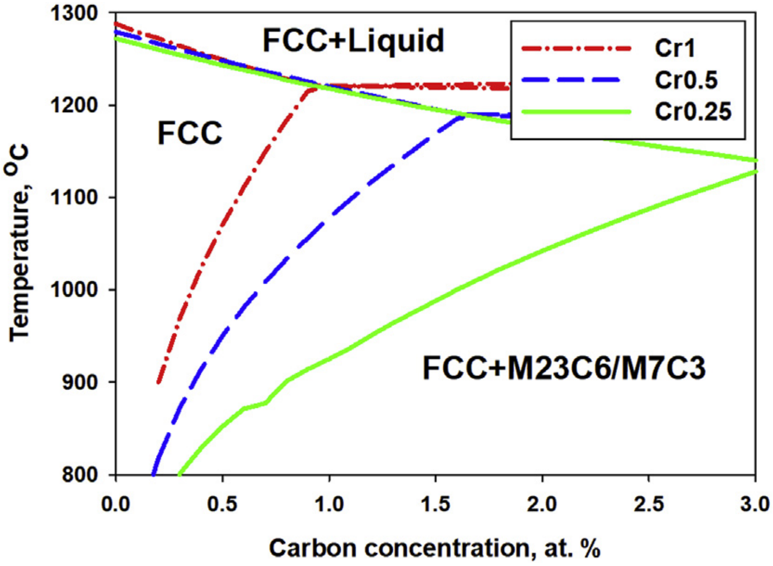

Figure 2.20 Boundaries of the single FCC phase field in the carbon-doped $Co_1Cr_xFe_1Mn_1Ni_1$ alloys (subscripts indicate the molar concentrations of the respective elements) depending on the Cr and C concentrations [99].

Consequently, in this dissertation, we combined the SPD and carbon interstitial alloying effect in Cr reduced CoCrFeMnNi alloy to explore whether we can further improve the mechanical properties. Simultaneously, the microstructure evolution from coarse grained to nanosized one was investigated during the shear strain increasing in HEAs with different carbon content. Then, the post deformation anneal was conducted on nanocrystalline HEAs to seek an optimal combination of strength and ductility and the thermal stability was studied during annealing processing as well.

Therefore, the detailed objectives of present dissertation are as follow,

To study the influence of carbon alloying on the deformation mechanisms and microstructure formation during severe plastic deformation by high pressure torsion at different stages of plastic deformation in HEAs using $CoCr_{0.25}FeMnNiC_x$ as a model system. For that purpose, the resulting microstructure formation, evolution and thermal stability will be systematically investigated as a function of processing conditions (HPT) with a number of different methods (XRD, TEM, APT, SEM).

It is anticipated that the results of this dissertation will precisely reveal the influence of alloying on the microstructure evolution during deformation by HPT and subsequent annealing. In particular, it is anticipated that under these conditions of strain and temperature deformation twinning will be suppressed, which would result in a pronounced effect on mechanisms and kinetics of the microstructural evolution and respective mechanical behavior. In addition, different grain sizes will be produced in severely deformed samples by annealing at various temperatures.

Subsequently, the experimental data base for the mechanical behavior of ultrafine-grained $CoCr_{0.25}FeMnNiC_x$ alloys should be established for a set of different microstructures (grain size, volume fraction of twins, precipitates like carbides and intermetallic particles) with a number of different methods using special mechanical testing equipment. Additionally, studying the thermal stability of the ultrafine grained structures in the alloys at elevated temperatures is essential during the annealing processes. The behaviors of elements segregation, new phase precipitation, phase decomposition and grain growth will be investigated systematically.

Finally, the alloy compositions will be identified, which, after SPD and subsequent thermal treatment, will result not only in superior strength, but also reasonably high ductility.

3 Experimental

3.1 Experimental material

3.1.1 Materials synthesis

The HEA composition was designed based on CoCrFeMnNi Cantor alloy but with reduced Cr content, as discussed in the previous section, as $Co_1Cr_{0.25}Fe_1Mn_1Ni_1$, where the subscripts indicate the molar fraction of the respective components [12]. The ingots were produced from mixtures of pure (≥ 99.9%) constitutive elements by vacuum induction melting with different carbon content (0, 0.5, 1.0, and 2.0 at. %, nominally) addition. Each ingot had a slab shape around 60×40×17 mm^3 weighting ~400 g. Cylinders with the diameter of 15 mm were machined from the produced ingots. Subsequently the cylinders were cut to disks with a thickness of 0.7-0.8 mm for further HPT process. The results of chemical composition measured by energy dispersive X-ray spectroscopy (EDX) for metallic elements and hot gas carrier method for carbon content are shown in Table 3.1. Despite the metallic elements constitutes reveal some fluctuation, the concentrations, including carbon, are close to the nominal ones.

Table 3.1 Chemical composition of the as-cast alloys (at. %).

Nominal C content	C	Cr	Co	Fe	Ni	Mn
0	0.038±0.09	6.23±0.05	23.41±0.18	23.81±0.05	22.72±0.21	23.82±0.22
0.5	0.521±0.045	6.30±0.08	23.33±0.19	23.33±0.28	22.93±0.12	23.62±0.32
2	2.136±0.182	6.46±0.08	23.01±0.25	22.32±0.21	21.24±0.47	24.77±0.45

3.1.2 HPT process

HPT experiments were performed using the machine manufactured by W. Klement GmbH with capacity of 250 tons with a test temperature range from 77 K to 673 K, shown in Figure 3.1 (a). Pressure and torsion are recorded by electronic sensors, which assure a stable progress. Each disk was grinded with a SiC paper (P240) before HPT experiment to remove surface oxidation due to cutting procedure. HPT was performed at RT under a hydrostatic pressure of 6.5 GPa for 0.5, 1 and 3 turns with the rotation speed of 0.5 rpm. The samples before and after HPT are demonstrated in Figure 3.1 (b). The specimens under the study were identified as CxNy, where x means the nominal C content for each alloy and y denotes the number of revolutions during HPT. The von Mises equivalent strains at HPT can be calculated by Eq. 2.15 and Eq. 2.16.

To study the carbon diffusion during HPT at cryogenic temperature, $CoCrFeMnNiC_2$ alloy had been processed at 77K for three HPT turns at 6.5 GPa to compare with the sample having the same composition and processed for at the same HPT conditions at RT.

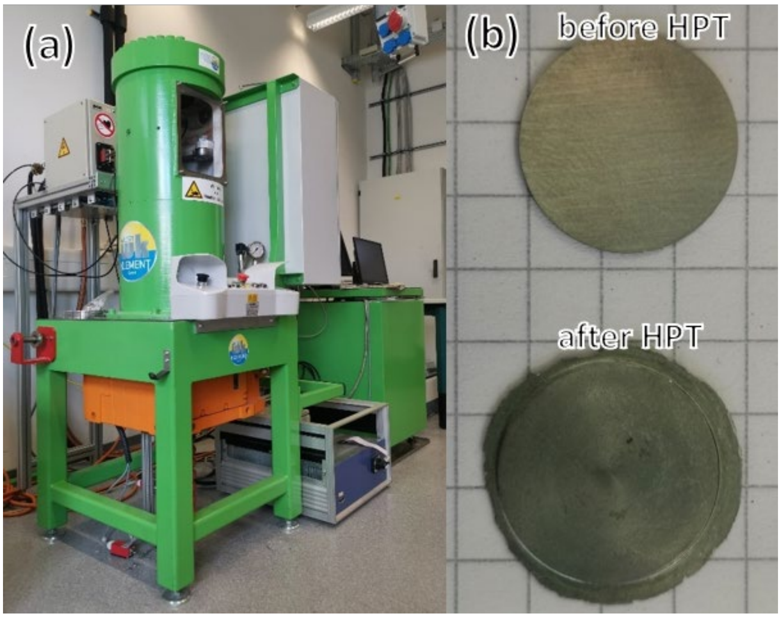

Figure 3.1 (a) HPT machine and (b) samples demo before and after HPT (black grids indicate 5×5 mm^2).

3.1.3 Post deformation anneal

In last a few years, some groups have studied the thermal stability of CoCrFeMnNi in coarse grain state [198,202], and in nanocrystalline state as well [171,172]. Therefore, in this dissertation, we focused on the thermal stability of nanocrystalline carbon added alloy, C2N3 sample. Differential scanning calorimetry (DSC) is a thermodynamical tool for direct assessment of the heat energy uptake, which occurs in a sample within a regulated increase or decrease in temperature [214]. The calorimetry is particularly applied to monitor the phase transitions. Therefore, the DSC measurements are very useful to determine the temperature of annealing procedures. There are of two types of differentials a heat flux illustrated in Figure 3.2 [215]. For power compensation DSC, the signal is related to the differential heat provided to keep the sample and the reference to the same temperature. For heat flux DSC, the signal derives directly from the difference of temperature between the sample and the reference and in that sense a heat flux DSC is similar to a differential thermal analysis.

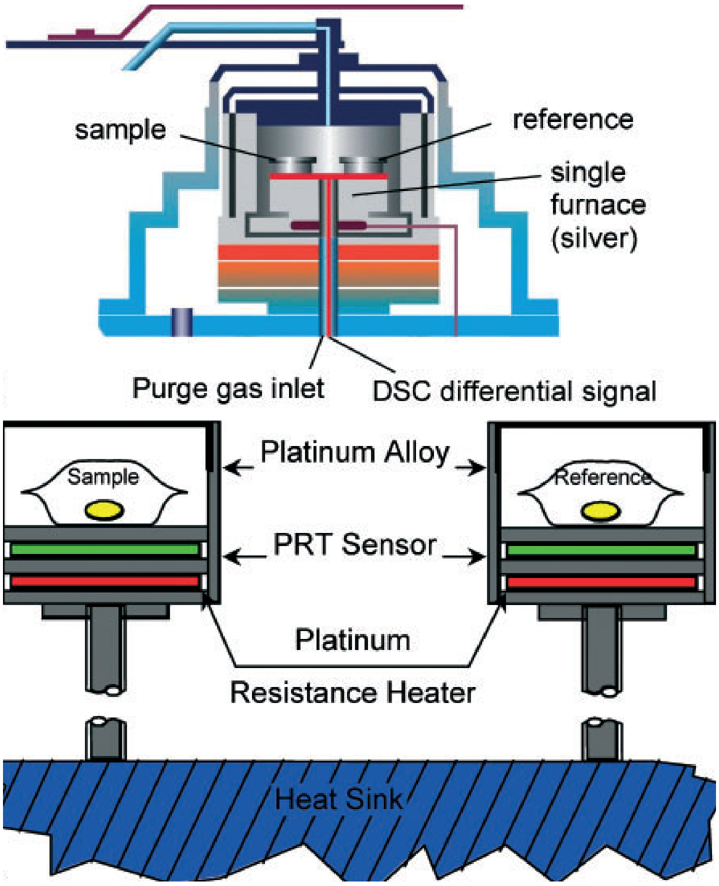
sample
reference
single
furnace
(silver)
Purge gas inlet
DSC differential signal
Sample
Platinum Alloy
Reference
PRT Sensor
Platinum
Resistance Heater
Heat Sink

Figure 3.2 Schematic cross-section of two types of differentials a heat flux DSC. (a) heat flux DSC, (b) power compensation DSC [215].

3.2 Characterizations

As the microstructure observations involve the phases identification and distribution, determination of defects density, microstructure morphology and elemental distribution, multiple characterization techniques were used in this dissertation, such as XRD, Scanning Electron Microscopy (SEM), TEM and APT.

3.2.1 Sample preparations

For all characterizations, the samples were firstly prepared by manual grinding with SiC paper (P240-P2400) and afterwards polished with diamond or alumina suspension (6-0.5 μm). For SEM and XRD measurements, the following electrolytic polishing was performed to completely remove strained layer induced by mechanical polishing. The electrolyte is a 10 % solution of perchloric acid ($HClO_4$) in ethanol (C_2H_5OH), and the polishing process was conducted under a direct-current voltage 20 V for 30-60 s at ~ -5 °C. TEM and APT samples were prepared using Focused Ion Beam (FIB) system, installed in SEM instrument. The detailed description of sample preparation by FIB will be illustrated in next sections.

3.2.2 X-ray diffraction

XRD, as a highly valuable technique, has been wildly used in materials research for determination of crystalline phases (phase analysis), preferable crystal orientations and determination of some microstructure features. Interaction of X-rays with crystalline lattice can cause an interference pattern of the waves present in an incident beam of X rays due to the uniform spacing of atoms in a crystal. A description of XRD was first proposed by Lawrence Bragg and William Henry Bragg in 1913, which can by described as Bragg equation [216],

$$n\lambda = 2d\sin\theta \tag{3.1}$$

where n is the diffraction order, λ is the characteristic wavelength of the incident X-rays, d is the lattice plane spacing and θ is the incident angle. A diffraction pattern is obtained by measuring the intensity of scattered waves as a function of scattering angle. Strong intensities known as Bragg peaks are obtained in the diffraction pattern at the points where the scattering angles satisfy Bragg condition which highly match the Eq. (3.1). The obtained XRD patterns contain huge amount of information such as lattice parameter, phase composition, preferred orientation and so on. Hence, X-ray line profile analysis was developed to extract this information , i.e. Rietveld refinement [217].

In this work, samples were examined by Philips X'Pert powder diffractometer with a Cu-K_α radiation source (λ = 1.5406 Å). The measurements were carried out in a 2θ range of 20-100°, with a step size of 0.02° and step time of 20 s at 40 mA and 45 kV. The lattice parameters were evaluated by an X'Pert High Score software using a Rietveld analysis. The strain and crystallite size were evaluated using a Convolutional Multiple Whole Profile fitting method (CMWP) [218] and this part of the work was performed in collaboration with Prof. Ungár (Eötvös Loránd University, Budapest). It should be noted that dislocation densities are only estimated based on an XRD analysis, which is critical for nanocrystalline materials.

3.2.3 Scanning Electron Microscopy

The scanning electron microscope is one of the most versatile instruments available for the examination and analysis of the microstructural characteristics. A major reason for the SEM's usefulness is the high resolution which can reach 1-5 nm now for commercial instruments image mode. One significant point it the capability to determine the crystal structure and grain orientation with equipped electron backscattering diffraction (EBSD) system. Similarly, SEM equipped with characteristic x-ray detectors can also be used to obtain compositional information using characteristic x-rays, which is EDX. Backscattered and secondary electrons are generated within the interaction volume which form images in SEM. These signals are capable of collecting the information of composition, shape, texture and thickness [219].

FIB system is usually installed together with SEM. Gallium ion sources is one of widely used liquid metal ion sources and plasma beams of noble gas ion such as xenon are also more and more available recently [220]. FIB is commonly used for materials removal and deposition, such as sample milling for TEM lamellae and depositing metals as sacrificial layers based on chemical vapor deposition. A schematic of SEM and FIB system is illustrated in Figure 3.3.

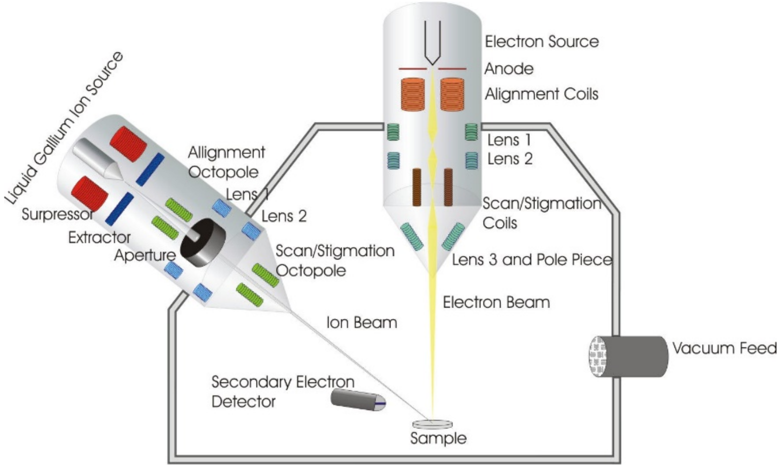
Electron Source
Anode
Alignment Coils
Lens 1
Lens 2
Scan/Stigmation
Coils
Lens 3 and Pole Piece
Electron Beam
Liquid Gallium Ion Source
Allignment
Octopole
Lens 1
Lens 2
Surpressor
Extractor
Aperture
Scan/Stigmation
Octopole
Ion Beam
Vacuum Feed
Secondary Electron
Detector
Sample

Figure 3.3 Schematic of the SEM and FIB machines, shown in a two-beam configuration [221].

FIB operando in this dissertation was performed with a FEI Strata 400 S equipped with a (Schottky) field emission gun as electron source and a Gallium liquid metal ion source. The Gas Injection System (GIS) contains Pt, W and C. The high voltage used for SEM imaging is 5 kV while 5- 30 kV range for FIB. An Omniprobe micromanipulator was used for sample lift out and transfer. Zeiss Auriga 60 equipped with a (Schottky) field emission gun was utilized for microstructure and fracture morphology observations. The SEM images were acquired with 4QBSD, In-lens SE and SESI detectors under a high tension from 5 to 20 kV and corresponding elemental analysis was conducted using an EDAX-EDX detector.

3.2.4 Transmission Electron Microscopy

Max Knoll and Ernst Ruska first invented the electron microscope at Berlin Technische Hochschule (now Technische Universität Berlin) in 1931 meaning a overcome the barrier to the higher resolution limited by visible light [222]. By the late 1930s electron microscopes with theoretical resolutions of 10 nm were being designed and produced, and by 1944 the resolution was further reduced to 2 nm. Later, developments in optics improved the resolution of TEM and the first practical STEM was developed in the late 1960s. At the same time, there were developments in combining analytical techniques like EDX [223] and electron energy-loss spectroscopy (EELS) [224] with TEM. A significant development in the history of TEM was the introduction of aberration correctors capable of correcting spherical aberrations during late 1990s, which remarkably improved the resolution limits [225]. With the developments in sample preparation and instrumentation, sub-angstrom resolution is reached with the capability of atomic scale analytical measurements. With the possibility of atomic resolution imaging and analytical capabilities, TEM is one of the main structural characterization tools used in wide range of research areas.

The basic illumination system of a TEM consists of the gun and condenser lenses and their role is to take the electrons from the source and transfer them to the specimen. The objective lens and the specimen stage system is the heart of the TEM. The imaging system uses several lenses to magnify the image produced by the objective lens and to focus these on the viewing screen or computer display via a detector. The two imaging modes commonly used in a TEM are diffraction mode and imaging mode and the schematic is shown in Figure 3.4 [226]. In both imaging and diffraction modes, a parallel beam formed by the condenser system is used to illuminate the region of interest of the specimen. After interacting with the specimen, the transmitted electrons (scattered and unscattered) are focused by the objective lens, forming an image at the intermediate image plane and a diffraction pattern at the back-focal plane (BFP) of the objective lens. Operation in imaging and diffraction mode can be switched by tuning the strength of the intermediate lens to focus on the intermediate image plane for imaging or the BFP for diffraction. In imaging mode, BF and DF images can be obtained separately by selecting the unscattered (direct) beam or a scattered beam for imaging. The BF images originates from two types of amplitude contrast: mass-thickness contrast and diffraction contrast. As its name implies, mass-thickness contrast depends on the mass (related to the atomic number Z and density) and thickness of the specimen, with higher Z and thicker regions scattering more electrons, thus reducing the intensity of the direct beam and causing these regions to appear darker in the image. Mass–thickness contrast dominates mainly for non–crystalline materials while diffraction contrast is more important for crystalline specimens, where the intensity of the BF image highly depends on the orientation of the crystal and the diffracted beams excited and blocked by an objective aperture. In a DF image, only the regions of crystals where the chosen diffracted beams are excited will appear bright. The principle of hollow-cone diffraction and imaging is shown in Figure 3.5 [226].

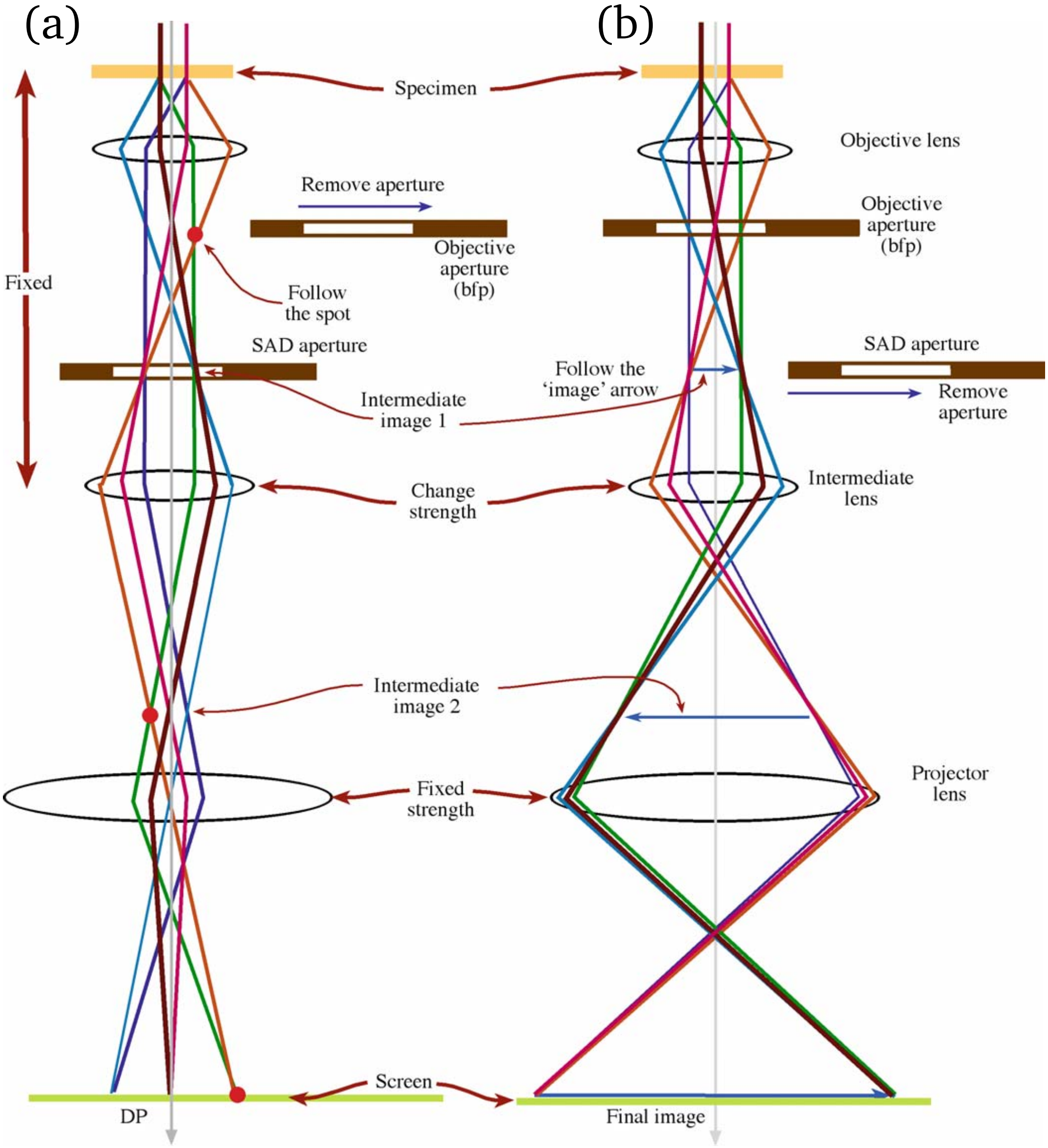
(a)
(b)
Specimen
Objective lens
Remove aperture
Objective aperture (bfp)
Fixed
Follow the spot
SAD aperture
Follow the 'image' arrow
Remove aperture
Intermediate image 1
Change strength
Intermediate lens
Intermediate image 2
Projector lens
Fixed strength
Screen
DP
Final image

Figure 3.4 The two basic operations of the TEM imaging system involve (a) diffraction mode: projecting the DP onto the viewing screen and (b) image mode: projecting the image onto the screen[226].

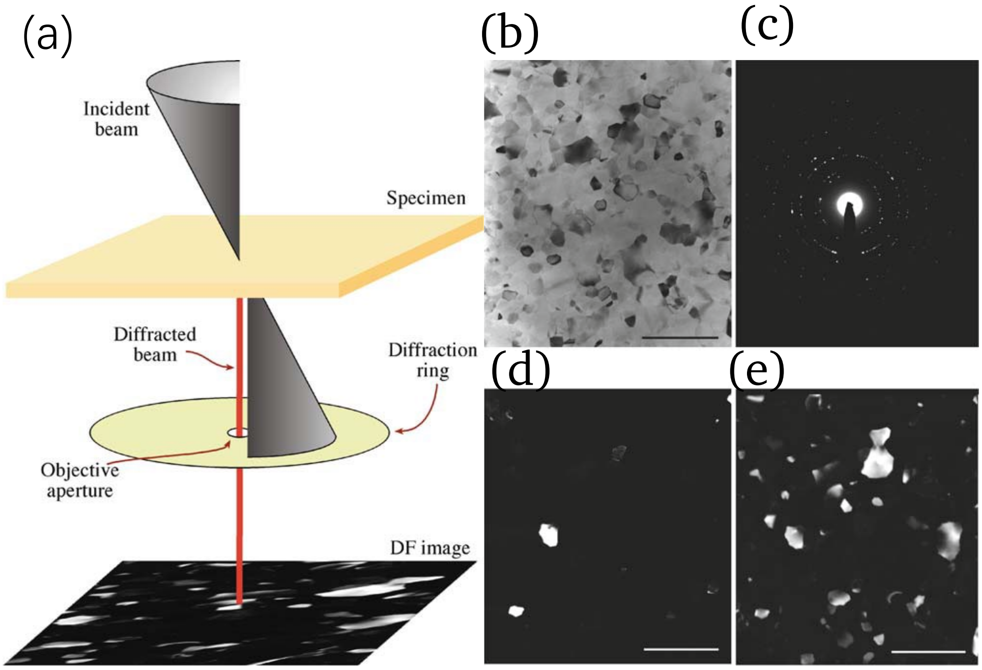

Figure 3.5 (a) Ray diagram showing hollow-cone illumination conditions. The direct beam is always off axis but electrons diffracted at the cone angle are always scattered on axis. (b) A BF image of a nanocrystalline Al film. (c) A hollow-cone SAD pattern from the film. Thus, while a single (220) CDF image (d) reveals only a couple of strongly diffracting crystals, a hollow-cone DF image (e) from all the {220} reflections show diffracted intensity from dozens of grains. The scale bar is 500 nm[226].

HRTEM allows direct imaging of the atomic structure of a sample. It is a powerful tool to study properties of materials on the atomic scale. In HRTEM mode, the incident beam exiting the specimen will interfere with the different diffracted beams to form an interference pattern containing structural information of the specimen. The resolvable details of the image depend on the phase change caused by the incident wave scattered by the sample, the spherical aberration of the objective lens and the selection of additional phase difference caused by the defocus. When a uniform incident beam passes through the specimen, a modulation of the incident wave is caused by the interaction with the potential of the specimen.

To understand the image forming and the analytical method, it is necessary to consider the interaction between sample and accelerated electrons. The electron is a low-mass, negatively charged particle. As such, it can easily be deflected by passing close to other electrons or the positive nucleus of an atom. The interaction can be roughly classified in to two types: elastic scattering and inelastic scattering. The electron interaction with an isolated atom is illustrated in Figure 3.6. In inelastic scattering can occur one of two ways, both of which involve Coulomb forces. As shown in Figure 3.6, the electron may interact with the electron cloud, resulting in a small angular deviation (θ_1). Alternatively, if an electron penetrates the electron cloud and approaches the nucleus, it will be strongly attracted and may be scattered through a larger angle (θ_2). The second principal form of elastic scattering occurs when the electron wave interacts with the specimen as a whole, named diffraction which is particularly important at low-scattering angles. Characteristic X-rays are generated when an energetic beam of electrons interacts with the inner shell electrons by inelastic scattering with enough energy to excite inner shell electrons to outer shell orbitals, leaving inner-shell vacancies. In an isolated atom, the electron is ejected into the vacuum while in a solid it escapes above the Fermi level into the unfilled states. The atom is then left in an excited state because it has more energy than it would like, and we describe it as ionized. Consequently, the ionized atom can return to its lowest energy (ground state) by filling in the hole with an electron from an outer shell[227]. This transition is accompanied by the emission of either an X-ray or an Auger electron, while the signal can be collected by detectors to understand the chemical composition, also known as EDX. Since the total energy is conserved during the interaction, the energy loss of the incident electron is equal to the energy transferred to the bound electron. The energy loss of the inelastic scattered electron is characteristic and can be used to identify the composition, the structure and the atomic bonding of the specimen, called as EELS mentioned above.

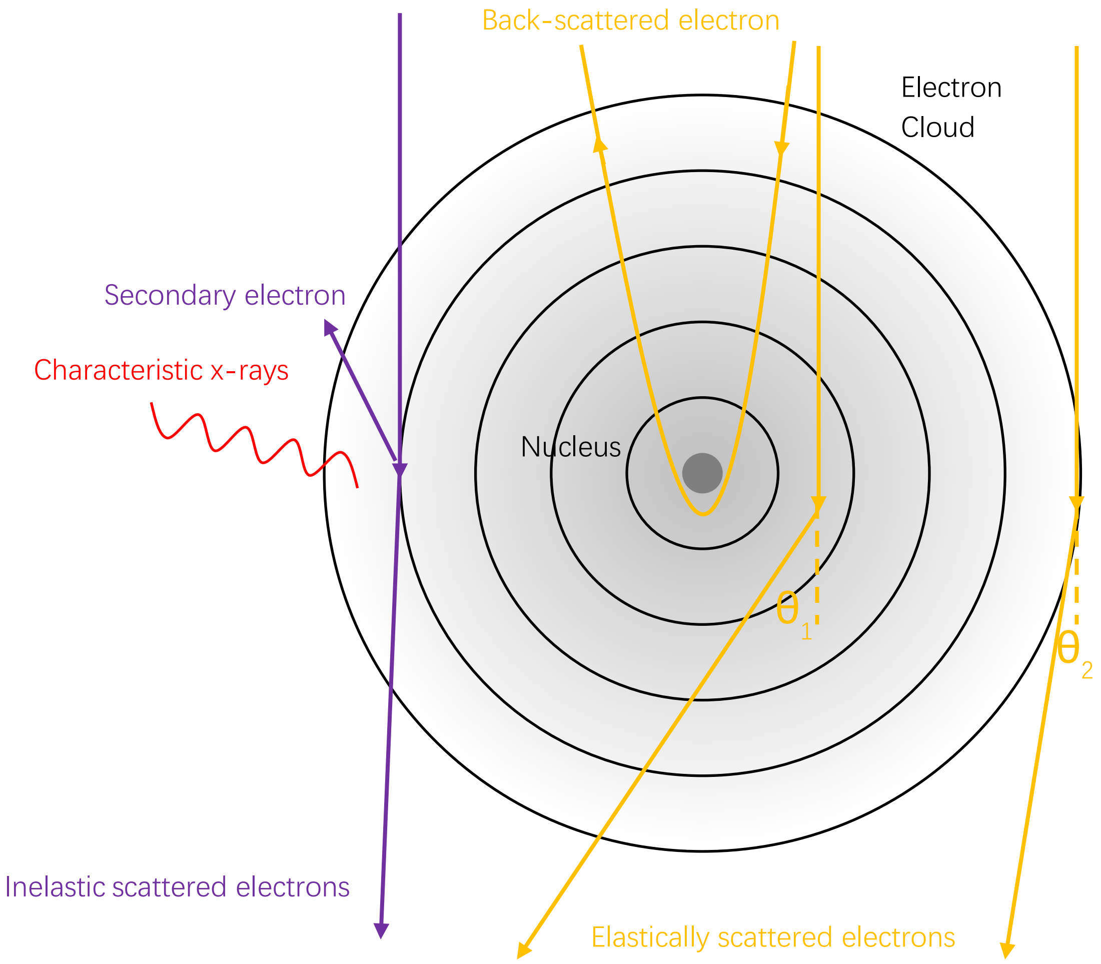

Figure 3.6 Interaction of an isolated atom with electrons including inelastic scattering and elastic scattering.

Additionally, Scanning TEM (STEM) imaging mode becomes more and more popular as it can conveniently operate combining with elemental analysis. In STEM, a convergent beam with a small probe size was used to scan the selected area. The resolution is controlled by the size of the scanning probe, which is determined by the aberrations of the probe forming system and the convergence angle. In contrast to conventional BF/DF-TEM images, bright field and dark field images in STEM are collected by BF detector and annular detectors, respectively. In STEM mode, the annular detector is used to collect signals at even higher scattering angles (>50 mrads). This kind of DF images acquired by high annular detectors are usually known as high angle annular dark field (HAADF) images and Annular dark-field (ADF) imaging. During the electron-matter interaction, high atomic number (Z) elements scatter the incident electrons to large angles much easier. Therefore, high Z atoms indicate a stronger contrast comparing with low Z atoms. For instance, Figure 3.7 indicates a θ phase, Al_2Cu precipitate, in the (011) plane of Al matrix. Cu atoms in the precipitate demonstrate a stronger contrast in comparison with Al atoms surrounding. In addition to imaging, STEM is also commonly combined with analytical techniques such as EDS and EELS to provide the corresponding information on the specimen.

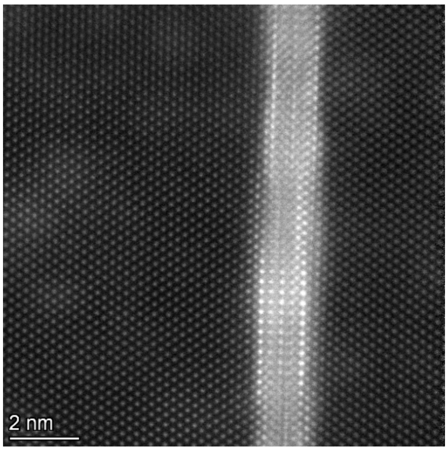

Figure 3.7 HR-STEM HAADF image of Al2Cu precipitate in Al matrix.

In this thesis, a Themis Z, a Themis 300 and a Tecnai F20 ST were used for TEM characterizations. The Themis Z was operated at 300 kV with double aberration corrected (TEM and STEM), Super-X EDX detector, monochromator and Gatan continuum 970 HighRes + K3 IS camera. The Themis 300 was also used at 300 kV with a probe aberration corrector, Super-X EDX detector and NanoMegas ASTAR system. The Tecnai F20 ST was performed at 200 kV equipped with NanoMegas ASTAR system. The experimental data analysis was evaluated with Digital Micrograph, Velox software and Multi-Indexing ASTAR software.

The samples for TEM should be with extremely less thickness, especially for nanocrystalline alloys. FIB is the rather convenient method to prepare the thin lamellae. The procedures of the sample preparation are as follows, shown in Figure 3.8. First, an area of interests is selected in SEM view and Pt is deposited on the surface as a protective layer with ion beam or electron beam, depending on the sample properties. Then two trenches are dug using strong ion beam and high acceleration voltage (30 kV) on both sides of the Pt marked position. Later, a relatively thick lamella is cut off and lift out by Omniprobe and mounted to a finger of a TEM grid. Further milling will be conducted on both sides of the lamella to reduce the thickness until it is thin enough. Consequently, low acceleration voltage (5 kV) is applied for final cleaning to minimize the damage induced by Ga ion.

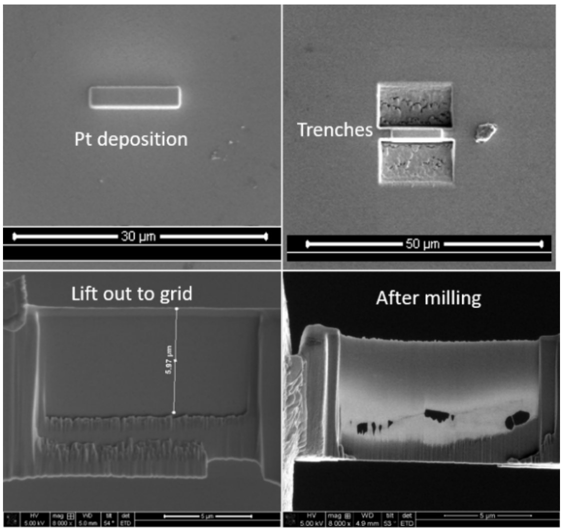

Figure 3.8 A TEM sample preparation procedure: from Pt deposition to lift out and finial thin lamella.

3.2.5 Atom Probe Tomography

Atom Probe Tomography is a relatively new technique that has reached a recognized position among the most important analytical microscopy techniques since the 1990s. Erwin Müller as a student was hired by Gustav Hertz at Berlin Technische Hochschule to build a field electron emission microscope (FEEM) at late of the 1920s. Simultaneously, it is good to know that Max Knoll and Ernst Ruska were working on the invention of the electron microscope at the same institute at the same time. Müller developed the FEEM around 1935 [228] creating a field electron emission source and projecting the emission pattern of electrons onto a fluorescent screen. Later in 1955, Kanwar Bahadur and Müller developed field ion microscope (FIM) that individual atoms became visible [229]. John Panitz developed imaging atom probe in 1972 which can record the hit positions of a single atom type at a time from any given voltage pulse by time gating the channel plates [230]. A 3D data by manually examining a series of 2D maps of a single preselected species as a function of depth can be created. Since 1970s, the atom probe from a one-dimensional technique has been excellently transformed into the tomography technique by Groupe de Physique des Materiaux (GPM) in Rouen. An outstanding breakthrough occurred in 1988 with the design of the first position-sensitive detector for atom probe (POSAP) by the Oxford group[231]. Later, new detectors have also been developed, and modern atom probes are now all equipped with so-called delay-line detectors that are able to combine excellent multihit capability and good time separation limit.

Nowadays, the Local Electrode Atom Probe (LEAP) is the most widely used commercial APT device.

To understand how an APT works, it is better to start with FIM, which is one of the early steps leading to the development of APT. The samples need to be sharp enough to generate the required high electric field. Due to the electric field, ionized rare gas atoms near the surface of a sharp tip are the vector for the formation of an image of the atomic positions at the specimen surface. The intrinsic resolution of the field ion microscope is thus theoretically given by the wavelength associated to the emitted gas ions. Based on a single metal sphere mode, the voltage V at the specimen surface can be given by [232],

$$V = \frac{1}{4\pi\varepsilon_0}\frac{Q}{R} \tag{3.1}$$

and electric field F is as follows,

$$F = \frac{1}{4\pi\varepsilon_0}\frac{Q}{R^2} = \frac{V}{R} \tag{3.2}$$

where R is the radius, Q is the charge distributed at the surface. Considering that electric fields required for both field ionization and field evaporation, are in the range of 10^{10} V/m, and that voltages in the kilovolts range are easily achievable, it appears that radii as small as a few tens of nanometers are required. However, as the sample is a needle instead of a sphere, a correction factor k_F in the electric field is added,

$$F = \frac{V}{k_F R} \tag{3.3}$$

where k_F is typically in a range of 2-10. An illustration of FIM is presented in Figure 3.9. As shown in the figure, an image of the sample surface can be obtained on a detector after gas atoms are ionized and repelled and FIM image is close to the stereographic projection of the sample surface.

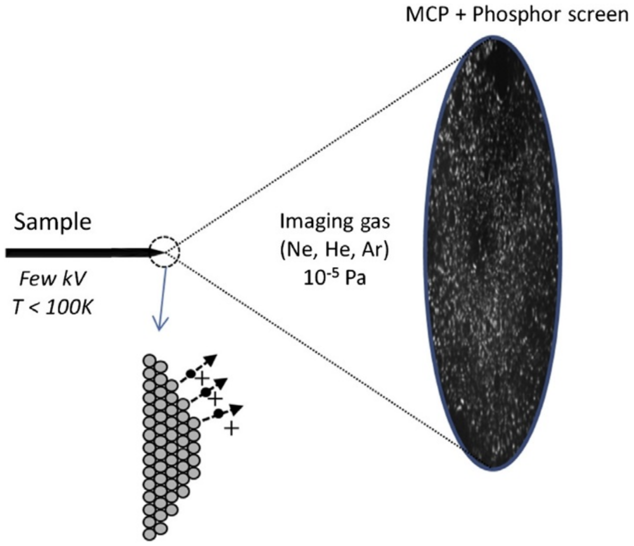

Figure 3.9 Schematic representation of the field ion microscope [233].

For APT, field evaporation a high electric field at the surface of a material induces desorption and ionization of atoms even at cryogenic temperatures and consequently, the removal of specimen atoms. The necessary field is created by applying a modest voltage (5–10 kV) to a very sharp specimen resulting positive ions accelerating away toward the counter electrode. Then a position-sensitive detector records the hit position of individual ions, the accumulation of which forms an image of the tip surface and ultimately enables a direct mapping of the atom's position on the original curved surface of the specimen apex. In LEAP, a local-electrode geometry [234,235] allowed to go from a 15 nm field of view to greater than 150 nm. Furthermore, voltage pulses have been used to generate pulsed field evaporation meaning that the sample is required for high conductivity. Alternatively, short laser pulses directed at the specimen apex can be used to induce an evaporation pulse for any material regardless of electrical conductivity. Base on this, a laser pulses assisted field evaporation can be used to reduce the risk of rupture of fragile materials [236]. In addition, APT has the advantage that all species of atoms are detected with uniformly high efficiency by a position-sensitive detection system placed in front of the specimen. This detector must have high timing measurement abilities. The chemical nature of each detected atom is defined by time-of-flight mass spectrometry and the original 3D position of each atom inside the material is calculated from the position information measured by the detection system and the geometrical properties of APT [237]. Figure 3.10 illustrates the principle of APT.

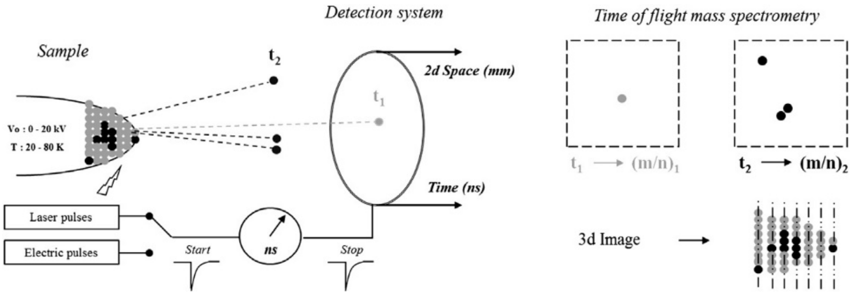

Figure 3.10 Principle of the ATP technique. Atoms at the surface of the specimen are evaporated by field effect and fly towards a detection system [237].

In this dissertation, the APT analysis was used with a LEAP 4000X HR instrument, shown in Figure 3.11. Detailed parameters for the measurements are described in respective chapters. The APT reconstruction and data evaluation were performed with IVAS 3.6.14 and AP Suite software.

Figure 3.11 Photograph of a LEAP 4000X HR system.

As mentioned above, the shape of the samples for APT is a needle-like with a tip radius of a few tens of nanometers. Electrolytic polishing is a fast and efficient method but is not applicable for all materials. Hence, FIB was utilized for the APT sample preparations. The tip preparation procedure of an APT/TEM correlative experiment on C2N3 alloy was shown in Figure 3.12 as an example. In the beginning, similar to TEM lamellae steps, an interesting place should be found, and a thick lamella is cut off. Later, the lamella is transferred with the help of Omniprobe to a special TEM grid on with the finger-like tips. This kind of grid can be homemade out of regular TEM grids using electrolytic polishing. Once the lamella touched the finger, Pt is deposited between the finger and the bottom of the sample, then the rest of the lamella is cut off. Then one just needs to mill the sample to a needle shape until a diameter is less than 50 nm on top. Finally, a low kV milling is performed to reduce the damage layer induced by Ga ions.

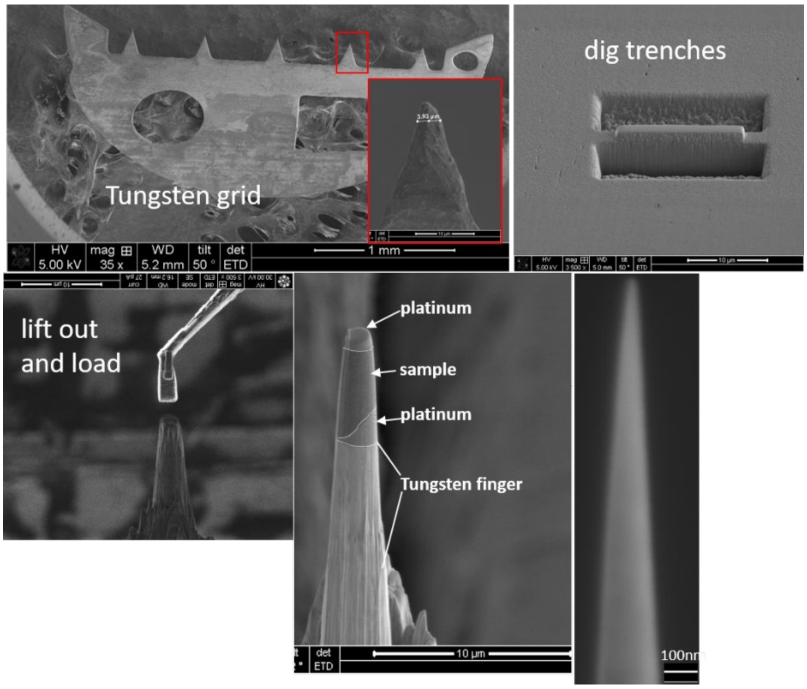
Tungsten grid
HV 5.00 kV
mag 35 x
WD 5.2 mm
tilt 50 °
det ETD
1 mm
dig trenches
lift out
and load
platinum
sample
platinum
Tungsten finger
10 µm
100nm

Figure 3.12 Step by step procedures of APT tips preparation onto the TEM grid.

3.3 Mechanical test

3.3.1 Microhardness

Microhardness measurement is an important tool to fast examine the material mechanical properties [238]. The simplest way of determining the resistance of a metal to plastic deformation is through a hardness test. The Vickers hardness (HV) is computed from the equation (3.4) and is equal to the load divided by the area of the depression,

$$HV \approx \frac{1.891F}{d^2} \tag{3.4}$$

where F is the applied force in kgf, d is the average length of the diagonal left by the indenter in millimeters. Before to measure the microhardness, the surface of the sample was polished until the roughness of 1μm. All the measurements were conducted with a load of 500 g with a dwell time of 10 s on the polished surface of the samples using Buehler Micromet-5104 device. The distance between indents was maintained at a constant value of 0.5 mm. Four series of measurements along the HPT disc diameters were conducted for each sample after HPT processing. For as-cast samples and annealed samples at least 10 points were measured.

3.3.2 Tensile test

Uniaxial tensile testing is a fundamental materials science and engineering test in which a sample is subjected to a controlled tension until failure. The characteristics such as, Young's modulus, Poisson's ratio, yield (ultimate) strength, strain hardening and uniform (ultimate) elongation, can be determined.

The dog-bone specimens for tensile tests were cut out from the HPT disks with a gauge length of 3 mm and a square cross-section of ~0.6 mm^2. All the surfaces of the gauge region were polished with a SiC paper (P2400) to remove deep scratches and oxidations. For precise elongation measurements, the specimens were marked with TiO_2 paint using an airbrush, see Figure 3.13. Tensile tests were performed at RT at a strain rate of 10^{-3} s^{-1} using a custom-built computer controlled micro-tensile stage equipped with a high-precision laser extensometer P-50 by Fiedler Optoelectronics. At least two samples for each state were pulled to fracture to obtain statistically reliable results.

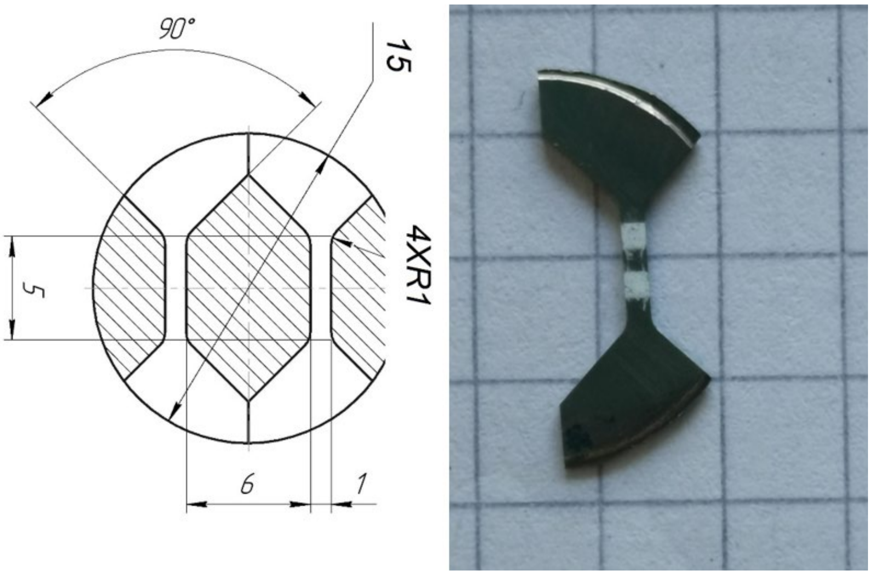

Figure 3.13 Schematic representation showing cutting position of tensile specimens in HPT-disks and specimens before test.

4 Influence of carbon alloying on the microstructure evolution of CoCrFeMnNi HEA processed by high pressure torsion at room and cryogenic temperatures

4.1 Materials and experimental methods

For the synthesis of non-equiatomic $Co_1Cr_{0.25}Fe_1Mn_1Ni_1$ (subscripts indicate the molar fraction of the respective component) alloys with the reduced Cr content, high purity elements (99.9 wt. %) were melted by vacuum induction with the addition of different amounts of C. The nominal concentration of C in the alloys was 0, 0.5 and 2 at. %. The chemical compositions of the as-melted alloys measured by EDX for metallic elements and hot gas carrier method for C content. The corresponding results are shown in Table 3.1 in Chapter 3. Cylinders with the diameter of 15 mm were machined from the produced ingots. For the HPT processing, disks with the diameter of 15 mm and initial thickness of 0.7 mm were sectioned out. HPT was performed at RT under a hydrostatic pressure of 6.5 GPa for 0.5, 1 and 3 turns with the rotation speed of 0.5 rpm at RT and an extra 3 turns sample at LNT for C2 alloy. Therefore, the specimens under the study were identified as CxNy, where x means the nominal C content for each alloy and y denotes the number of revolutions during HPT. The von Mises equivalent strain (ε) is calculated as:

$$\varepsilon = \frac{2\pi N r}{\sqrt{3}h} \tag{4.1}$$

Where r is the radius of the considered position, N is the number of revolutions and h represents the thickness of the disk [239,240]. Zeiss LEO 1530 scanning electron microscope and Zeiss Auriga 60 with BSE and EDX detectors were used for microstructure characterization and elemental analysis for both HPT and as-cast specimens. Specimens for XRD analysis were prepared by mechanical polishing and final electro-polishing to remove the damaged surface layer. XRD measurements were performed using a Philips X'Pert powder diffractometer with a Cu-Kα anode. The strain and crystallite size were evaluated using a CMWP [218] and the lattice parameters were evaluated by a X'Pert High Score software using a Rietveld analysis. Transmission electron microscopy (TEM, STEM) and Automated Crystal Orientation Mapping (ACOM) were carried out using FEI Tecnai F20-ST at 200 kV and Thermo Fisher Themis-Z at 300 kV. ACOM data was collected by ASTAR system using a pixel size of 1 nm. Crystallites with an area under 20 pixels (corresponding to an equivalent diameter ~5 nm) were not included into the statistics due to their overlapping along the electron beam path. TEM lamellae and the tips for APT analysis were prepared on FEI Strata 400 and Zeiss Auriga 60 using Ga FIB. APT measurements were conducted using Cameca-LEAP 4000X HR instrument in laser probe mode and voltage mode at 55K, with a pulse energy of 30 pJ, a pulse rate of 200 kHz and a target detection rate of 0.3%. The reconstruction of APT data was performed with IVAS 3.6.14 and AP Suite software.

4.2 Results

4.2.1 Microstructures of C-alloyed HEAs before HPT

Typical BSE images of the as-cast microstructures of the alloys with different C contents are shown in Figure 4.1 (a-c). All samples are coarse grained; grains are typically several hundred microns in diameter. Fine inclusions (visible as dark spots in Figure 4.1) noticed in all the alloys are oxides and sulfides reported previously in this alloy system [173,198]. Meanwhile, Figure 4.1 likewise reveals that the alloys solidify with primary FCC dendrites and interdendritic segregation, which is prevalent in as-cast CoCrFeMnNi HEAs [7]. In the alloy with 2 at. % C, narrow lamellar precipitates along GBs are observed under a higher magnification (Figure 4.1 (d)). These precipitates in the earlier research [12] were identified as M_7C_3 type carbides.

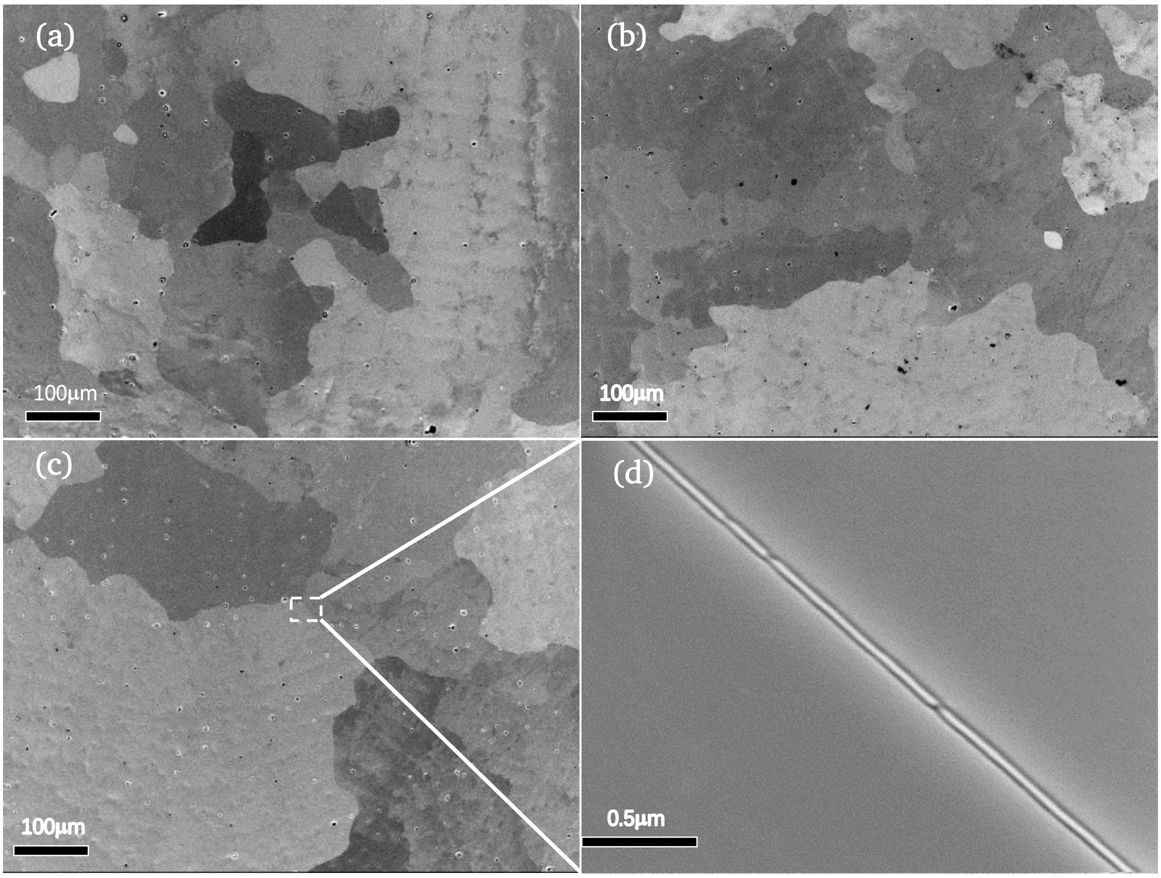

Figure 4.1 (a-c) BES images of the microstructure of the as-cast CoCrFeMnNiCx HEAs: (a) x= 0; (b) x=0.5; (c) x=2; (d) corresponding enlarged region in (c).

In order to reveal the composition of the carbides and their morphology, Figure 4.2 shows a 3-dimensional reconstruction of the carbide on a grain boundary in the as-cast C2 alloy. The carbide enriched with C and Cr is seen in Figure 4.2 (a). Ni and Co are partitioned mainly in the FCC phase, while Mn and Fe are distributed more evenly between the FCC phase and the carbide particles. An interface view of the carbide and the matrix highlighted by iso-surfaces with the respective thresholds of 34 at. % Cr, 28 at. % Ni and 38 at. % Mn are shown in Figure 4.2 (b); the corresponding 1-dimensional composition profile across the carbide in Figure 4.2 (c), computed along the red arrow, is shown in Figure 4.2 (b). The carbide has a lamellar shape with a thickness of ~25 nm and crosses the whole reconstruction volume. Further, the C concentration measured within the carbide in Figure 4.2 (c) is ~17 at. %, which does not fit the anticipated concentration in neither the M_7C_3 nor $M_{23}C_6$ type carbide. Thus, the chemical composition of the carbide is likely far from equilibrium. An increase of the Cr and C concentration from the interface towards the matrix suggests that the formation of the carbide leads to Cr and C depletion at the grain boundary, which indicates that such carbides precipitate after complete solidification of the alloy. The formation of $M_{23}C_6$ and M_7C_3 carbides with similar morphology has been frequently observed in some austenitic steels after ageing (see, for example [241–246]). It was established that the precipitates discontinuously form at high angle grain boundaries, and like all boundary precipitates have a parallel orientation with one of the grains. These precipitates grow further with preferential migration of incoherent $M_{23}C_6$/FCC matrix boundary and gradually became aggregated to form film-like precipitates. The thermodynamic aspects and mechanism of such carbides formation in Fe-Cr-Ni steels are discussed in Refs. [242,246–249].

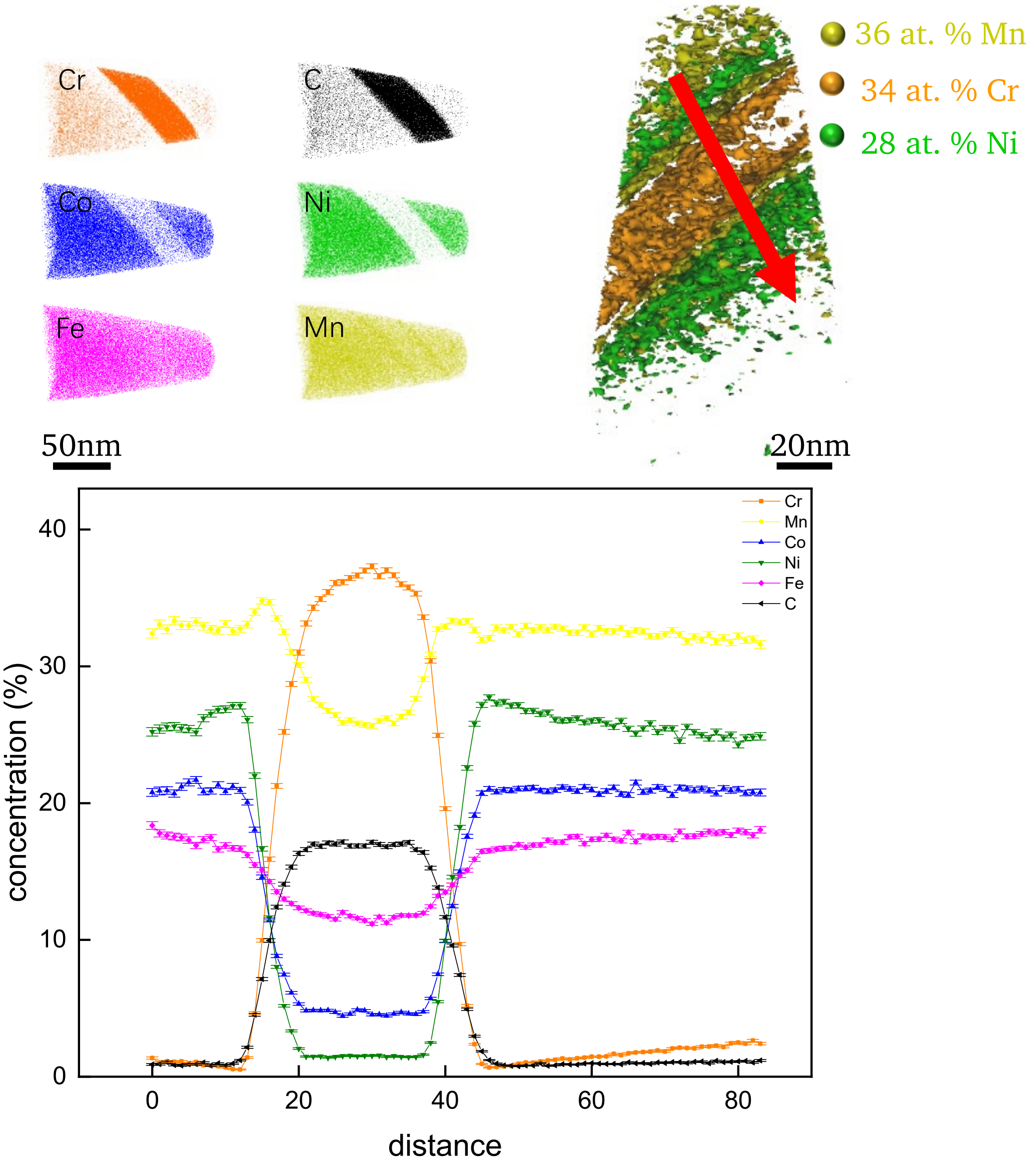

Figure 4.2 APT reconstruction of the carbide at a grain boundary in the as-cast C2 sample shown in Figure.4.1(d): (a) overview of the reconstruction with Cr, Co, Fe, Ni, Mn and C maps (b) iso-concentration surfaces show areas with element concentration exceeding 36 at. %.

4.2.2 Microstructures evolution of C-HEAs during HPT at RT

It has been reported that HPT leads to the formation of a gradient microstructure varying along the radius, which is conditioned by the gradient distribution of shear strain [174,250]. Figure 4.3 shows the microstructure evolution in the C0N0.5 alloy from the HPT sample center towards its periphery. In the central areas, the initial (as-casted state) dendritic structure with the inhomogeneous distribution of constituting elements is persisting (Figure 4.3 (a), (d)). At the radius of 0.25 mm, which corresponds to a relatively small equivalent strain of ~0.6, massive twinning (or rather nano-twining) occurs as shown in Figure 4.3 (b). Figure 4.3 (c) suggests that a nano-structure formed apparently at the distance of 7 mm (equivalent strain of ~4). The sample surface shows almost uniform BSE contrast, nevertheless the elemental distributions in the matrix exhibit striped bands along the shear direction (Figure 4.3 (f)). The regions depleted with Mn and Ni are enriched in Fe, Cr and Co, and vice versa.

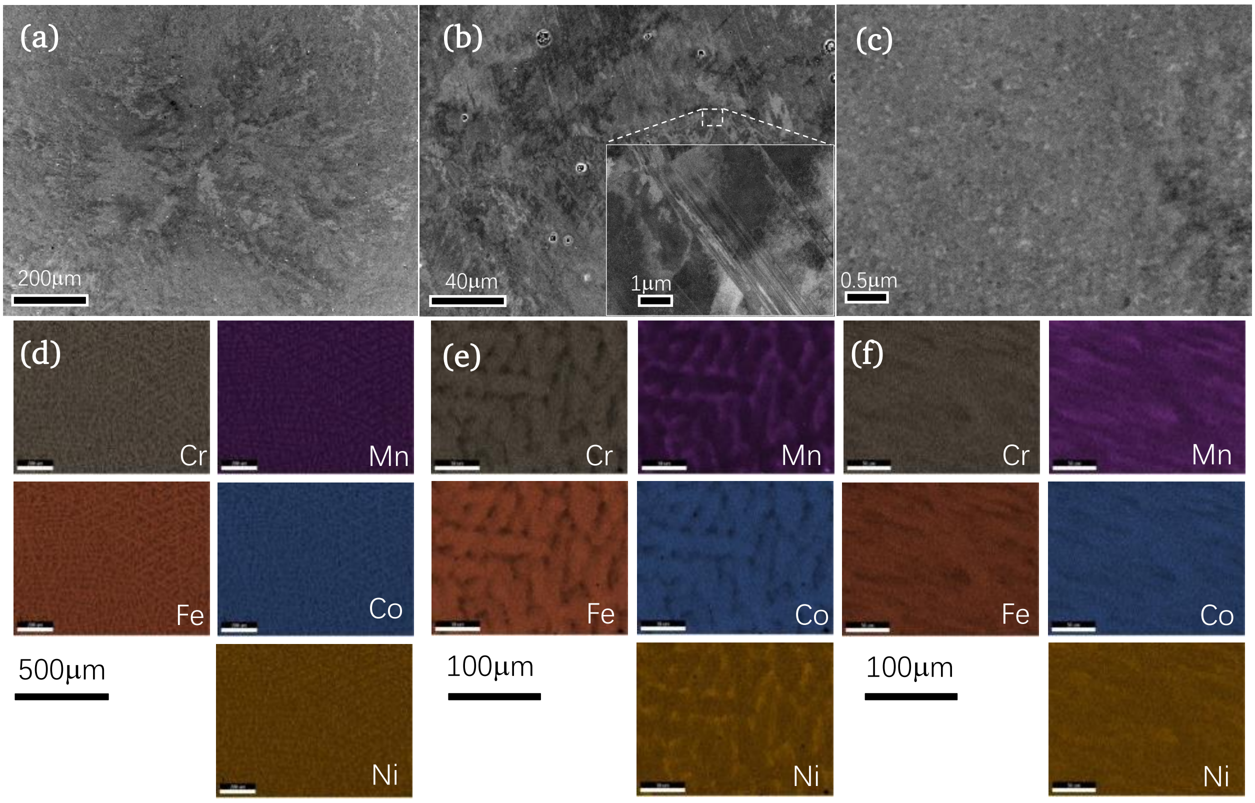

Figure 4.3 Microstructure evolution of the C0 alloy during HPT: (a) center position without shear strain; (b) deformation structure with twinning, the equivalent strain ~0.6; (c) the microstructure at the edge of HPT disk, the equivalent strain ~4; (d-f) the EDX elemental maps corresponding to areas shown in (a-c).

The compositional fluctuations of C2N3 sample after HPT were examined in Figure 4.4. As can be seen in Figure 4.4 (a), the elemental distribution map acquired from the FIB sample indicated a band-shape of the projection of the deformed dendrite and interdendrite structures after HPT leading to the chemical fluctuations of the multiple elements in the as-casted alloy (see Chapter 2). The dendritic band (DB) is rich in Cr, Co and Fe which is analogous to dendrite in as as-casted alloy in Figure 4.3, whereas interdendritic band (IDB) is rich in Ni and Mn. Figure 4.4 (b) indicated a uniform nanocrystalline single FCC phase microstructure with elongated grains in the saturation region. Though the deformed alloy exhibited a compositional inhomogeneity, the grains were refined to similar sizes in both DB and IDB, ~20 nm in width. A concentration profile was created along the white arrow indicated in Figure 4.4 (a) to determine the composition of each band. As illustrated by Figure 4.4. (a) and (c), the border between DB and IDB appears blurry which is mainly due to the effect of sample thickness and plastic deformation induced during HPT. In addition, a statistical comparison based on SEM-EDX images and TEM-EDX maps indicated that DB has a volume fraction of ~2/3 and higher concentration of Fe, Co, and Cr while IDB has a low volume fraction of ~1/3 and higher concentration of Mn and Ni. The atomic concentrations of each element are presented in Table 4.1.

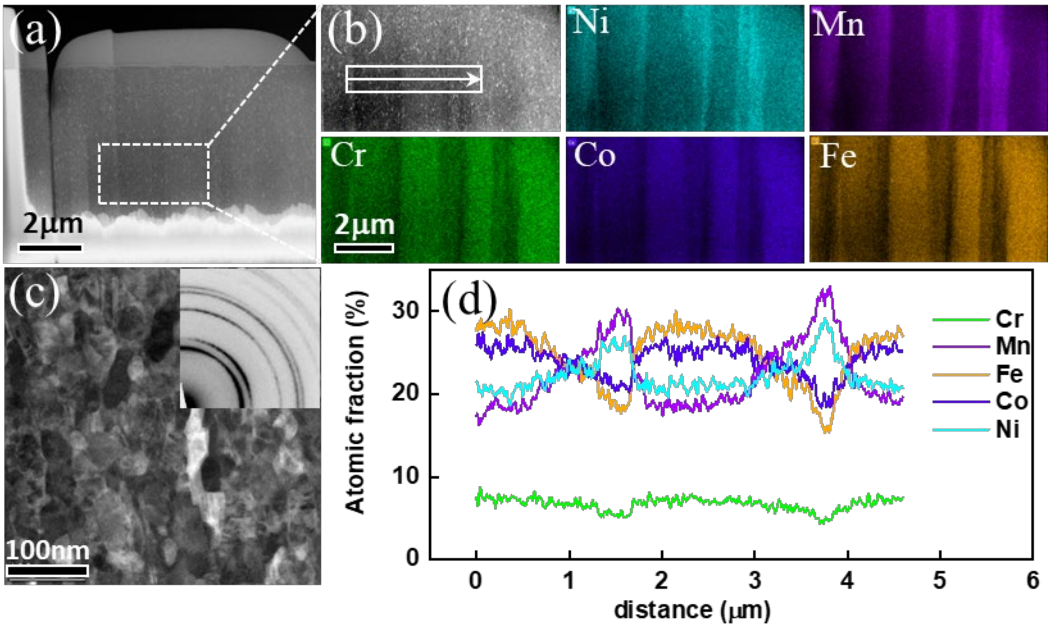

Figure 4.4 Microstructures and distribution of chemical elements of C2N3 alloy. (a) EDX maps of metallic elements and the selected area in original TEM lamella; (b) HAADF-STEM image of the microstructure of the C2N3 alloy and inserted SAED; (c) a concentration profile created along the white arrow in (a).

Table 4.1 The composition and volume fraction of DB and IDB regions

Domains	Volume fraction	Chemical composition (%)				
		Cr	Co	Fe	Ni	Mn
DB	2/3	6.9±0.6	24.9±2.8	28.0±3.0	20.0±2.6	17.9±2.5
IDB	1/3	4.5±0.4	19.4±2.4	16.7±2.2	26.2±3.2	30.4±3.7

Figure 4.5 (a-c) show the DF-TEM images and corresponding SAED patterns of the high entropy alloys, after three turns of HPT. All observations were performed in a cross section at the periphery of HPT disks. The microstructure of all the alloys is characterized by elongated in shear direction grains. Apparently, the grain size decreases with the C increasing content. Nano-twins and dislocations are clearly observed in the BF-TEM images for C0.5N3 and C2N3 alloys shown in Figure 4.5 (d-e), respectively, however, the relative amount of twins is not very high. In fact, less than 10% of grains contain twins. The ring arrangement of the diffraction spots suggests that the nano-structure contains boundaries of high-angle misorientation. The average grain sizes are 45, 29, and 18 nm in C0N3, C0.5N3, and C2N3 alloys, respectively, as determined using the linear intercept method on HAADF images. It is worth noting that all grain boundaries were taken into account, including twin boundaries, and therefore the estimated grain size includes the twins as well. However, we should keep in mind that the calculated grain size is the minimum dimension of the crystal, which has an ellipsoid shape after HPT processing [251].

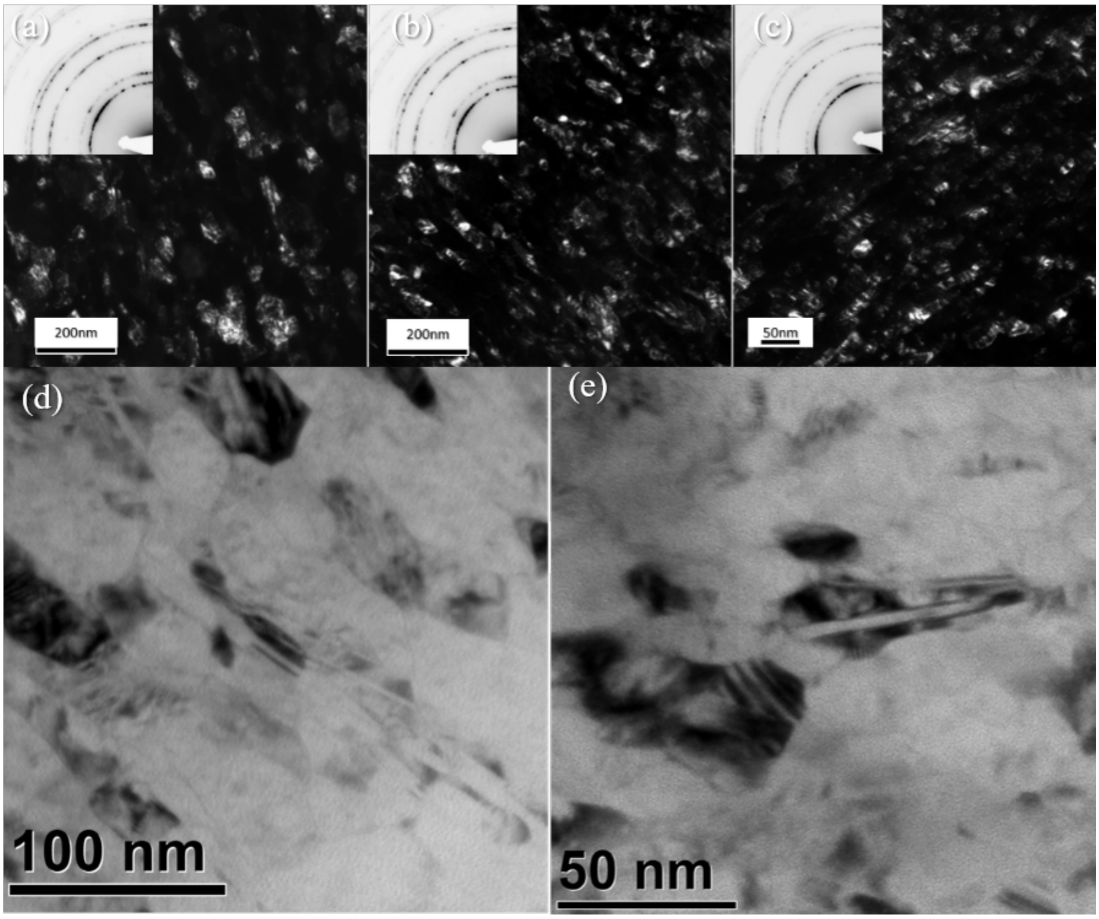

Figure 4.5 DF-TEM images and corresponding SAED patterns (inserts) of HEAs processed by HPT with 3 turns: (a) C0N3; (b) C0.5N3; (c) C2N3; (d, e) higher magnification BF-TEM images for C0.5N3 and C2N3 alloys, respectively.

Figure 4.6 shows the XRD patterns of HEAs with different C contents after three turns of HPT. The measurements were done at the periphery of the HPT discs with a strain γ approximate ~220. CMWP fitting results [218] were presented for the determination of crystallite size distribution and the dislocation structure of alloys the obtained sub-grain size, dislocation density summarized in Table 4.1. Only FCC phase peaks are present in the pattern suggesting that the FCC phase is stable during the HPT processing. This observation is consistent with the TEM SAED patterns (inserts in Figure 4.5). It is apparent that the peaks of the C2N3 alloy are broader than these of C0N3 and C0.5N3 alloys, due to the smaller grain sizes and high dislocation density, as shown in Table 4.2. Meanwhile, the maximums of the C2N3 alloy shift towards lower diffraction angles as is evident from an enlarged 2θ angle peaks image showed in the right-hand side of Figure 4.6. This shifting suggests that C dissolves mostly in the FCC matrix and induces an increase of the lattice parameter shown in Table 4.2. The lattice parameters of C0N3 and C0.5N3 are almost the same implying that the distortion caused by C atoms in the C0.5N3 alloy is quite small. Note that the diffraction peaks of carbides are not detected, probably due to a small volume fraction and nano-size of the carbides after HPT.

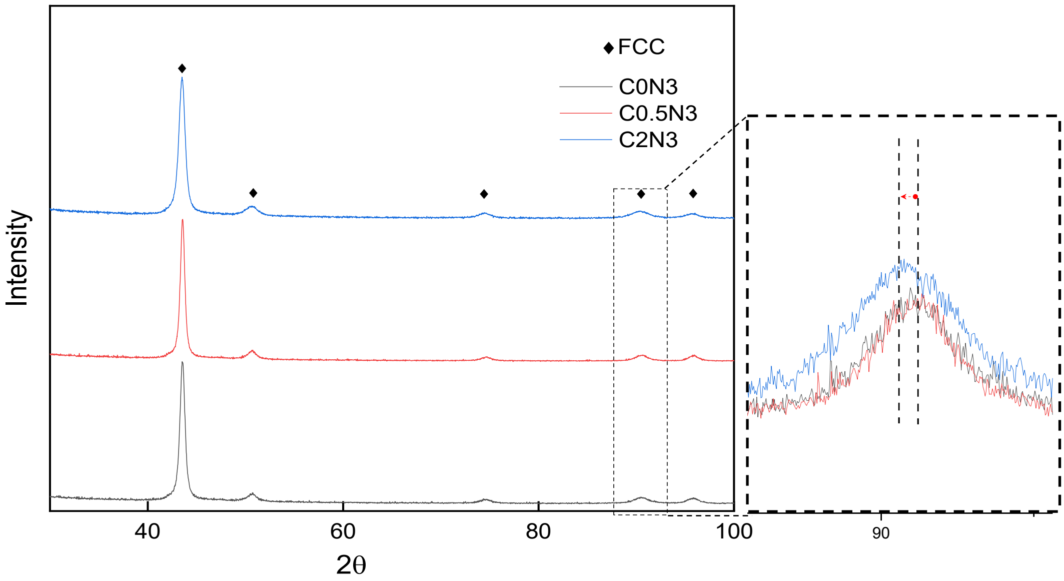

Figure 4.6 XRD diffraction patterns for the high entropy alloys with different C contents after three turns of HPT. The insert shows enlarged (311) peaks.

Table 4.2 The grain/crystallite sizes determined by STEM/CMWP method, the dislocation density ρ, the lattice parameter a.

Alloys	$<X>$area (nm)	d by STEM (nm)	ρ (10^{16} m^{-2})	a (Å)
C0N3	22.4	45	0.57	3.5949(±0.00048)
C0.5N3	17.7	29	1.85	3.5955(±0.00034)
C2N3	16.5	18	8.26	3.6054(±0.00064)

Later, the results of crystallite size and dislocation density were analyzed for CxN3 samples with CMWP method were demonstrated in Figure 4.7. The measured points were selected along the HPT disk radius at the position of 1, 2, 5 and 7.5 mm. The crystallite sizes of all the CxN3 indicated a decreasing trend with the shear strain increasing, shown in Figure 4.7 (a). C2N3 alloy presented a saturation of the crystallite size at $r = 2$ mm with a shear strain of ~55, which indicate a large saturation region. However, the final saturation crystallite sizes are approximate for these three alloys, and are in the range from 16~22 nm. On the other hand, it can be seen that the dislocation density of C2N3 dramatically increased to the maximum at a shear strain of ~55, which is analogous to the crystallite size results. Furthermore, in C2N0 and C2N0.5 alloys, the dislocation densities illustrated a decrease tendency with the strain increasing. This may relate to the common dislocation density evolution: the dislocation density increased significantly at the lower strain states and then decreased which can be explained based on the facts that dynamic recovery occurred extensively when the dislocation density becomes high [126]. The dislocation generation rate and annihilation rate are supposed to reach a balance at large strain value, resulting in a steady state dislocation density.

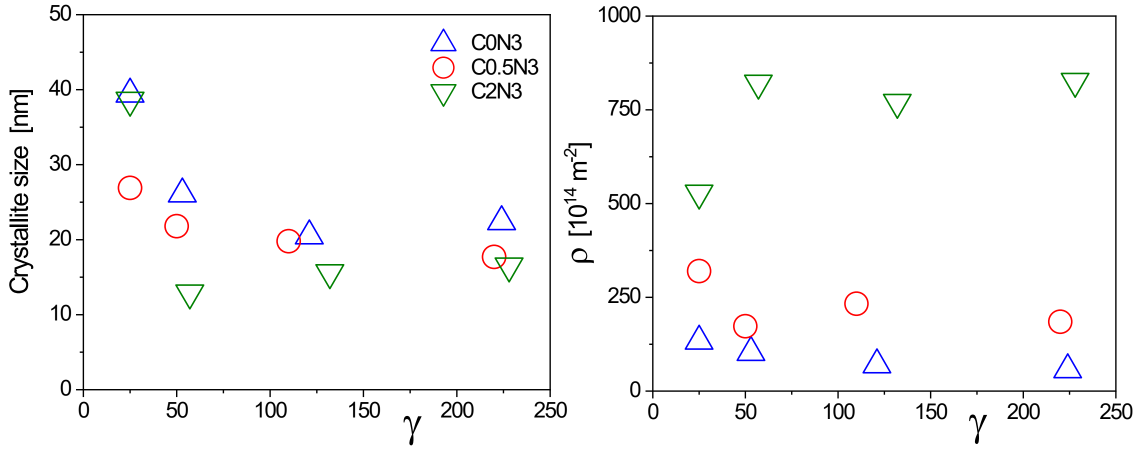

Figure 4.7 The crystallite size vs. shear strain γ; (b) the dislocation density vs. shear strain γ.

Figure 4.8 presents the chemical composition of C2N3 alloy obtained using the APT reconstruction. The reconstruction volume contains a number of grains according to the measurements on TEM images in Figure 4.8 (a-c). The elemental distributions illustrate a single-phase solid solution character of the material with chemical homogeneity at the nano-scale. No obvious segregations or C, Cr-rich precipitates are observed. The carbides are likewise not detected by the APT technique due to two conceivable reasons: (i) the initial brittle carbides fractured into finer pieces during HPT processing and dissolve in the alloy matrix under the high strain [210]; (ii) the fine shattered carbides are not detected due to the limited volume measured. Because of the limited volume of tip of the APT measurements, it is essential to note that the multiple elements in the HPT processed carbon-alloyed HEA are not uniformly distributed as discussed above, though a single FCC structure were revealed by TEM characterizations.

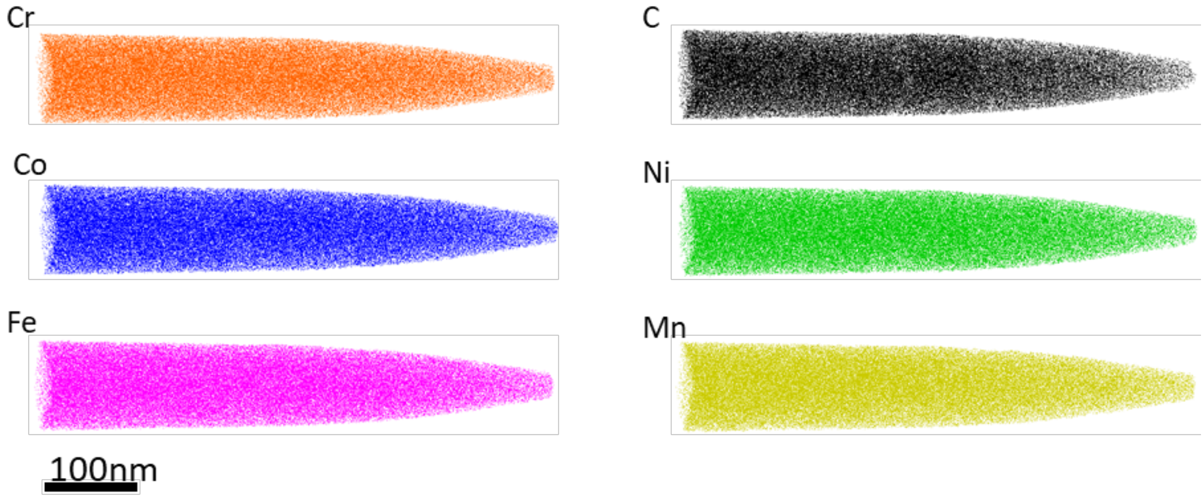

Figure 4.8 APT reconstruction the C2N3 alloy at saturation: an overview of the reconstruction with Cr, Co, Fe, Ni, Mn and C maps.

4.2.3 Comparison of saturation microstructures of C2N3 alloy deformed at room and liquid nitrogen temperature

The comparison of microstructures of the C2N3 RT and C2N3 LNT samples corresponding to the sample region with saturated microhardness are shown in Figure 4.9. The BF-TEM images in Figure 4.9 (a) and (d) illustrate the nano-scaled uniform microstructure. The corresponding diffraction patterns indicate that both samples exhibit single FCC phase and uniform nanoscale grains. No precipitation or phase transformation occurred during and after HPT processing. ACOM maps and inserted grain size distribution histograms are shown for the two HPT conditions in Figure 4.9. (b) and (e). Nanoscale grains are separated by high angle grain boundaries (> 15°) shown with black lines. The average grain size of the two alloys is approximately around ~18 (±12) nm. In addition, several nanotwins can be found in orientation maps in both alloys. However, due to the limitation of scanning resolution, nanotwins with a width less than 4 nm could not be detected especially in LNT alloy. High resolution TEM images of these two samples are shown in Figure 4.9 (c) and (f), respectively. The inserted fast Fourier transform (FFT) images show the [011] zone axis in both samples. Apparently, the amount of deformation twins was relatively low in the RT sample. However, there are plentiful nanotwins with a thickness between 1 and 4 nm as shown in Figure 4.9 (f) marked by yellow dashed lines and the related FFT provides significant evidence of Σ3 boundaries in (011) plane of FCC structure. In facts, nano-twins were observed in all grains with the [011] zone axis normal to the sample surface (i.e., in all grains suitably oriented for observation of twins in HRTEM) in LNT sample.

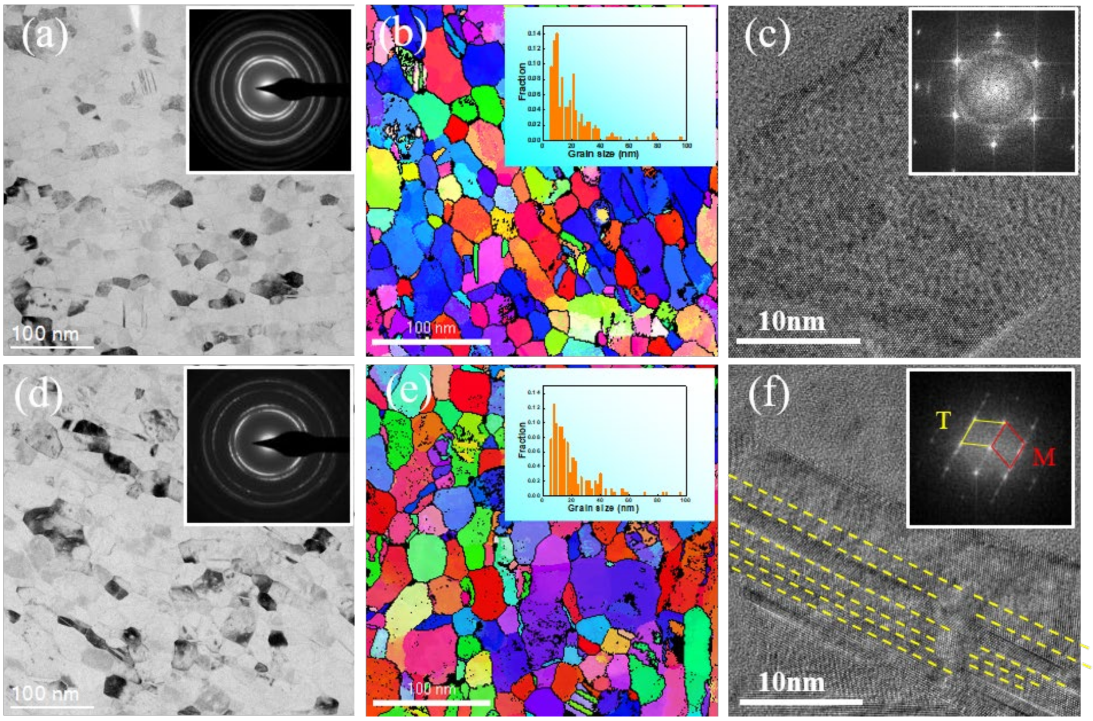

Figure 4.9 TEM characterization of CoCrFeMnNiC2 deformed at room (a-c) and cryogenic temperature (d-f). (a) and (d) show the BF-TEM image with inserted selected area diffraction patterns;(b) and (e) are orientation maps evaluated from

ACOM and corresponding grain size histogram; (c) and (f) show the HR-TEM image with enlarged area and corresponding FFT.

The chemical composition and the elemental distribution in studied alloy were analyzed using APT method, as shown in Figure 4.10. As the grain sizes of both alloys are around ~18 nm, the cuboids of 20 nm thickness were sliced from the original APT volumes to avoid crystal overlapping. The carbon distribution map in Figure 4.10 (a) shows that the carbon atoms are not homogeneously distributed in this sample but have segregated along the surfaces, which are most probably grain boundaries (indicated by arrows). Let us emphasize that the APT sample (a needle with base radius of 50 nm and a length of 150 nm) contains approximately ~100 grains with several hundreds of grain boundaries. Therefore, the obtained results are statistically valid. Meanwhile the metallic constituents were distributed homogeneously. The segregation of the C-atoms fluctuates on a nanometer-scale in the range roughly from 5 to 30 nm corresponding to the range of grain sizes in the RT alloy (Figure 4.9 (b) and (e)). Therefore, it seems that carbon atoms segregate to crystalline defects like GBs, which more likely present with a high density in severe deformed alloys. However, this significant segregation phenomenon was not observed in the LNT sample shown in Figure 4.10 (b) C-map. The difference between the segregation behavior at RT and at LNT indicates that the C atom diffusion during the deformation process is insufficient at the low temperature.

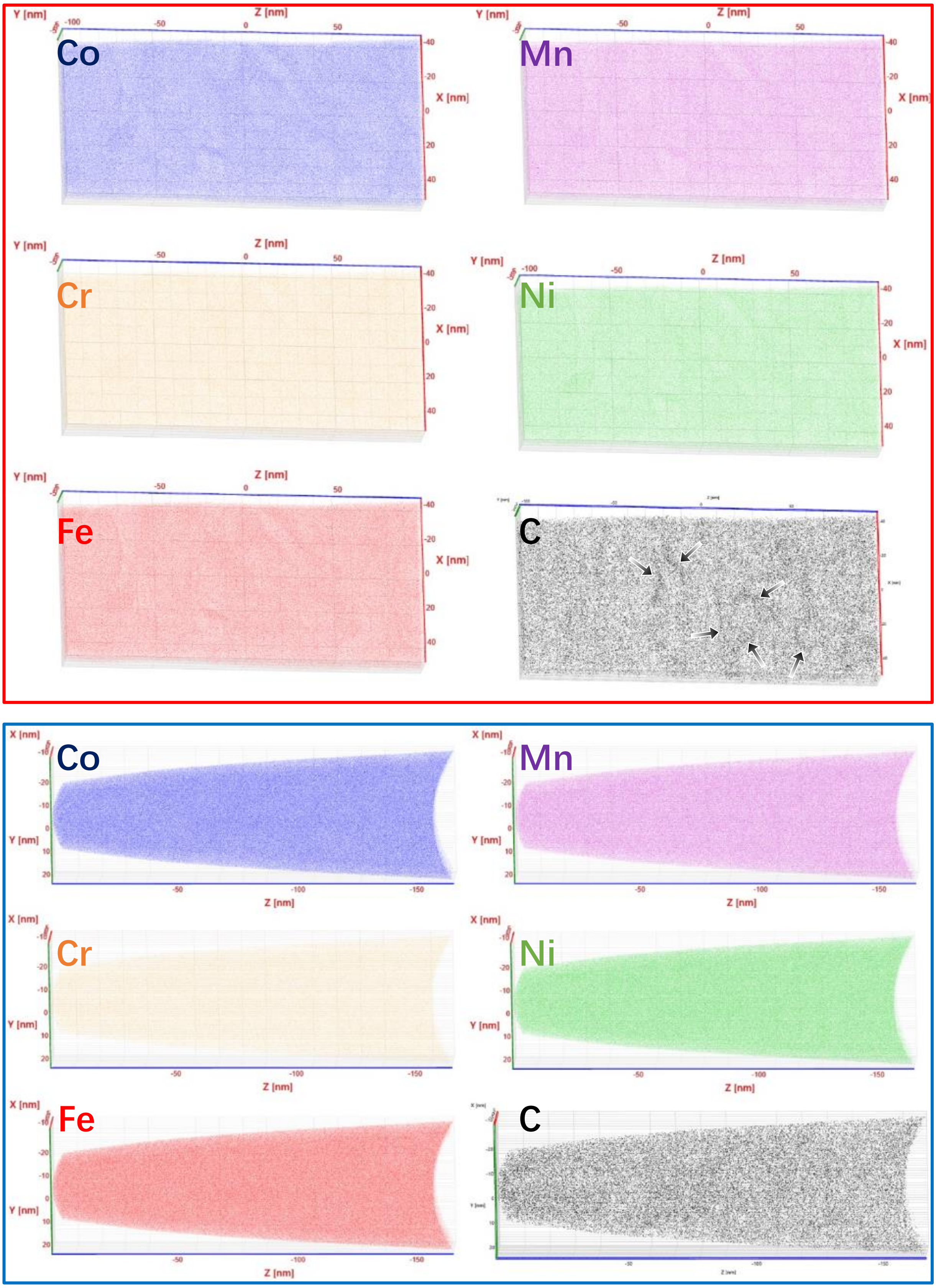

Figure 4.10 APT reconstructions in (a) RT and (b) LNT alloys. Co, Mn, Cr, Ni, Fe, and C elemental distribution were shown separately; the arrows C map (a) indicated the sites of carbon segregation.

4.3 Discussion

4.3.1 Mechanisms of grain refinement and carbide dissolution

Plastic deformation of HEAs has been investigated for over 10 years since they were first discovered [2,7]. However, studies on structure and properties of single phase FCC HEAs processed via HPT deformation have been reported only in the last few years [174,175]. In this study, the microstructural observations indicate that C alloying of the CoCrFeMnNi high entropy alloy significantly contributes to grain refinement during HPT processing.

It is known that the microstructure evolution during HPT occurs in a series of stages. The schematic describing the grain refinement of C0 alloy during the HPT is shown in Figure 4.11 (a). It starts with the formation of a cell structure and deformation twins with high dislocation density located in the cell boundaries [252,253]. Subsequently, inhomogeneous microstructure with a broad grain size and boundary misorientation distributions forms, which maintains over a wide range of shear strains. Nevertheless, the mean grain size gradually decreases with strain increasing and the permanent storage of dislocations in cell boundaries leads to an increase of their misorientations. Ultimately, a steady stage is reached where the mean grain size achieves the lowest value, and neither the mean grain size nor the GB misorientation distribution can be influenced by further deformation [253].

The main feature of the microstructure evolution of low SFE FCC alloys during plastic deformation is intensive deformation twinning, which significantly facilitates the grain refinement during SPD [89]. In the materials that deform by both twinning and slip the kinetics of microstructure refinement can be enhanced due to intensive twins formation [99,254]. Thin deformation twins, which are separated from the matrix by high-angle boundaries, readily transform into a chain of grains during the deformation.

Deformation twinning in the Cantor alloy is associated with its low SFE of ~21 mJ/ m^2 at RT [98,255]. The mean grain size of saturated microstructure is ~45 nm (Figure 4.5(a)), which is similar to the behavior of the equiatomic CoCrFeMnNi alloy during HPT [174]. It suggests that the two alloys have comparable SFE in essential. It was found recently based on first principles calculations that addition of C in CoCrFeMnNi increases SFE [256]. This finding was confirmed in CrCoNi MEA [257].

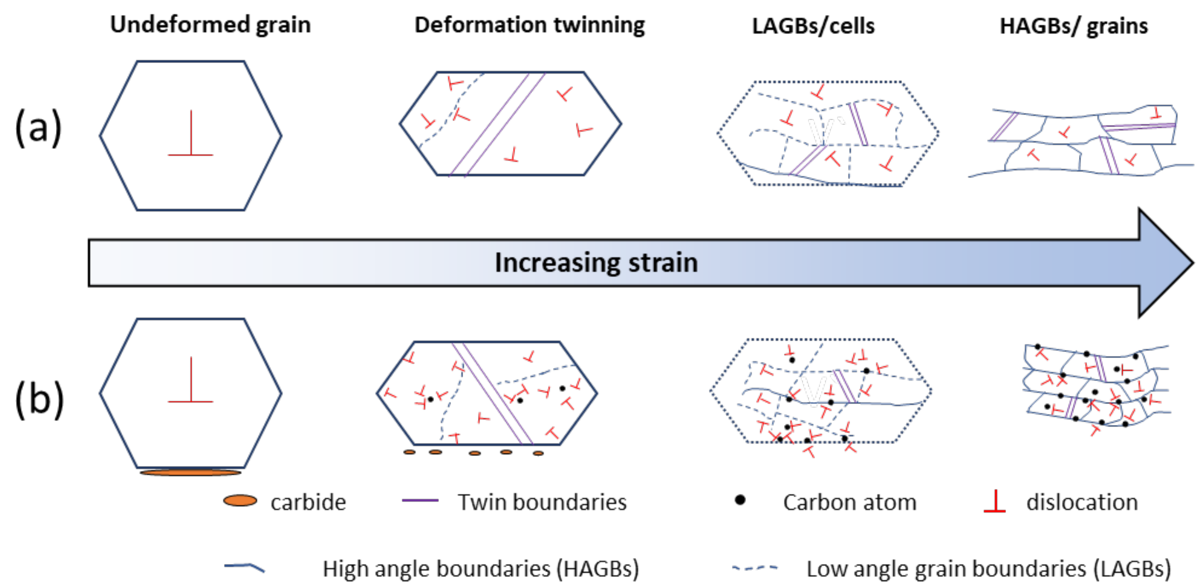

Figure 4.11 Schematic of microstructure evolution during HPT of: (a) C0 alloy; (b) C2 alloy.

With the C content increasing, the mean grain size of the saturated microstructure shows a decreasing trend. The mean grain sizes are 29 and 18 nm for the C0.5N3 and C2N3 alloys, respectively. The reduction in grain size can be associated with the segregation of C on GBs (Figure 4.10) as a result of the dissolution of carbides during HPT. Similar results were also reported in C45 steel [210,258] and pearlitic steel [259]. Several mechanisms may lead to strain induced dissolution of precipitates during SPD. It is known that high dislocation density [253], non-equilibrium GBs [260] and high vacancy concentrations [261] which form during SPD, provide the diffusion paths for interstitial C atoms. All the defects contribute to the diffusion or the atomic mobility during SPD: the dislocations can drag solutes [262] and act as diffusion pipes [263], the GBs are the fast diffusion paths and also drag solute when they move during SPD [264–266], and the strain induced vacancies directly enhance the atomic diffusion, respectively.

It is known that interstitial C atoms have a strong effect on dislocation cross-slip. Grain refinement starts from grain subdivision during plastic deformation on several length scales which is found to be universal in wavy glide materials like e.g., Ni [267] and iron [268]. However, grain subdivision also occurs in planar glide materials such as low SFE alloys, e.g. HEA [269] and TWIP steel [270]. In our case, different C contents from 0 to 2 at. % (nominal) was added to CoCrFeMnNi alloy. Despite some segregation formed on the GBs in C2 alloy, the C concentration in the matrix is close to the nominal one (≈2 at. %). The schematic describing the grain refinement of C2 alloy during the HPT is shown in Figure 4.11 (b). Due to the strong effect of C atoms, it results in a gradual transition in the type of dislocation configuration from planar (Taylor lattice) to wavy (cells and cell blocks) [270], which contributes to the formation of cell blocks. Since the size of initial cell blocks is limited by C atoms pinning the dislocations, the fragmentation trends to reduce the sub-grain size resulting in finer grains. GB migration is necessary to obtain a steady-state microstructure and to prevent a continuous decrease of the grain size [271]. However, the C segregation at GBs occurring during HPT provides the effect of pinning of the boundary migration; grains cannot grow up which results in finer grain size in the C2 and C0.5 alloys comparing with the C0 alloy. In pure Ni, the influence of C in the saturated microstructure was also analyzed [154]. It was revealed that the higher C content led to finer grain size after HPT in the saturation regime.

The evaluation of the XRD peak profiles revealed notably high values of dislocation density in all HPT-processed alloys. It is known that the dislocation density in SPD processed alloys is low because dislocations usually sink into GBs or self-organize into ordered substructures like sub-boundaries [253]. From dislocation densities in Table 4.2, we can approximately estimate how many dislocations reside in one grain. In the C0N3 alloy, each grain contains fewer than 30 dislocations. Comparing with the C2N3 alloy which has much smaller grain size, but contains about 50 dislocations per grain. These results provide support to the argument that C interstitial enhances the storage of dislocations during HPT processing even in grains with the finest size.

4.3.2 Carbon segregation behavior at room and liquid nitrogen temperature

In order to quantitatively analyze the fluctuations of carbon concentration in the matrix, 1-D concentration profiles were plotted for a cuboid shaped slab with dimensions 5x5x60 nm^3 along the Z-direction. Two typical linear concentration profiles of carbon for both alloys are shown in Figure 4.12. The inserted horizontal dashed lines correspond to the average C concentration of the selected APT volume. In the present study, the nominal carbon content in the alloy is 2 at. %, which is rather low concentration and usually leads to a large deviation in the statistics. As can be seen in Figure 4.12 (a), the mean C concentration is around 1.84 at. %, however, two peaks with a concentration of ~4-5 at. % reveal the pronounced C segregation in the RT sample. Whereas the random fluctuations of C concentration were plotted in Figure 4.12 (b) without any noticeable peak implying that this C segregations were not formed during the HPT process at LNT in the studied alloy, despite of a relatively higher mean C content of 2.04 at. %.

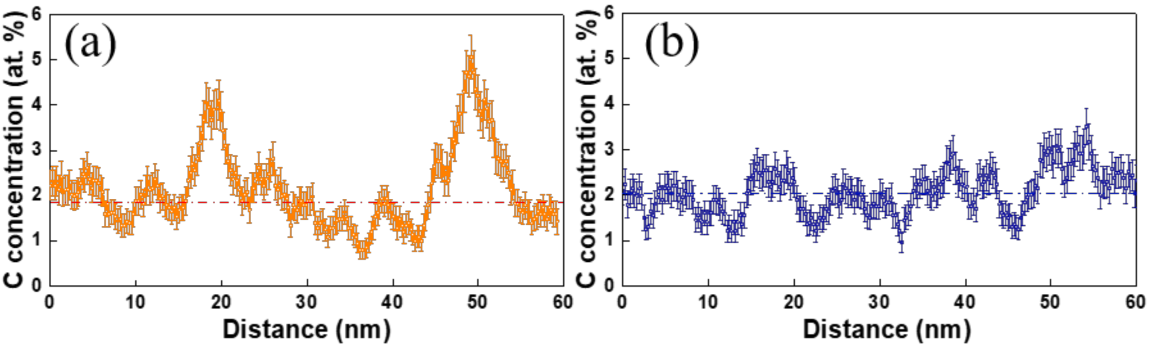

Figure 4.12 Linear concentration profiles of C atoms evaluated from the APT measurements of the samples processed by HPT at (a) RT and (b) LNT.

Normally Carbon atoms can easily segregate to the lattice defects like dislocations, sub-grain and grain boundaries in both BCC and FCC alloys [210,259,272]. In order to understand why notable carbon segregations were not observed in the sample processed at LNT, we should consider two points: (i) the source of carbon atoms to form segregations; and (ii) the transport mechanisms for carbon atoms to the segregation sites. In our previous subsection, we have shown that as-melted C2 alloy contains carbides precipitated along grain boundaries. We argued that the dissolution of these carbides during HPT released carbon atoms that subsequently segregated to grain boundaries. This phenomenon was also found in C45 steel processed by HPT at RT [210]. Present investigation indicates that HPT process at LNT most likely does not lead to a dissolution of carbides, but rather to their refinement. This directly follows from the fact that the carbon concentration in the FCC matrix is the same in samples after HPT processing at both temperatures, as shown by the XRD determination of lattice parameter (Figure 4.6). Indeed, released carbon atoms as a result of carbides dissolution can either dissolve in the lattice thus leading to its expansion, or form segregations. As none of that is observed in the sample processed by HPT at LNT, we conclude that at that temperature carbides are more stable against mechanically driven decomposition. As an example, the refined carbide particle was found at grains triple junction position in the LNT sample shown in Figure 4.13. Figure 4.13 (a) indicated the grain triple junction in LNT sample. Grain 1 and Grain 2 show [011] and [001] orientations of the zone axis correspondingly (see the inserted FFTs taken from the grains interior). The spots belonging to two grains are marked by the circles of corresponding colors. Aside from the spots of grains 1 and 2, additional set of spots is observed. It is indicated by the arrows in Figure 4.13 (b). Figure 4.13 (c) shows the inverse FFT image of Figure 4.13 (b) filtered with these additional spots. The interplanar spacing is ~ 0.254 nm, which is higher than the largest interplanar spacing of FFC structure (a_{111} = 0.211 nm). This number is quite close to $d_{(401)}$ = 0.252 nm of Cr_7C_3 type carbide. The reasons for the enhanced stability of carbides at LNT are not fully understood yet and require further investigations with the help of thermodynamic calculations, which is over the scope of present work. Here, we can suggest that it might be somehow related to frozen atom transport mechanisms such as dislocation drag [273], dislocation pipe diffusion [274], non-equilibrium grain boundary diffusion [266] and even vacancy-assisted diffusion [261], due to high energy barrier at cryogenic condition according to Fick's law [275].

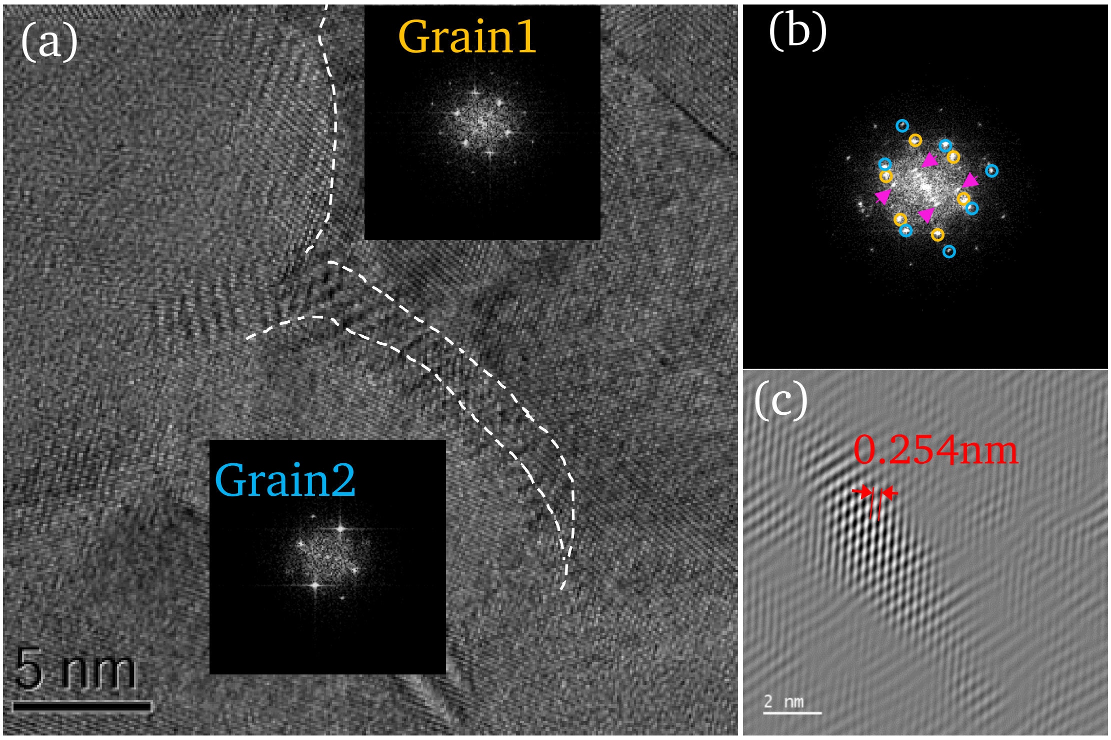

Figure 4.13 HRTEM image obtained at grain triple junction in LNT sample. (a) marked grain boundaries of Grain 1 and Grain 2 showing [011] and [001] ZA and corresponding FFTs. (b) FFT from the grain boundaries region. (c) shows the inverse FFT image of (b) filtered with these additional spots.

Another interesting observation of the present research is the formation of numerous twins inside of the nanocrystalline grains in LNT sample. CoCrFeMnNi type FCC HEAs are known to exhibit excellent mechanical properties at cryogenic temperatures, which is caused by the activation of twinning deformation [9,12,276]. In the above-mentioned works, a transition to twinning deformation is related to the pronounced temperature dependence of the yield strength. High flow stress at cryogenic temperature is an important trigger for the development of deformation twins in FCC high entropy alloys [99,277,278]. Additionally, the activation of deformation twinning can be related to the temperature dependence of the SFE as shown by first-principal quantum mechanical methods [255]. Numerous grain refinement. As a consequence of twinning deformation, the dislocation slip can be suppressed nano-scaled twins could be formed in LNT sample due to lower SFE, which can contribute to the observed, which leads to reduced generation of dislocations and vacancies.

4.4 Conclusions

High entropy alloys CoCrFeMnNiCx (x = 0, 0.5 and 2 at. %) with a reduced Cr content were processed by SPD using HPT. As a result, the microstructure was significantly refined down to nanometer grain size range, and a saturation of grain size was achieved. The interstitial alloying element C played an important role in the microstructure refinement during HPT and the resulting strengthening of the alloys under investigation:

i) C interstitial facilitated an increase in dislocation density and grain refinement during high-pressure torsion processing. The grain sizes are reduced to 45 nm, 29 nm, and 18 nm in the alloys with the C content of 0, 0.5, and 2 at. %, respectively. Meanwhile, the dislocation density increases sharply from 0.57×10^{16} m^{-2} up to 8.26×10^{16} m^{-2}. The deformation mechanisms responsible for microstructure refinement involved deformation twinning and dislocation slip.

ii) In the as-cast condition the alloy with 2 at. % C contained carbides at the grain boundaries, enriched with Cr and C. It appears that the carbides were dissolved during the high-pressure torsion processing. In turn, after three rotations of high-pressure torsion segregation of C at the nanograin boundaries were detected by XRD.

iii) Investigations allowed to conclude that the nano-structured single phase FCC high entropy alloy processed at room temperate shows carbon segregation at grain boundaries or in areas with high density of dislocations. However, cryogenic deformation is unfavorable to carbon segregation formation mainly due to high diffusion energy barrier at low temperature.

5 Thermal stability of nanocrystalline carbon alloyed high entropy alloy

5.1 Materials and experimental methods

Non-equiatomic high entropy alloy $Co_1Cr_{0.25}Fe_1Mn_1Ni_1$ with reduced Cr content and 2 at. % carbon was produced by mixing of pure constitutive elements by vacuum induction melting. Disks for HPT process were cut from the as-casted ingot with a dimension of ϕ 15× 0.8 mm^3. The distribution of the principal elements in as-casted alloy were determined by EDX, it indicated a dendrite and interdendrite structure as described in Chapter 3. The dendrite composition in the studied alloy indicated a higher Cr, Fe and Co content with an interdendritic composition rich in Ni and Mn, which is analogous to Cantor alloy [7]. HPT experiments were carried out at RT under a hydrostatic pressure of 6.5 GPa for 3 turns with a rotation speed of 0.5 rpm. After HPT the samples were subjected to process the post deformation isochronal anneal in a high vacuum quartz tube furnace for 1 h at 200, 500, 530 560 and 600 °C. These temperature intervals were selected according to the DSC measurement on C2N3 alloy, shown in Figure 5.1.

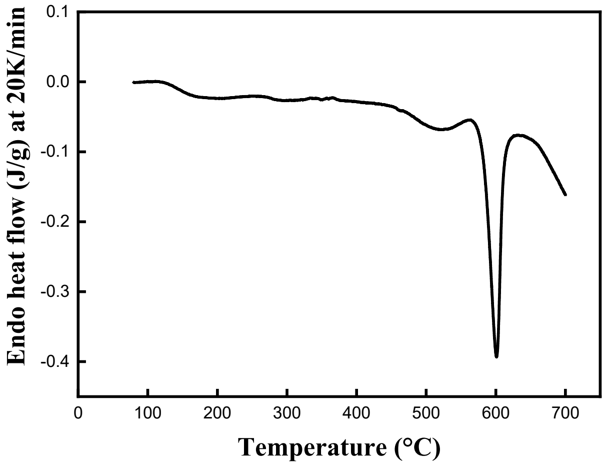

Figure 5.1 DSC heating curve of the C2N3 alloy, a strong exothermic peak on 600 °C and one around ~530 °C.

Conventional bright-field images, SAED and HAADF-STEM were obtained using the TEM) ThermoFisher Themis 300 and ThermoFisher Themis Z at 300 kV. STEM based core EELS images were acquired on ThermoFisher Themis Z at 300 kV using a Gatan GIF Continuum camera with an energy resolution of 0.6 eV and a step size of 0.5～10 nm. High resolution TEM and STEM images were conducted with ThermoFisher Themis Z. Subsequent TEM data analysis was performed with Velox and Digital Micrograph software. APT measurements were investigated using LEAP 4000 HR instrument. The APT measurements were conducted in voltage mode with a pulse fraction of 30 %, a pulse rate of 200 kHz and a detection rate of 0.5 % at 55 K. The 3-dimentional reconstruction and further analysis were provided using AP Suite software. The samples for TEM and APT characterization were prepared using a dual beam Ga FIB FEI Strata 400 instrument milled at 30 kV and final polishing at 5 kV.

5.2 Results

5.2.1 Microstructures after heat treatment at different temperatures

A brief microstructure evolution by conventional TEM investigation of HPT-processed nanocrystalline HEA after isochronal heat treatments at different temperatures is demonstrated in Figure 5.2. At low annealing temperature of 200 °C, the microstructure looks similar to that of the as-deformed state and shows a nanocrystalline grain size of ~20 nm with a single FCC phase given by the corresponding diffraction pattern. However, when the annealing temperature is increased to 500 °C, very weak additional reflections rings related to BCC structure appear in the diffraction pattern. From the bright-field images, there is no obvious recrystallization in this state and the grain size is more or less comparable to that in the as-deformed state i.e., the grain size is remaining the size of ~20 nm. After annealing at 530 and 560 °C, the BCC reflections are more distinct in the diffraction patterns. With slightly higher temperature increasing, the microstructures become coarser due to the growth of FCC grains and precipitates. The statistical mean grain size averaged for all phases in the sample annealed at 530 and 560 °C is 64 and 87 nm, respectively. At 600 °C, a notable grain growth is clearly presented and the microstructure shows equiaxial grains with an average size ~280 nm. Aside from the recrystallization, the BCC reflections are not found any more which indicates a presence of a single FCC structure at this temperature again. Furthermore, there is a pronounced change in the diffraction pattern from continuous to discontinuous rings, which is a result of grain growth. It is worth noting that the FCC matrix after HPT is relatively stable until 500 °C, when it started to decompose and the grains still show an elongated morphology meaning that recrystallization didn't occur.

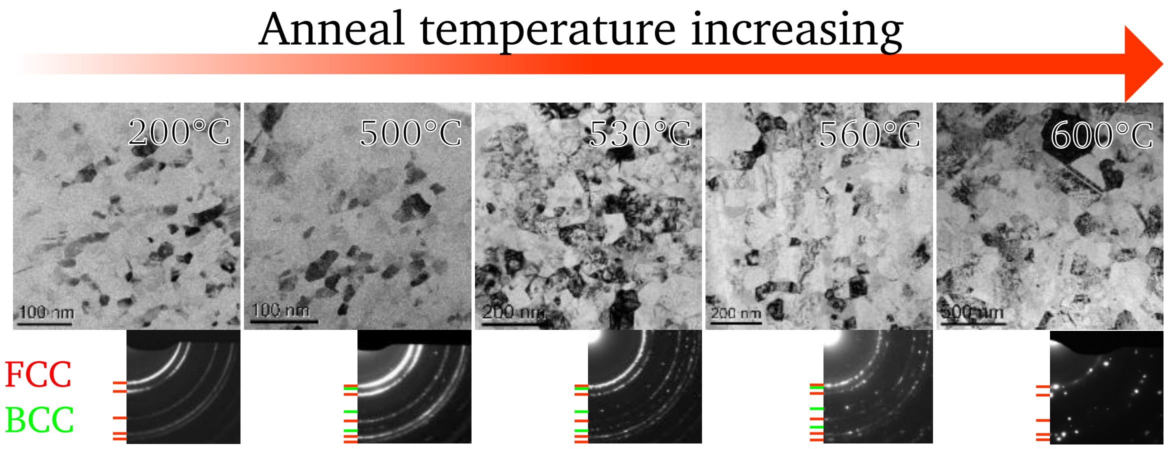

Figure 5.2 BF-TEM images and corresponding SAED of the C2N3 alloy after annealing from 200-600 °C.

5.2.2 FCC phase decomposition during annealing

In order to understand the FCC phase decomposition and recrystallization progress, the spectroscopy analysis using STEM-EELS was performed in samples annealed at 500, 530 and 600 °C samples. Figure 5.3 shows the microstructure and elemental map after heat treatment at 500 °C for 1 h.

Analogous to bright-field TEM images, the ADF image in Figure 5.3 (a) illustrated a nanocrystalline microstructure with a grain size of ~20 nm. STEM-EELS analysis reveals the formation of nano particles indicated by white arrows in DB areas, that are separated with IDB areas with white dashed lines. These nano particles with an average size of ~20 nm and enriched in Fe and Co are found to be randomly distributed only in DB. Also, in IDB region, there are some particles enriched in Ni and Mn with a comparatively small size of ~5 nm. These two types of particles are assumed to be similar to the CoFe B2 and NiMn $L1_0$ phases precipitated at annealing of Cantor alloy [279]. Moreover, elemental segregation of Cr and Ni was observed at grain boundaries in Figure 5.3 (b), in a higher magnification STEM-EELS map obtained with a step size of 0.5 nm. The inserted concentration profile measured along the white arrow crossing one grain clearly indicates the Ni and Cr segregations occurred at the grain boundaries. Interestingly, Ni and Cr segregations seem to be at a competition relationship as Cr is segregated on the one side of the grain while Ni segregated on the other side. However, these two elemental segregations are close to each other and are surrounding the same grain. On the whole, Ni, Mn, and Cr show a tendency to segregate on the grain boundaries, besides Ni and Mn indicated a co-segregation implying a nucleation of NiMn phase.

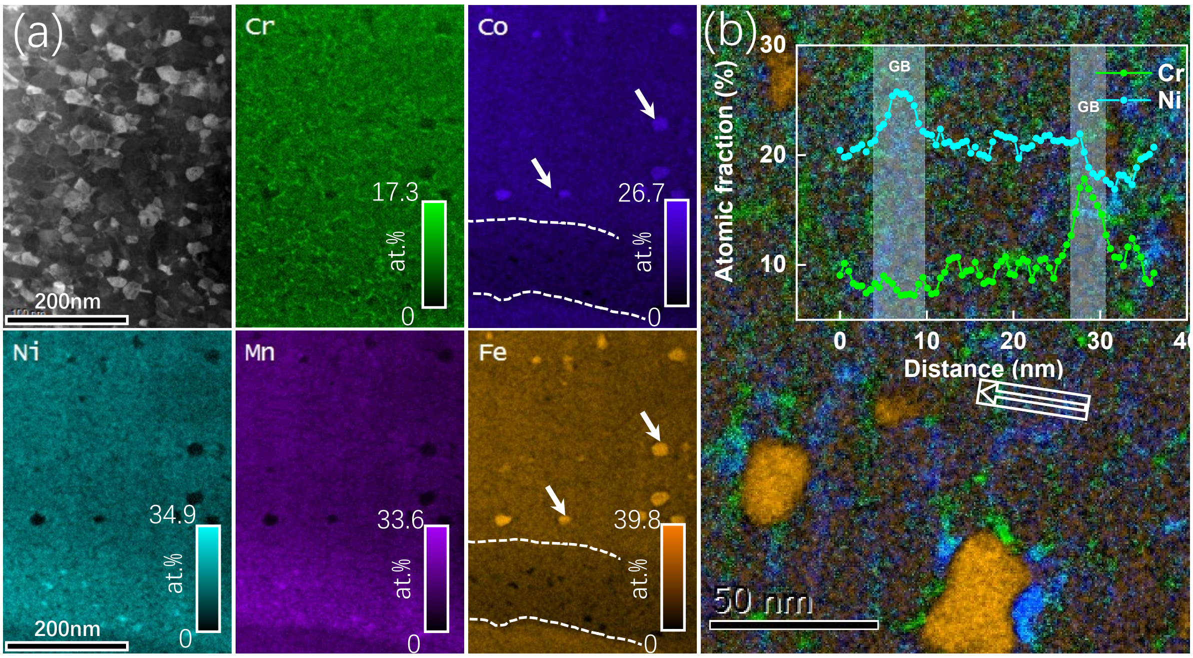

Figure 5.3 STEM-EELS elemental maps of C2N3 alloy after annealing at 500°C for 1 h. (a) The ADF image of spectrum imaging region and corresponding metallic elements distribution maps; (b) Magnified color mix map of Cr, Ni and Fe with inserted concentration profile crossing a grain along the white arrows displaying the fluctuations of Cr and Ni.

It had been discussed above that carbon segregations were revealed on the grain boundaries of C2N3 alloy in the as-deformed state; it is necessary to clarify the carbon effect on the elemental segregation phenomenon in the 500 °C treated sample. Hence, APT measurements were conducted with this sample. 3D reconstructed volumes along with iso-composition surfaces for C, Cr and Ni were shown in Figure 5.4 (a). The iso-composition values were chosen to highlight the segregation of the elements.

Cr and C iso-composition surfaces highlight segregation of respected atoms at the same grain boundaries as a co-segregation. The 1D-composition profile in Figure 5.4 (b) along the purple arrow across the GB shows that Cr (with the peak concentration of ~12 at. %) and C segregate with the concurrent depletion of Ni and Mn. Moreover, on the internal grain, Mn and Ni concentrations are a bit higher than Co and Fe ones meaning that the APT tip was obtained from the IDB region. In the other 1D-composition profile along the orange arrow shown in Figure 5.4 (c), it is seen that Ni and Mn co-segregations occur accompanied by the co-depletion of Fe, Co, Cr and C. The peak concentrations of Ni and Mn have reached ~31 at. % and ~36 at. % with a concomitant Fe and Co depletion to ~15 at. %. STEM-EELS and APT analysis reveals co-segregation of Cr and C, Mn and Ni as well, and the complex enrichment and depletion phenomenon occurring at the grain boundaries in the 500 °C treated sample.

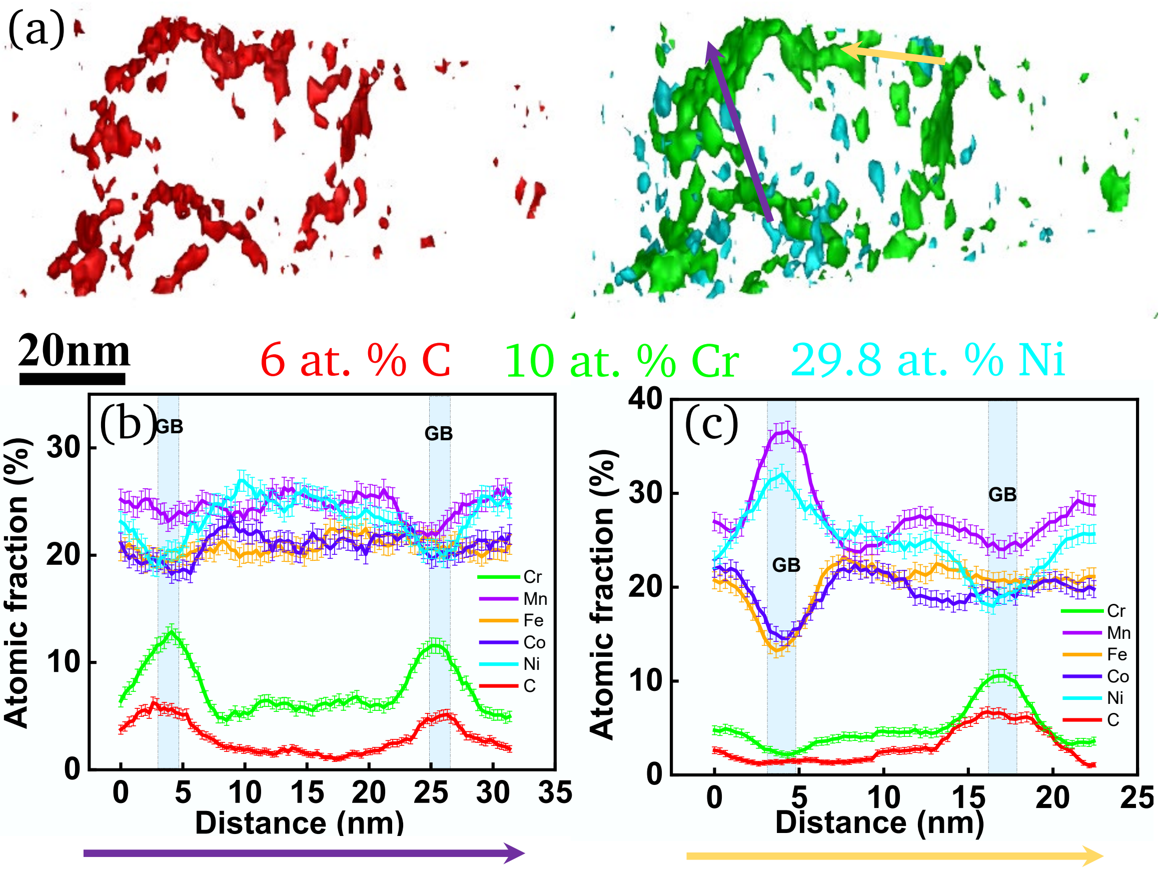

Figure 5.4 APT reconstruction of C2N3 sample after annealing at 500 °C for 1h shows segregation of C, Cr and Ni. (a) 6 at. % C iso-surface, 10 at. % Cr iso-surface and 29.8 % Ni iso-surface; The 1-D composition profiles taken along the direction indicated by the purple arrow (b) and the orange arrow (c).

Figure 5.5 shows the microstructure of the heat treated at 530 °C sample and corresponding elemental distributions characterized using STEM-EELS with a step size of 10 nm from the region in a white rectangle. As detailed in the elemental maps in Figure 5.5 (b), the selected volume contains two regions which correspond to the DB and IDB regions, respectively. Despite it cannot be distinguished in the HAADF image (Figure 5.5 (a)), the crucial difference between these two regions clearly reveals in elemental distribution maps (Figure 5.5 (b)), where the formation of numerous precipitates with different compositions is observed. As can be seen in the top part of the elemental distribution maps, there are two types of particles, one is enriched in C and Cr and the other one contains Ni and Mn. However, in the bottom region, there are additional precipitates rich in Co and Fe, which correspond to DB region. The detailed analysis of the chemical composition and crystalline structure of the precipitates are discussed below. This heterogeneous precipitation behavior is attributed to the chemical inhomogeneity presented in the as-deformed alloy after HPT processing.

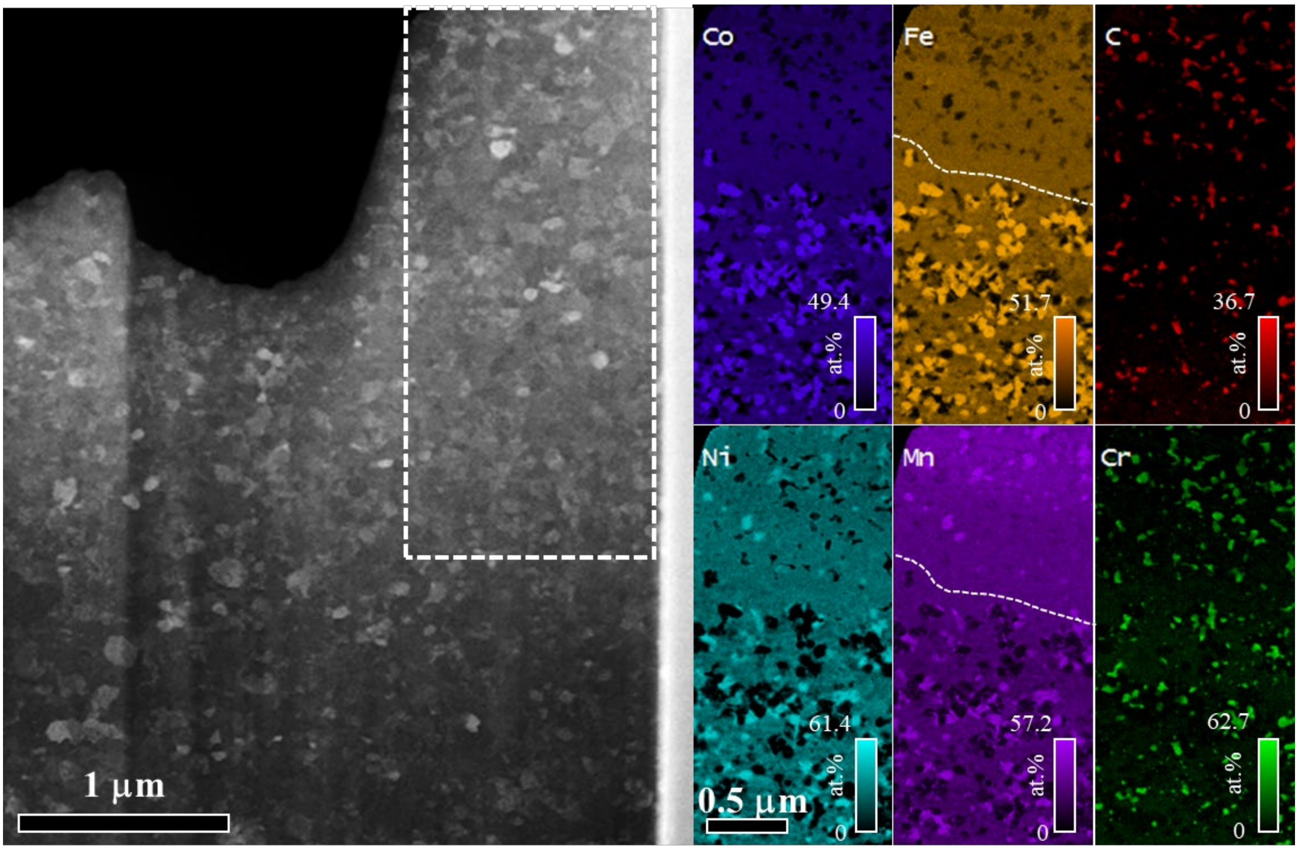

Figure 5.5 STEM-EELS elemental maps of C2N3 alloy after annealing at 530°C for 1 h at a low magnification. The dashed line in the Fe and Mn elemental maps indicate the border between DB and IDB.

Figure 5.6 demonstrates magnified image of the microstructure and elemental distribution maps from DB region in Figure 5.5 characterized using STEM-EELS with a step size of 0.5 nm. A significant growth of CoFe phase can be seen in Figure 5.6 (a), with a mean particle size of 80∼100 nm which is larger than the FCC grains nearby. These FCC grains have an equiaxial shape with an average size of 50∼100 nm, which indicated a notable grain growth in the FCC matrix. Despite of dramatic depletion of Fe and Co elements, the FCC phase shows a concentration of 3.5 Cr, 29 Fe, 22 Co, 23 Mn and 18 Ni (all in at. %), which is comparable to the chemical composition of the as-deformed DB region with distinct decrease of Cr. Furthermore, the nanoprecipitates with irregular shape, surrounding these CoFe particles and indicated by yellow arrows in the overall map, correspond to a NiMn phase. In addition, some nanoparticles enriched in Cr and C were observed at this temperature, which are assumed to be carbides or their precursors due to their high carbon content. A concentration profile line was created along the white arrow crossing the CoFe precipitate and a FCC grain to reveal the segregation on the grain boundaries and phase interfaces, shown in Figure 5.6 (b). The concentration profile illustrated co-segregation of two elements, Mn and Ni on/near FCC grain boundaries and at the interface between the FCC grain and CoFe phase. The co-segregation with a ~40 at. % Ni and ~30 at. % Mn at the interface is stronger than that at FCC grain boundaries (~29 at. % Ni and ~27 at% Mn). However, there is one significant phenomenon that the elemental distribution in the FCC grains is inhomogeneous in comparison with that in the sample annealed at 500°C. In particular, Ni and Mn showed not only a strong co-segregation at the grain boundaries, but there is also a notable enrichment with Ni and Mn in the region close to grain boundaries, which can be seen clearly in Figure 5.4 (b) and Ni map in Figure 5.4 (a). However, a concentration of Co and Fe is higher in the center of the FCC grains (see Co and Fe maps) according to the concentration profile. This subtle inhomogeneity in the elemental distribution may be induced by the thermally activated diffusion and finally lead to the decomposition of FCC phase. In addition, the carbon concentration is higher in the CoFe precipitates, which is assumed to occur due to preferable carbon contamination of CoFe particles during TEM measurements.

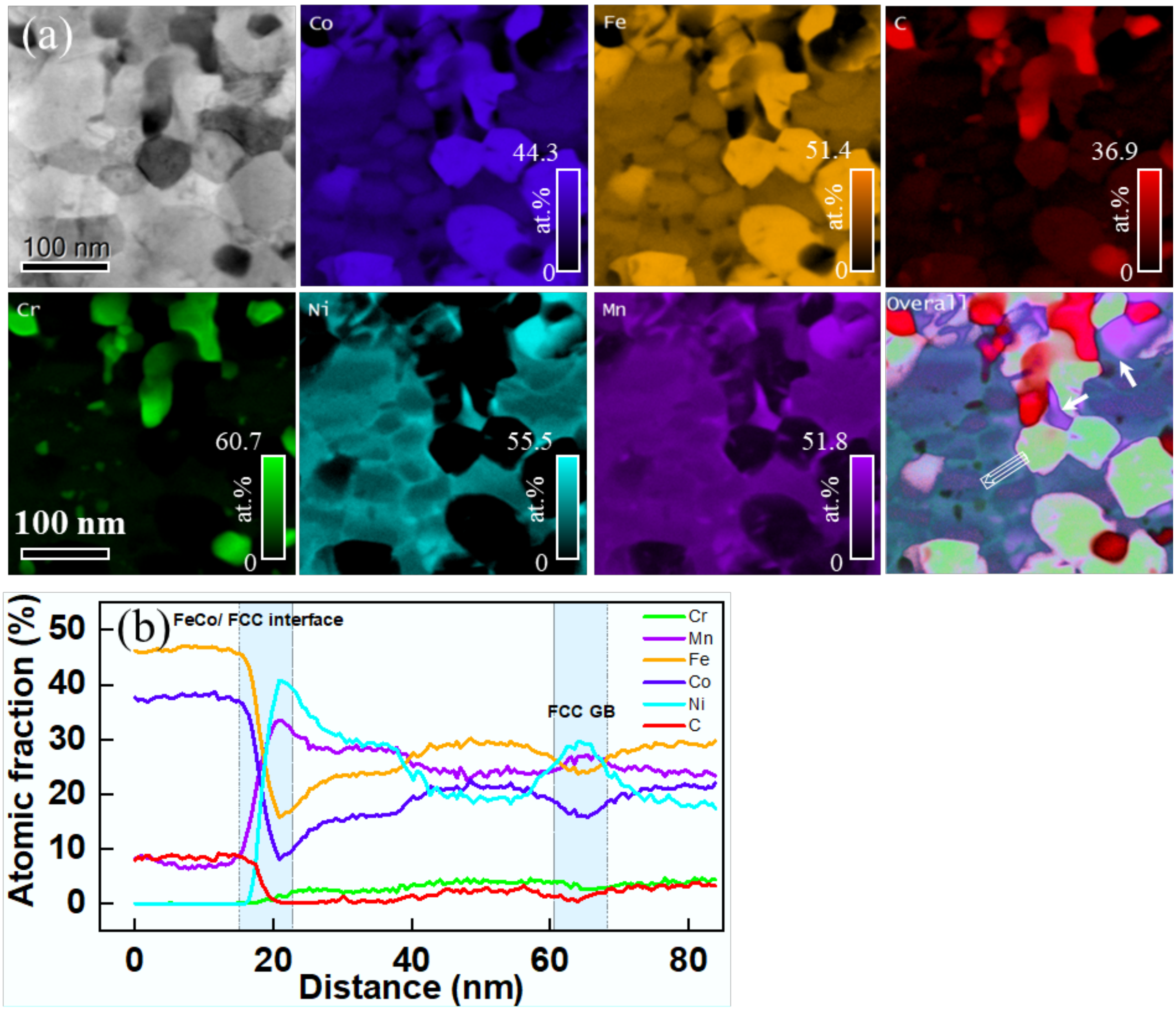

Figure 5.6 STEM-EELS elemental maps of C2N3 alloy after annealing at 530°C for 1 h at high magnification in DB region. (a) STEM spectrum image and elemental distribution maps with a step size of 0.5 nm (b) a concentration profile along the white arrow in the overall map.

In order to deeply analyze the inhomogeneous distribution of C, Co, Cr, Fe, Ni and Mn in the DB region of the 530 °C heat treated sample; APT investigation was performed. Figure 5.7 (a) shows the 3D reconstructed volume containing several precipitated particles. Figure 5.7 (b) demonstrates iso-composition surfaces of 55 at. % (C, Cr) in red, 75 at. % (Co, Fe) in orange, 90 at. % (Ni, Mn) and 35 at. % Ni in cyan. All the precipitates observed in the APT reconstructed volume are close to each other. The Ni segregation behavior is remarkable according to the Ni iso-surface, as Ni atoms appear like a cocoon around all the precipitates and FCC grains. This 3D-distribution of Ni atoms is analogous to that observed in the EELS construction in 2D plane (Figure 5.6). Furthermore, several proxigrams were established using the above iso-surfaces. Figure 5.7 (c) shows the proxigram from the 90 at. % (Ni, Mn) iso-surface which indicates a high Mn and Ni concentration in NiMn particles with a ratio of 1:1, in addition containing ~1.7 at. % Fe, ~0.6 at. % Cr, ~4 at. % Co and less than 0.1 at. % C. Figure 5.7 (d) illustrates the proxigram from the 75 at. % (Co, Fe) iso-surface. No obvious C solution (~ 0.1 at. %) can be seen in the CoFe particle, which confirms that high C concentration detected by EELS is induced by preferable carbon contamination during TEM measurement. CoFe phase is composed of Fe and Co (both~ 44 at. %), ~11 at. % Ni and Mn (7.5 at. % Mn, 3.6 at. % Ni). Furthermore, a higher concentration of Ni at the interface is associated to the cocoon-like distribution of Ni segregation. Similarly, the proxigram collected from 55 at. % (C, Cr) iso-surface was plotted in Figure 5.7 (e). The carbide shows a main concentration of 24 at. % C, 52 at. % Cr, rest of Fe, Co, Mn with approximate concentration of 23 at. % in total and a negligible Ni content, indicating a $M_{23}C_7$ type high-entropy carbide [280] according to the chemical constitution. Further, a composition of the FCC phase in the APT volume was given by the mass spectrum directly using a present bulk compositing analysis shown in Table 5.1. It indicates an exhausted C concentration (0.15 at. %) and a significant depletion of Cr in the FCC matrix suggesting a precipitation of $M_{23}C_6$ carbide formation nearby. The compositions of the matrix and the precipitates measured from APT are reported in Table 5.1.

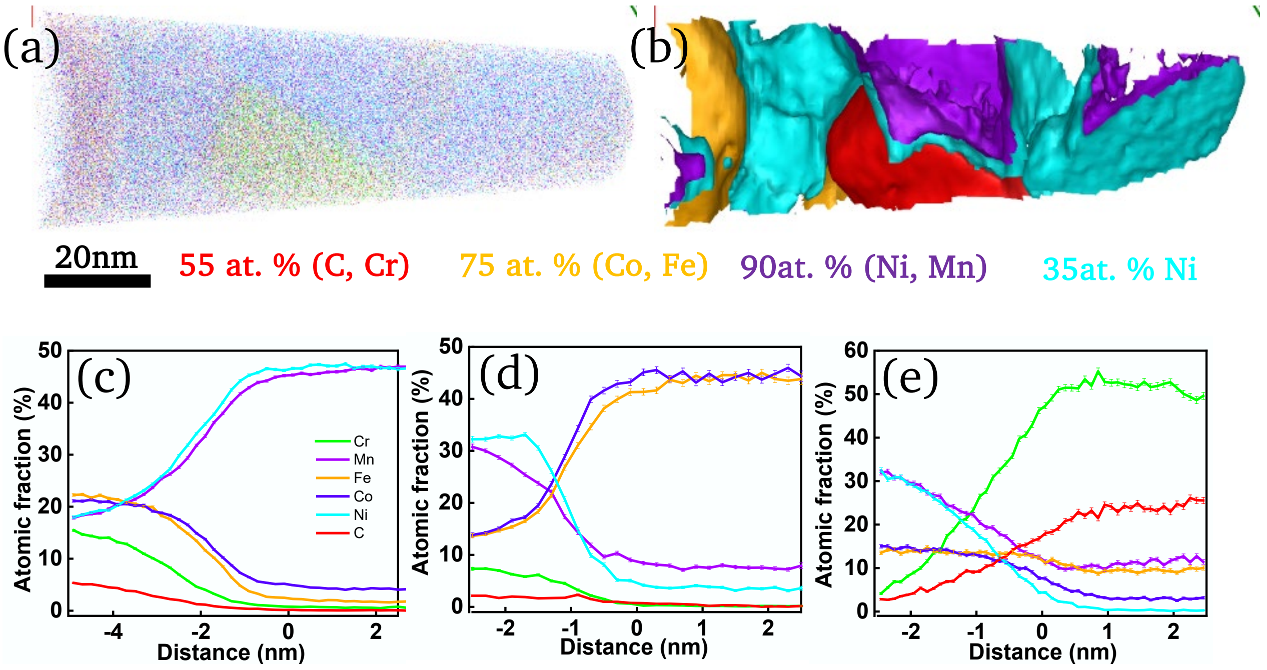

Figure 5.7 (a) APT 3D reconstruction volume of C2N3 alloy after annealing at 530°C for 1 h in DB region showing inhomogeneous elements distribution; (b) the iso-composition of 55 at. % (C, Cr), 75 at. % (Co, Fe), 90 at. % (Ni, Mn) and 35 at. % Ni; Proxigrams (d-e) created for the NiMn, CoFe and C,Cr iso-surface, respectively.

Table 5.1 The chemical compositions of all phases present in the analyzed APT volume in Figure 5.8.

phase	C	Cr	Fe	Co	Mn	Ni
CoFe	0.1±0.05	0.2±0.05	**44.1±0.7**	**44.3±0.6**	7.5±0.3	3.6±0.2
NiMn	0.05±0.02	0.6±0.1	1.6±0.1	4.1±0.2	**46.5±0.5**	**46.9±0.5**
CrC	**24.4±0.7**	**52.6±0.8**	9.4±0.5	3.1±0.3	11.1±0.5	0.4±0.1
FCC matrix	0.15±0.01	5.1±0.1	23.6±0.2	22.3±0.2	23.7±0.2	24.4±0.2

A STEM image and corresponding EELS elemental distributions of the sample annealed at 600 °C was shown in Figure 5.9 (a). The typical equiaxial grains after recrystallization were observed in the

ADF-STEM image with a mean grain size of ~200 nm. The EELS elemental distribution maps showed all the six alloy constitutive elements which presented in the carbides precipitated mostly at the grain triple junctions and some occasional round particles enriched in Cr located in FCC grains indicated by the white circles in Cr map. The Cr-rich particles do not contain C meaning that it is Cr-rich BCC phase or Cr-σ phase precipitates [174,198]. Also, some carbides contain higher concentration of Mn in the center, which can be the indication that carbide nuclei were Mn-rich. Figure 5.9 (b) plots a concentration profile crossing a carbide and a FCC grain boundaries. According to the profile, the carbide contains ~ 30 at. % C and 50 at. % Cr, indicating that it is M_7C_3 type carbide. Further, a weak segregation of Ni and Mn was observed at grain boundaries, which is comparably lower than that in 500 and 530 °C treated samples. It is predicted that the grain growth leads to a decrease of lattice defects density thus limiting the diffusion paths for all alloy constitutes.

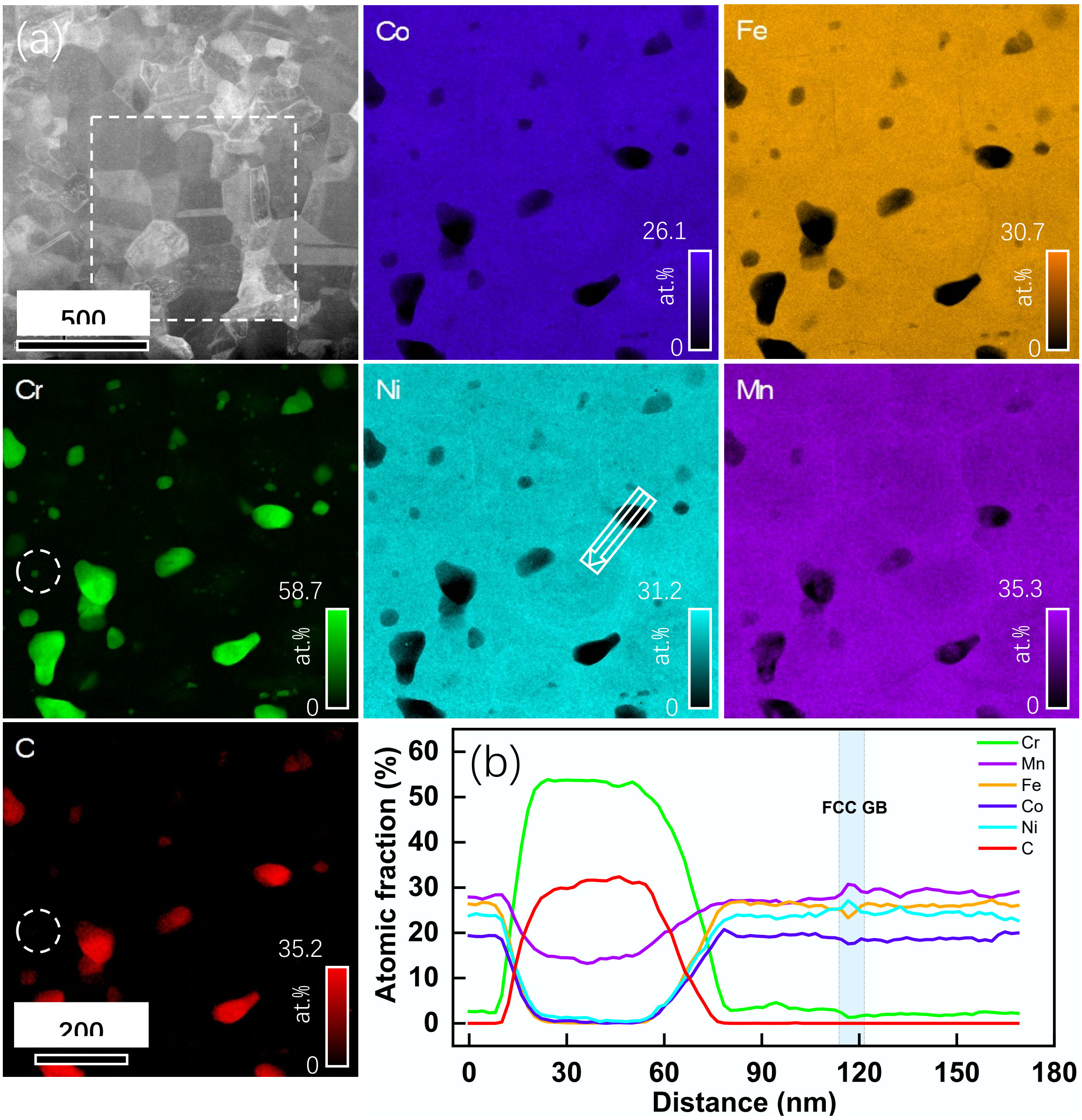

Figure 5.9 STEM-EELS elemental maps of C2N3 alloy after annealing at 600°C for 1 h. (a) STEM spectrum image and elemental distribution maps; (b) a concentration profile along the white arrow in Ni map, and white circles indicate position where is a Cr enriched particle.

A variation of the precipitates' size and volume fraction in the annealed samples in the temperature range from 500 to 600 °C was plotted in Figure 5.10. Both size and the volume fraction of precipitates in the 500 °C annealed sample are rather low in comparison with samples treated at higher temperatures. The mean grain size at this temperature is still close to that in the as-deformed alloy as shown in Figure 5.2 indicating a high density of grain boundaries, which contributes to the fast diffusion progress as discussed above. In the 530 °C sample a higher volume fraction of all the precipitates is observed, more than 25 %, which is attributed to the higher diffusion efficiency. However, mean size of the CoFe phase is ~100 nm which is much larger than FCC grains and other precipitate as summarized in Figure 5.10 (a) and confirmed in Figure 5.6 (a) as well.

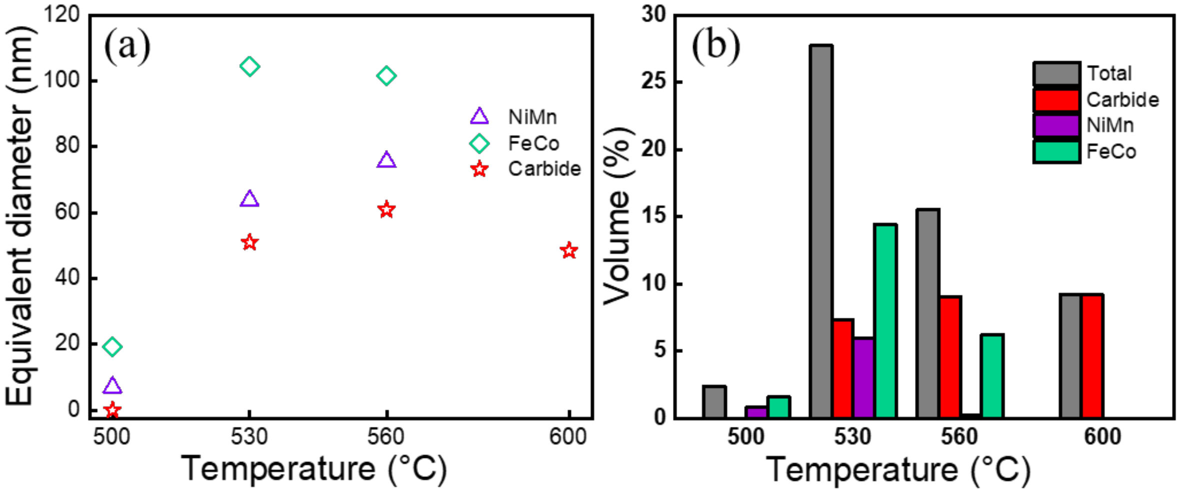

Figure 5.10 Statistics on the precipitates of CoFe B2 phase, NiMn phase and carbides from the C2N3 alloy annealed from 500 to 600 °C. (a) equivalent diameter and (b) the volume fraction of each precipitate.

5.2.3 Characterization of precipitate structures

HRSTEM images were acquired for CoFe phase and NiMn phase of 530 °C sample and HRTEM image was obtained for M_7C_3 type carbide in 600 °C sample, as shown in Figure 5.11. Figure 5.11 (a) shows atomic resolution Z contrast HAADF STEM image of typical CoFe phase on [001] zone axis, which indicates the atom configuration corresponding to the B2 structure, as clearly seen in the respective FFT in Figure 5.11 (d). Due to close values of atomic scattering factors of Fe and Co (3.51 for Co and 3.54 for Fe at Bragg angle [281]), it is impossible to recognize atomic species based on the contrast. However, a weak blurt superlattice reflection was found in the FFT indicated with yellow arrows. Later, a converged beam electron diffraction (CBED) was collected from the CoFe phase confirmed it's a BCC ordered structure. In addition, a calculation result demonstrates the lattice parameter of the B2 structure is ~0.293 nm, slightly larger than the pure binary CoFe intermetallic (ICSD 44731 cubic Im-3m structure, a=0.28845 nm [282]), which is related to the lattice distortion induced by the presence of interstitial C atoms and substitutional Ni, Mn and Cr atoms. Figure 5.11 (b) illustrated the HAADF STEM image of NiMn precipitate. In a standard binary Mn–Ni phase diagram [283], there is a chemically ordered face-centered tetragonal (FCT) $L1_0$ structure (ICSD104916, tetragonal P4mmm, $a = b = 0.261$ nm, $c = 0.349$ nm[284], as illustrated in Figure 5.11 (i)). However, Figure 5.11 (b) indicated a structure containing multiple nanotwins with a width of ~10 atomic layers. Corresponding FFT in Figure 5.11 (e) demonstrated a twinned FCC structure without chemical ordering, which is analogous to the result of the CBED of the NiMn phase in Figure 5.11(h). TEM analysis on the lattice parameters ($a = b = c \approx 3.76$ nm) shows there is no detectable compression of lattice parameter c, which suggests that the NiMn phase is not the FCT $L1_0$ structure, but rather a disordered FCC structure. In agreement with local HRTEM and CBED analysis above, the diffraction pattern of the 530°C sample reveals a broader ring near FCC {111} which is caused by the strong overlapping reflections of FCC matrix {111}, NiMn FCC phase {111} and CoFe B2 phase {110}. Furthermore, HRTEM image shows the Cr-rich carbide at the FCC grain boundary in Figure 5.11(c). The FFT of the carbide is detailed in Figure 5.11 (f) demonstrating a [-221] zone axis of the M_7C_3 carbide. A perfect overlap of the (111) spot of the FCC grain with the (212) spots of carbide indicates that the (111) planes of the FCC are exactly parallel to the (212) plane of the carbide as illustrated in Figure 5.11(f). Therefore, the orientation relationship between both phases is as follows: $(111)_{\mathrm{FCC}}$ // $(212)_{\mathrm{M7C3}}$.

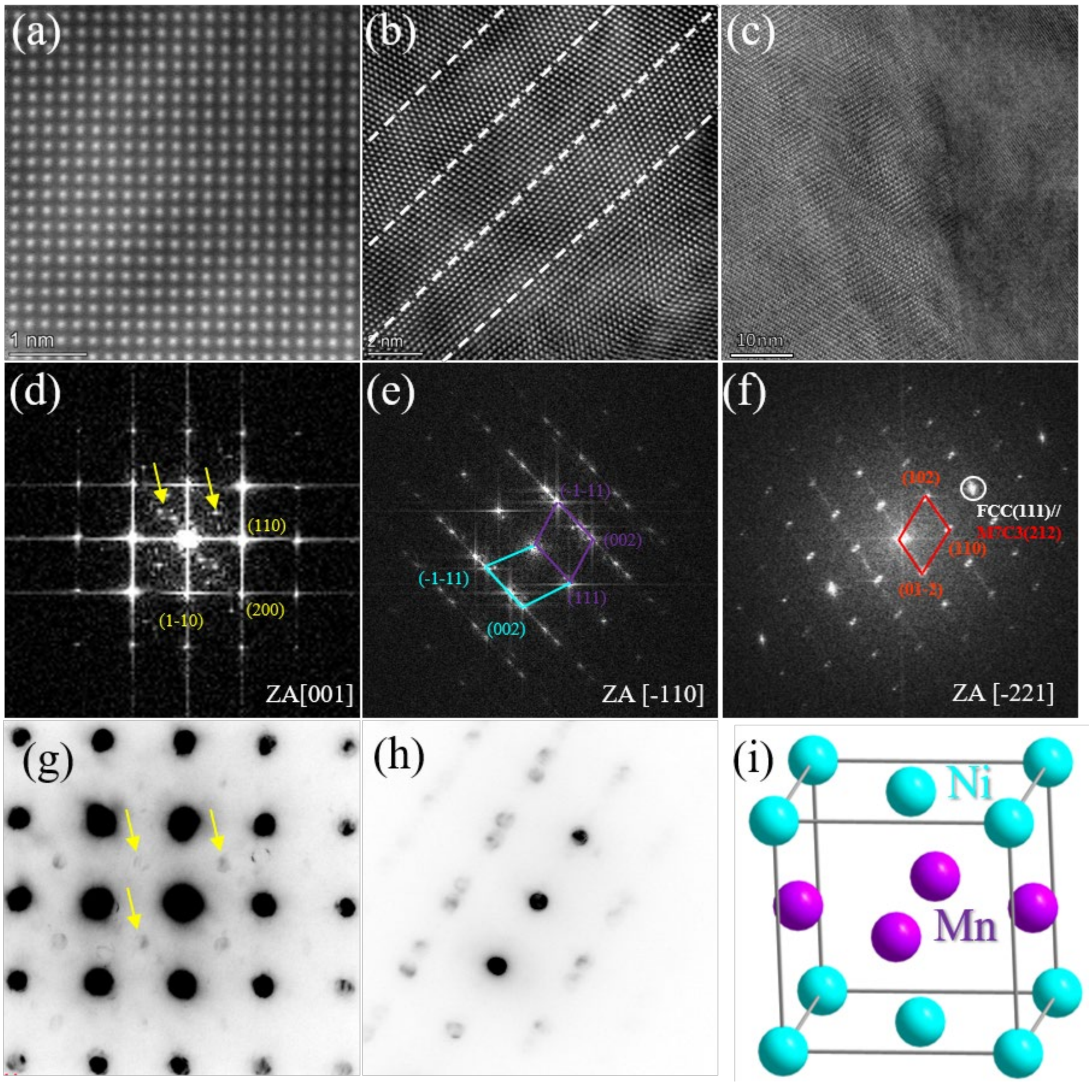

Figure 5.11 HRSTEM images of (a) a CoFe phase, (b) a NiMn phase in C2N3 alloy after annealing at 530 °C for 1 h . (c) HRTEM image of carbide on the FCC grain boundary in C2N3 alloy after annealing at 600 °C for 1 h; (d) is the FFT of (a) indexed with [001] zone axis; (e) is the FFT of (b) indexed with [-110] zone axis based on FCC structure; (f) is the FFT of (c) showing an orientation relationship of (111) FCC // (212) M7C3;(g) and (h) are the CBED of (a) CoFe phase and (b) NiMn phase, respectively; (i) shows the schematic of a chemically ordered NiMn FCT $L1_0$ structure.

5.3 Discussion

5.3.1 The elemental segregation and formation of the precipitate after annealing

In the present Chapter 5, a carbon alloyed nanocrystalline FCC system HEA was isochronally annealed at a series of temperatures. The results of the careful microstructural analyses illustrate the decomposition of the nanocrystalline single-phase solid solution, grain boundary segregation formation and new phases precipitation behavior. The annealing temperature ranges where particular phases are stable were established and compared with the literature data for the equiatomic Cantor alloy. It was established that after annealing at 500 °C for 1h the Cr, Ni and Mn atoms segregate at the grain boundaries, as shown in Figure 5.3 and Figure 5.4. As discussed in Chapter 4, grain boundary C segregations were revealed in HPT-processed samples.

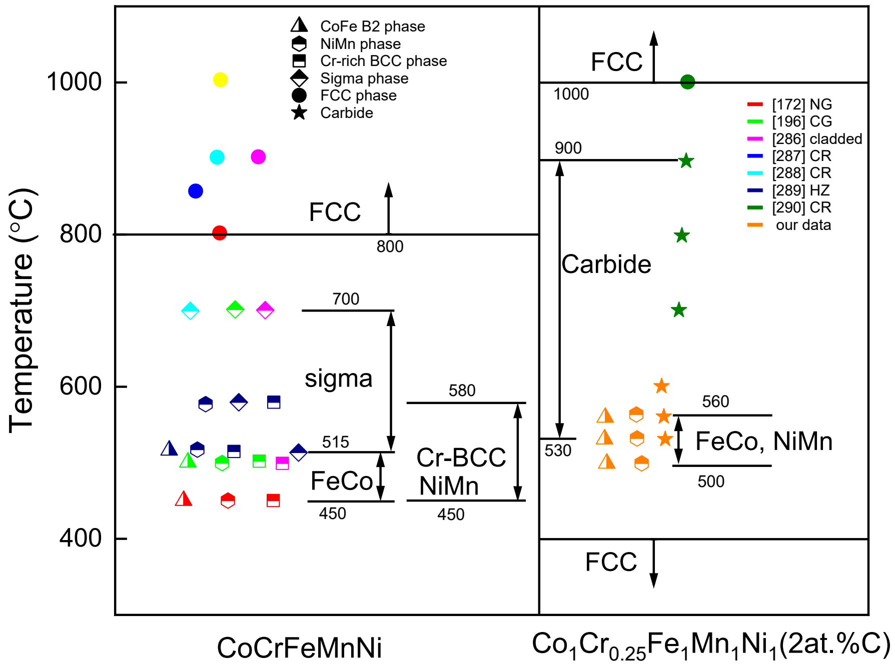

Figure 5.12 Temperature range of various phases precipitation in CoCrFeMnNi from literatures [172,196,280–284] and our experimental C2N3 alloy.

Based on the available literature data for CoCrFeMnNi alloy [174,198,285–289], the precipitation temperature intervals for all the detected phases are shown in Figure 5.12. In our as-deformed C2N3 alloy with a mean grain size of ~18 nm C segregations at the grain boundaries were found. Subsequent anneal processing was performed in temperature range from 200 to 400 °C, and the microstructure observation by TEM suggested the nanocrystallites with single FCC phase were stable without any new phase formation. The low-temperature annealing has led to an intensification of C segregation on the grain boundaries, which can be concluded from the comparison of Figure 4.10 and Figure 5.4. This pronounced C segregation induced by tempering at low annealing temperatures may contribute to the co-segregation of C and Cr in the sample annealed at 500 °C. In the study of Mantha et al. [201], non-equiatomic nanocrystalline CoCuFeMnNi alloy produced by HPT shows that prior to the formation of the secondary phase, Cu, Ni and Co segregate and Fe and Mn deplete at the grain boundaries at low annealing temperature of 250 °C, and new phases formed at 340 °C. Hence, this segregation and precipitation behavior may also occur in this temperature range in our alloy despite of the different constitutes.

When the C2N3 alloy is annealed at the intermediate annealing temperatures, such as at 500 °C, it shows a significant co-segregation of Ni-Mn and C-Cr. Meanwhile, a small amount of CoFe B2 phase with an equivalent diameter of ~ 20 nm in DB region and NiMn phase (or its precursor) with a size of a few nanometers in the IDB region were found in the sample annealed at 500 °C as shown in Figure 5.3. This kind of nano-sized CoFe B2 phase was characterized using TEM, and it was also detected in Cantor alloy in both coarse [198,287] and nano grained [174] states from 450 to 515°C (Figure 5.12). Besides, the $L1_0$ structured NiMn phase was found in the coarse grained alloy after a long term annealing in temperature range from 500 to 580 °C [198,287]. However, the NiMn phase in the nanocrystalline Cantor alloy after annealing at 450 °C is identified as a FCC phase [174], which is analogous to our results. Due to higher concentration of Cr (20 at. %) in Cantor alloy, the Cr-rich BCC phase formed in the Cantor alloy during the annealing from 450 to 580 °C. And the Cr-enriched σ phase indicated a wide formation temperature range of 515 to 700 °C. As a result of reducing Cr content and C addition in our experimental alloy, Cr-rich BCC phase is not found during the anneal processing from 530 to 600 °C, but a formation of numerous carbides was observed at the grain boundaries during the intermediate temperature annealing instead. Yet, extremely small Cr-rich granules were also detected in the grain interior in the alloy annealed at 600 °C, as illustrated in Figure 5.9, which could be Cr-rich BCC phase according to the composition analysis. The temperature interval of the carbide formation in the C2 alloy ranges from intermediate temperature (530 °C) to medium-high temperature (900 °C) [289], and at temperature higher than 1000 °C, a single FCC solid solution remains, which is 200 °C higher than it was observed in the Cantor alloy (Figure 5.12).

5.3.2 Elements segregation and new phase nucleation process during the annealing

It had been shown in literature that in the presence of carbon in the FCC matrix, as well as at the grain boundaries, the diffusion mobility of some elements is significantly affected in Cantor alloy [213,290,291]. Recently, Lukianova et. al [213,290] measured the tracer diffusion coefficients of C-alloyed Cantor alloy in the temperature range from 1173 to 1373 K. They found that the diffusion rates of all substitutional elements increase with the increasing content of C when the temperature was less than 1300 K, which was explained by the elastic distortions induced by interstitially dissolved carbon. Mn is the fastest isotope among all substitutional elements and Co and Ni are the slowest diffusing elements at 1173 K [213]. However, according to Gaertner et al., below 1000 K Ni is not the slowest element in the C-free CoCrFeMnNi alloy [292]. These findings hint towards a necessity to distinguish high-temperature and low-temperature diffusion behavior of alloying elements in CoCrFeMnNi alloy. In our case, notable diffusion processes occurred in temperature range from 500 to 600 °C, i.e. at temperatures which are much lower than these in the tracer diffusion experiments [213,290,291,293]. Hence, the diffusion coefficients and effective diffusion activation enthalpy of each substitutional element may significantly differ from respective values measured at high temperature in single crystal CoCrFeMnNi alloy. Furthermore, high density of defects present in the severely deformed alloy also produces a significant effect on the diffusion progress. As such, the total grain boundary area drastically increases by lowering the grain size. These boundaries can serve as fast diffusion pathways and represent energetically preferred nucleation sites for precipitates with much faster precipitation kinetics than that in coarse grained alloys where bulk diffusion prevails [174]. Hence, the diffusion coefficients measured in microcrystalline materials for bulk diffusion conditions may be not relevant in the nanocrystalline state and a much larger diffusivity mainly triggered by grain boundary diffusion should be expected. That is why strong segregation of Ni, Cr and Mn at the grain boundaries (Figure 5.4) and even some tiny nano particles or precursors of NiMn phase (Figure 5.3 (a)) were observed after anneal at 500°C, which demonstrated that sluggish diffusion effect is not attributed for the C alloyed nanocrystalline CoCrFeMnNi alloy.

In ref. [174], a Cr-rich particle was observed after 5 min annealing at 450 °C in the nanocrystalline Cantor alloy produced by HPT. In contrast to this, some particles of CoFe phase were obviously detected in the present investigation, whereas Cr was found to segregate at the grain boundaries without formation of any Cr-containing precipitates after 500 °C anneal. This effect was obviously associated with the fact that Cr is the strongest carbide-forming element among all the constitutive elements of the Cantor alloy. Note that C segregations were already present at the grain boundaries and subsequent anneal intensified the interstitial C segregation further. Hence, it is reasonable to conclude that Cr segregation phenomenon in the 500 °C treated sample is mainly caused by the pre-segregation of C. As can be found in Figure 5.3 (b) and Figure 5.4, there is a partitioning of elemental segregation at the same grain boundary: Ni and Mn co-segregate together on one grain boundary segment, whereas Cr and C on another segment (of the same grain boundary). This analysis confirms that in the same grain boundary region, co-segregation of Ni and Mn prevails at positions where C and Cr are depleted while the opposite behavior (co-depletion of Ni, Mn and segregation of Cr) takes place at other locations as illustrated in Figure 5.4 (b) and (c).

This segregation behavior is analogous to the work of Li et al. [202], where a co-segregation of Cr, Fe and Co at the grain boundaries near Ni and Mn co-segregation in the CoCrFeMnNi alloy with a small addition of carbon after the isothermal treatments at 450 °C for 6-48 h was reported. It hints that Fe and

Co may be the slowest diffusing elements in the nanocrystalline alloy at 500 °C. Subsequently, a strong segregation of Cr, Ni and Mn at the grain boundaries and a depletion of Fe and Co in the same regions, leads to an enrichment with Fe and Co in the grain cores. An uphill diffusion of Co and Fe concentration towards the center of the grain is illustrated in Figure 5.6. Meanwhile, there is significant depletion of Fe and Co at the grain boundaries. Therefore, we assume that the nucleation of CoFe ordered phase might occur in the grain cores while carbides and NiMn phase precipitated at the grain boundaries, especially at triple junctions. In a similar way, Gu et al. pointed out that the formation of long-range ordered structure occurred in the grain cores in a 500 °C annealed Cantor alloy after cold rolling which leaded to the abnormal hardening phenomenon [294].

To better understand the elemental segregation, solid solution depletion and new phase nucleation in the HPT deformed sample, a schematic is provided in Figure 5.13. (i) As can be seen in the left image, the as-deformed nanocrystalline sample shows the random distribution of all the constitutive elements in the FCC matrix accompanied with C segregation at the grain boundaries. (ii) As discussed previously, further C and Cr segregate on some grain boundaries when anneal temperature is going up to 500°C. Meanwhile, co-segregation of Ni and Mn appear on other grain boundaries which are devoid of Cr and C segregations due to the exclusive relationship. As a result of dramatic enrichment of Cr, Ni, Mn near the grain boundaries, Fe and Co enrich in the grain interior leading to a compositional precursor state, as shown in the middle image. (iii) With the longer anneal time or higher anneal temperature, the nucleation of carbides and NiMn phase occurred at the grain boundaries while CoFe phase precipitates in the FCC grains, which indicates a full decomposition of the original FCC solid solution. From Figure 5.3, it is obvious that the size of the CoFe phase particles is rather larger than that of the average FCC grain. Also, the decomposition of FCC solid solution may contribute to the formation of the NiMn precipitates and carbides on the grain boundaries during the CoFe phase formation, as displayed in the right image.

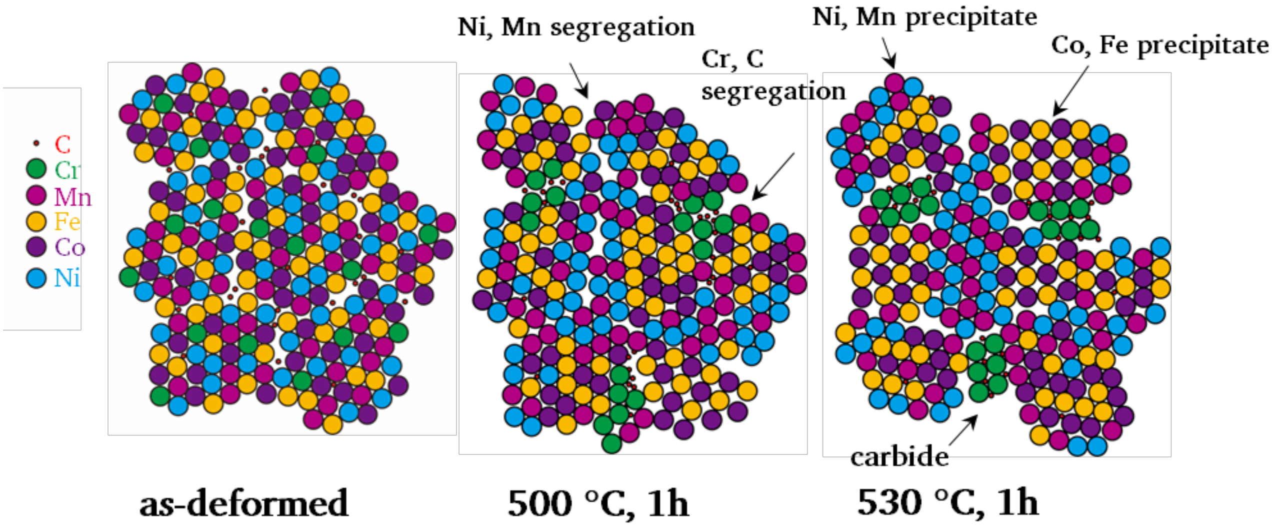

Figure 5.13 A schematic shows the progress of segregation, depletion and nucleation during the annealing process of C2N3 alloy from as-deformed state to the sample annealed at 530 °C for 1 h.

Subsequently, the grains continue to grow up at 560 °C to a mean grain size of ~90 nm, which is a similar size to that of CoFe precipitates at this temperature. Nevertheless, the volume fraction of both NiMn and CoFe phases dramatically decreases, as shown in Figure 5.10 (b). Additionally, Egorushkin et al. [284] point out that the NiMn phase is stable only below 665 °C in FeMnNi alloy system and CoFe B2 phase forms near the equiatomic composition in binary Fe-Co system approximately below 730 °C [282]. Grain boundaries are usually regions of high disorder owing to their reduced atomic coordination and complex structure. It is known that the high dislocation density [274] and vacancies [261] also contribute to the diffusion of both interstitial and substitutional elements, however, these important paths for diffusion become essentially limited because of the FCC structure recrystallization and dislocation recovery at the elevated temperatures. Hence, we believe that the phase equilibrium status has been represented in the sample annealed at 560 °C for 1 h under the assistance of the high-density defects. In the 560 °C processed sample, the volume fractions of NiMn and CoFe phase are ~ 0.3 % and ~ 6 %, respectively, which implies low ability of precipitation of these second phases at 560 °C in the experimental alloy. The phenomenon is much more pronounced in 600 °C heat treated sample in agreement with [59,61] that NiMn and CoFe phases cannot be observed any more at 600 °C. Massive carbides can be observed on the FCC grain boundaries and in triple junctions, as represented in Figure 5.9. According to the equilibrium phase diagrams constructed using the Thermo-Calc software [12], $M_{23}C_7/M_7C_3$ carbide formation temperature is up to 1000 °C in the studied alloy. So, it is reasonable that carbides remain in the 600 °C sample. Furthermore, it is worth to mention that there is still Ni and Mn co-segregation on the grain boundaries in the 600 °C sample as displayed in Figure 5.9 (b). This may imply the alloy annealed after 600 °C is still not in the phase equilibrium state.

5.4 Conclusions

In conclusion, phase decomposition in nanocrystalline $Co_1Cr_{0.25}Fe_1Mn_1Ni_1$ alloy with addition of 2at. % carbon obtained through HPT was studied systematically using TEM and APT characterization under a sequence of temperatures. The main conclusions from the present Chapter are as follows:

i) Formation of grain boundary segregations of Ni, Mn, and Cr, and intensification of present in the as-deformed state carbon segregations was revealed after annealing at 500 °C. Upon that it appeared that Ni and Mn co-segregate together in some areas of a grain boundary whereas Cr and C also co-segregate together in other areas of the same grain boundary.

ii) The nucleation of NiMn FCC phase occurred at grain boundaries in the sample heat treated at 500 °C and Cr-rich carbides were found at grain boundaries after annealing at 530 °C. Whereas in the grain interior a precipitation of the CoFe B2 phase was observed.

iii) The chemical inhomogeneity induced by dendritic structure in as-casted state leads to a heterogeneous precipitation phenomenon in the temperature range from 500 to 560 °C. CoFe phase is not observed in IDB region throughout the whole annealing process due to the low concentrations of Fe and Co in the domains. Whereas, both CoFe and NiMn phase formed in DB regions as balanced contents of metallic elements.

iv) In the 600 °C heat treated sample, carbides still exist, however, no CoFe B2 or NiMn FCC phase were found. This indicates the temperature range of the thermodynamic stability of these phases.

6 Mechanical properties of nanocrystalline carbon alloyed high entropy alloys

6.1 Materials and experimental methods

Vickers micro-hardness was measured with a load of 500 g with a dwell time of 10s on the polished surface of the samples using Buehler Micromet-5104 device. The distance between indents was maintained at a constant value of 0.5 mm. For CxN3 alloys, four series of measurements along the HPT disc diameters were conducted for each sample after HPT processing. For annealed samples, at least 10 points were measured and averaged in saturation regions where an equivalent strain was larger than ~60 ($r > 4$ mm).

Tensile tests were performed at RT at a strain rate of 10^{-3} s^{-1} using a custom-built computer controlled micro-tensile stage equipped with a high-precision laser extensometer P-50 by Fiedler Optoelectronics. For precise elongation measurements, the specimens were marked with TiO_2 paint using an airbrush. The tensile specimens were cut out from the HPT disks after heat treatments with a gauge length of 3 mm and a square cross-section of ~0.6 mm^2. At least three samples for each state were pulled to fracture to obtain statistically reliable results. The detailed sample size and painting demonstration were shown Figure 3.13 in Chapter 3.

6.2 Results

6.2.1 Mechanical properties of HPT deformed nanocrystalline HEAs with carbon additions

Figure 6.1 (a-c) shows the hardness variation along the radius of the HPT processed HEA samples with the different C content after 0.5, 1 and 3 rotations. The corresponding von Mises equivalent strain is also indicated in (c). The hardness of the C2 sample after HPT processing through different numbers of turns is shown in Figure 6.1 (a) in comparison with the initial hardness of the as-cast state (dashed line). A large gradient of the hardness occurs along the disk radius in all samples. After 0.5 turn, the hardness gradually increases from ~340 HV in the center to ~620 HV at the periphery. With increasing number of rotations, the hardness in the center becomes higher, and its increase along the radius becomes steeper until it reaches the saturation at ~620 HV. In the sample after three rotations, the hardness saturation is observed at the distance of 1.5 mm from the center. The hardness saturation most likely indicates achieving a stable (minimum upon these conditions) grain size. Similar behavior was observed in the C0 and C0.5 samples. It is apparent that an increase in the C content leads to a higher hardness of the studied HEAs in Figure 6.1 (b), however the overall appearance of the hardness distribution along the HPT-sample diameter with a drop in the center and the hardness saturation towards the periphery of the disk is very similar for all three alloy compositions. Figure 6.1 (c) shows the variations of the hardness values with Von Mises equivalent strain for the C0 and C2 samples. It confirms that the saturation occurs at the equivalent strain higher than 20 in both alloys. As can be seen in Figure 6.1 (d), a direct comparison of the hardness variation of C2N3 alloy deformed at RT and LNT. The hardness showed a significant increase from the HPT disc center to the area with saturated value of ~630 HV. Meanwhile, both samples exhibit a saturation at a radius of about 3 mm which corresponds to an equivalent strain of ~40, which likely indicates the grain size and defects density are at the same level in both samples.

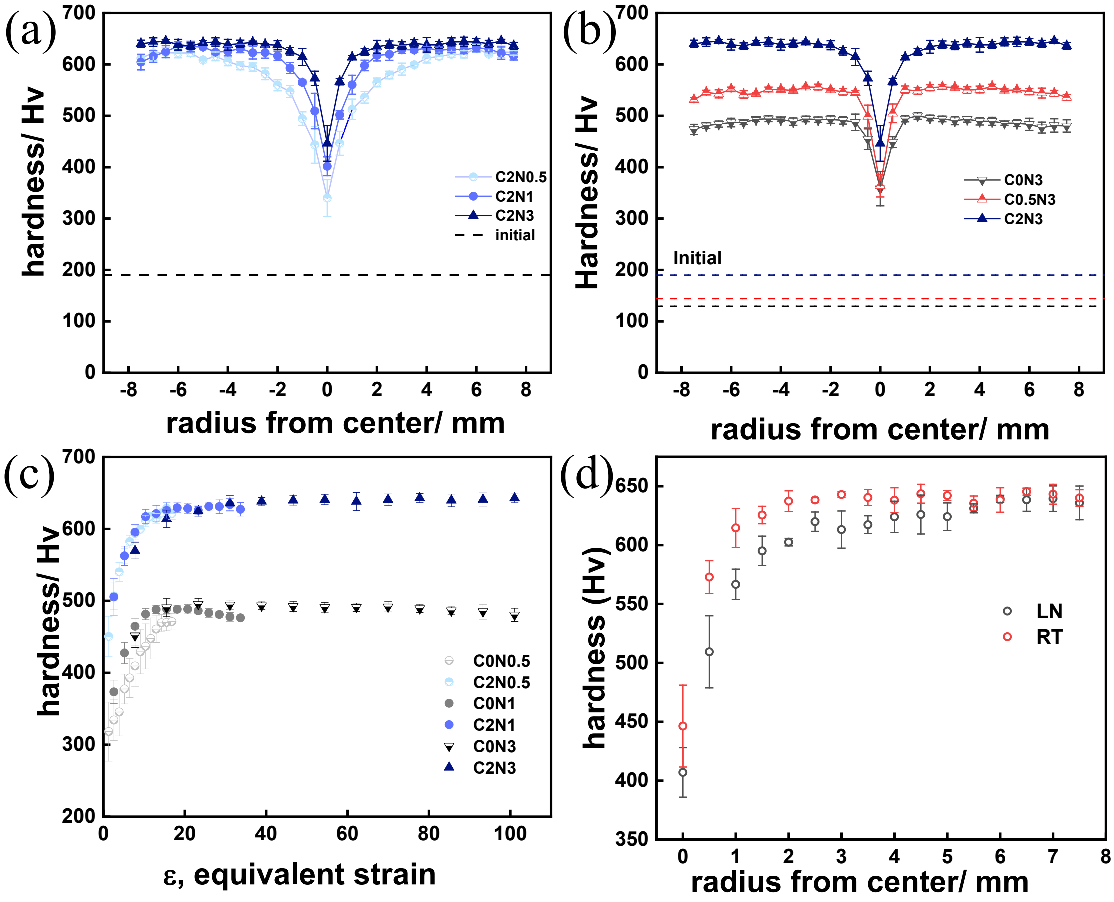

Figure 6.1 The variation of Vickers microhardness along the HPT samples' diameter for (a) C2Ny alloys; (b) CxN3 alloys; (c) Hardness evolution of C0 and C2 samples as a function of Von Mises equivalent strain, the hardness evolution of C0.5 alloy is not shown here because of the plots overlapping, but it has the same tendency; (d) hardness of C2N3 alloy processed by HPT at RT (293 K) and at cryogenic temperature (77 K).

Figure 6.2 shows representative tensile stress-strain curves for the as-cast and HPT-processed alloys with different C contents at RT. The coarse-grained alloys exhibit a considerable uniform elongation and high ultimate strength as a result of planar slip, high frictional stress and dynamic Hall-Petch effect, similarly to other FCC structured HEAs [8,9,12]. Figure 6.2 (b) shows stress-strain curves of the samples with different C content processed by three HPT turns. The HPT-processed samples show remarkably high strength at the expense of ductility (typical for cold-worked alloys) comparing with the as-cast states. The C0N3 alloy still shows a reasonable ductility with the elongation to failure of ~ 8 %. The C0.5N3 state demonstrates similar behavior. On the other hand, the C2N3 samples show almost brittle fracture with negligibly small ductility and ultra-high fracture strength of ~2.4 GPa. The tensile mechanical properties of the CxN3 alloys are summarized in Table 6.1

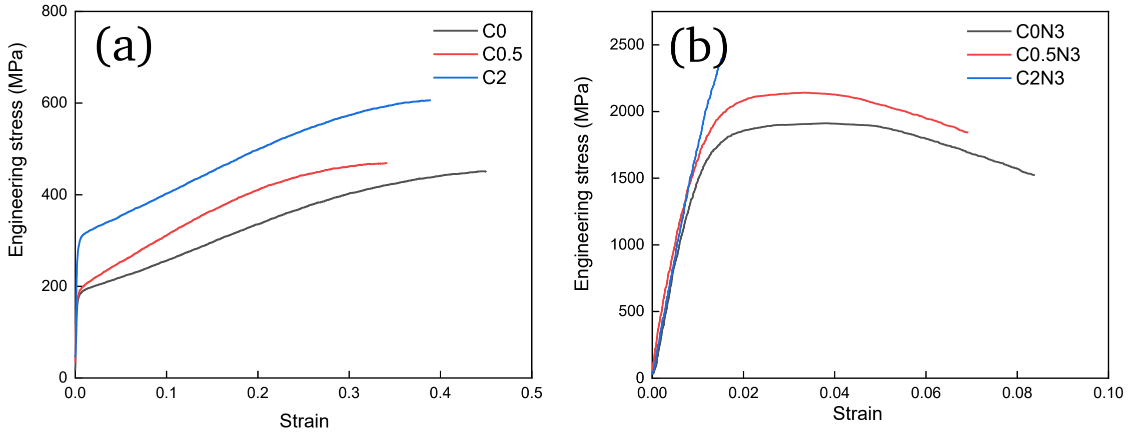

Figure 6.2 The tensile stress-strain curves of the studied alloys: (a) as-cast state; (b) CxN3 alloys.

Table 6.1 Mechanical properties of the as-casted and CxN3 alloys: yield strength (YS), ultimate tensile strength (UTS), uniform strain (ε_u), strain at fracture (ε_f) and Vickers hardness.

C content at. %	State	YS, MPa	UTS, MPa	ε_u, %	ε_f, %	Hardness, HV
0	As-cast	181	451	43.3	44.4	129
	N3	1667	1912	2.6	7.4	490
0.5	As-cast	190	468	33.2	35.4	144
	N3	1898	2141	2.1	5.7	550
2	As-cast	291	605	37.8	39.5	190
	N3	2402*	-	-	0.16	640

*Fracture occurred before the yield point.

The fracture morphology of CxN3 alloys after HPT and tensile testing are shown in Figure 6.3. Deep large dimples form usually on the surface of the Cantor type alloys in the as-cast or coarse-grained conditions thereby indicating a ductile fracture behavior [12,295]. Meanwhile, the HPT processed alloys also do not indicate obvious brittle fracture characteristics. Fine dimples are densely distributed on the fracture surfaces of the C0N3 and C0.5N3 alloys (Figure 6.3 (a) and (b)), which is corresponding to low ductility shown in Figure 6.3 (b) and Table 6.1. The dimples size of these two alloys is almost the same, ranging from tens to hundreds of nanometers that is considerably larger than the grain size. However, in the C2N3 alloy the "dimples" are much larger than in the other two alloys. The characteristics of the fracture surface in the C2N3 alloy can be characterized "vein pattern" which is typical of bulk metallic glasses [296,297]. The mechanisms responsible for the two types fracture morphology are different, as will be discussed below. Additionally, some deformed “micro-cracks” surrounded by fine dimples are found on all the fracture surfaces. The C0N3 and C0.5N3 alloys show wider cracks in comparison with the C2N3 alloy due to their better ductility. Investigations of cross-sections of as-deformed specimens revealed that these cracks look like thin and elongated ellipsoid shaped voids. Presumably, they were formed already during the HPT processing around oxides and sulfides inclusions, fractured into fine particles.

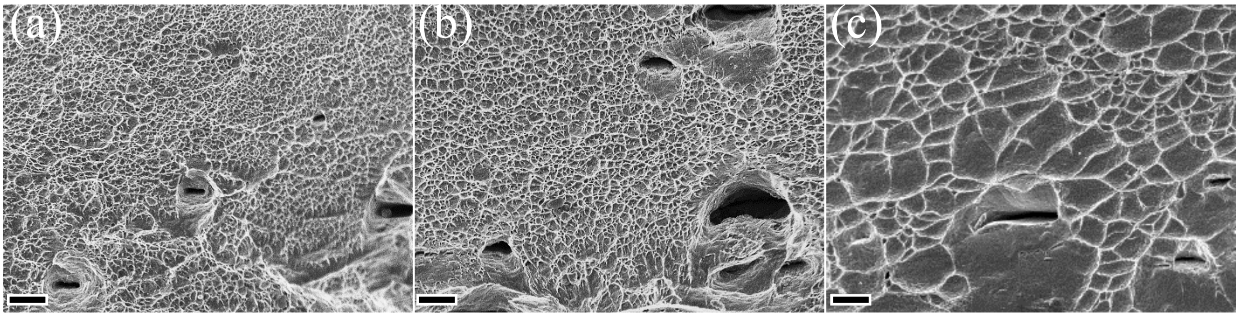

Figure 6.3 Fracture morphology of tensile samples of C0N3 (a), C0.5N3 (b) and C2N3 (c) alloys. Scale bars indicate 1 μm.

6.2.2 Mechanical properties of annealed nanocrystalline 2 at. % C-HEAs

Figure 6.4 shows the mechanical properties of 2 at. % carbon alloyed nanocrystalline HEAs after heat treatments in the temperature range from 200 to 600°C. The Vickers microhardness was measured around the HPT-samples periphery with a saturated microstructure. As demonstrated in Figure 6.4 (a), the results suggested that the hardness of the nanocrystalline C-HEA increases slightly up to 720 HV after annealing at 500 °C and then decreases rapidly with increasing annealing temperatures up to 600 °C. Representative plots of engineering stress against engineering strain curves are shown in Figure 6.4 (b). In order to compare the tensile properties, tensile curve of the as-HPT sample is also presented together with these of annealed ones. After an inspection, the yield strengths of the annealed samples indicate a slight increase up to ~2.4 GPa of 500 °C sample, which is analogous to the results of microhardness. Later, yield strength drops after 530 °C. Also, note that the 530 °C sample fractured before the yield point and broke into three pieces without any plastic deformation (see the inserted image in Figure 6.4 (b)), which indicates a completely brittle fracture.

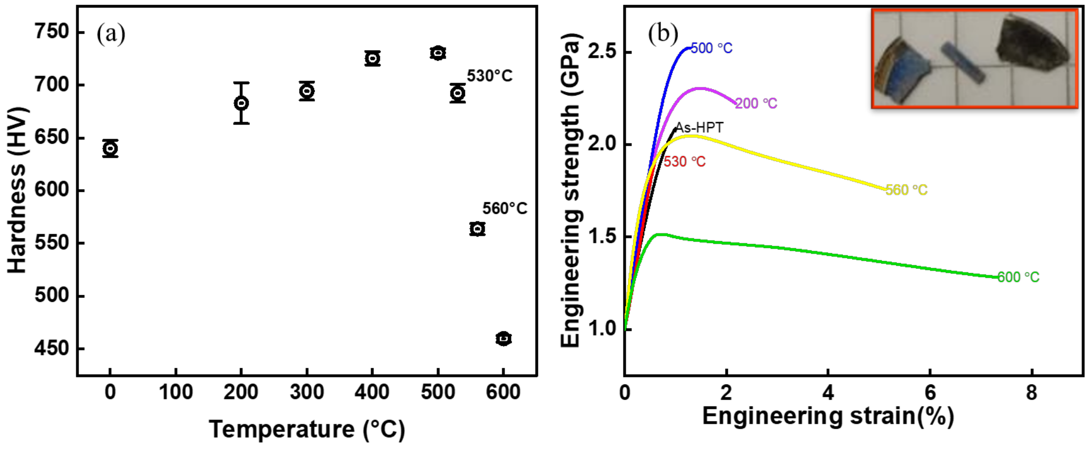

Figure 6.4 Mechanical properties of nanocrystalline 2 at. % C-HEAs after annealing process from 200 to 600 °C: (a) dependence of Vickers hardness on heat treatments temperatures; (b) engineering strain-stress curves.

Table 6.2 Mechanical properties of annealed C2 alloys: YS, fracture strain (ε_f) and Vickers hardness

Anneal temperatures °C	Hardness (Hv)	Hardness (GPa)	YS (GPa)	Ratio: Hardness (GPa)/YS(GPa)	Fracture strain, ε_f (%)
0	640(7.5)	6.28	2.09(0.06) *	3.00	0
200	682(19.3)	6.69	2.31(0.06)	2.89	1.34
500	730(4.1)	7.16	2.44(0.01)	2.93	1.03
530	692(8.6)	6.79	1.76(0.1) *	3.85	0
560	564(5.2)	5.53	1.90(0.03)	2.91	4.10
600	460(3.2)	4.51	1.41(0.06)	3.12	7.05

*Fracture occurred before the yield point; values in bracket indicate deviations.

Figure 6.5 represents the fracture surface morphologies of the anneal samples after tensile tests. As shown in Figure 6.5 (a), the fractography of the 200 °C sample demonstrated a similar appearance to that of as-deformed sample, the vein pattern-like dimples implying that both samples have a same fracture mode. Additionally, the fracture morphology of the 500 °C sample in Figure 6.5 (b) showed a dominantly dimpled fracture surface caused by a mixture of submicron-dimples and fine ridges coalescence. However, the completely brittle fracture behavior in the 530 °C sample occurred illustrating a quasi-cleavage feature shown in Figure 6.5 (c). It presented the particle-like granules and the granule sizes are close to the precipitates size in Figure 5.5 in Chapter 5 indicating a precipitate induced brittle fracture. Figure 6.5 (d) showed the trench-like dimples mixing the submicron dimples in the 560 °C sample, furthermore, inside the dimples, some particles were detected which may act as the initiation sites for these voids. Last, the fracture surface of the 600 °C sample exhibited equiaxed dimples with submicron size indicating a typical ductile-fracture mode. Similar, the particles, mainly carbides, were found in some of the dimples.

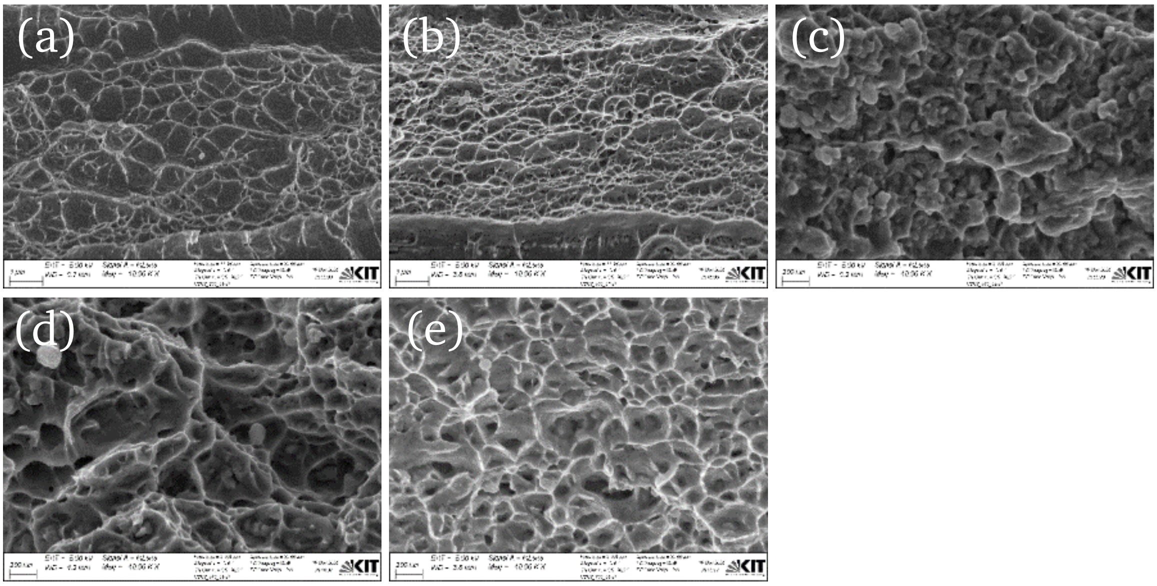

Figure 6.5 Fracture surface morphology of the samples annealed at (a) 200 °C, (b) 500 °C, (c) 530 °C, (d) 560 °C and (e) 600 °C.

6.3 Discussion

6.3.1 Strengthening mechanisms in nanostructured CxN3 HEAs

The mechanical properties at both RT and LNT of as-cast high entropy alloys under investigation with different C content have been discussed earlier in [12]. A significant increase of strength with increasing C content has been demonstrated. C doping contributes to the solid solution strengthening due to increased lattice friction stress. When comparing our results on mechanical behavior of as-cast CoCrFeMnNiCx alloys [18], one should keep in mind that in our case the tensile tests have been performed using miniature specimens with a gauge length of 3 mm and the cross-section area of 0.6 mm^2 which means that just several grains present in the sample cross section. It is known that the dimensions of tensile specimens can influence the resulting mechanical properties especially in respect of uniform elongation.

In this study, we focus mainly on the alloys processed by HPT for three turns. HPT resulted in a dramatic decrease of the alloys grain size down to nanometer-range. Mean grain size of the microstructure formed after three HPT turns was 47, 29 and 18 nm, in samples with the C content of 0, 0.5 and 2 at. %, respectively. There is a general agreement that for materials with such a small grain sizes dislocation slip becomes less important and even ceases to operate. Indeed, if we calculate the contributions of all hardening mechanisms based on dislocation slip (Hall-Petch grain boundary strengthening, strengthening due to stored dislocations and solid solution strengthening) we obtain unrealistically high strength values.

Grain refinement is one of the reason for governing strength of polycrystalline materials, where the strengthening can be described in terms of the empirical Hall-Petch relation using equation (1.3) [19,20]. We used a coefficient k_y = 0.494 MPa·$m^{1/2}$ obtained for a coarse-grained Cantor alloy [9]. The respective Hall-Petch contributions for the three alloys are summarized in Figure 6.6. The contribution of stored dislocations to the yield strength can be obtained from the Taylor equation[298] :

$$\sigma_{Taylor} = \mathrm{M_T}\alpha\mu b\sqrt{\rho} \tag{6.1}$$

where M_T is 3.06, the Taylor factor meaning orientation factor for FCC polycrystalline matrix, α is a constant equal to 0.2 for FCC alloys, μ is the shear modulus, here we use the modulus of Cantor alloy for this calculation [299], b is the magnitude of Burgers vector and ρ is the dislocation density [300]. Again, the calculated contributions are presented in Figure 6.6.

C atoms in solid solution contribute to the frictional stress of the alloy, and solid solution strengthening can be calculated as proposed in Refs. [301,302]:

$$\Delta\sigma_{ss} = fG(c\alpha^2\delta^2)^{2/3} \tag{6.2}$$

$$\delta = \frac{a_0 - a_{int}}{(1-c)a_0} \tag{6.3}$$

where the f is dimensionless parameter, c is the concentration of C, δ describes the lattice mismatch, and α is a dimensionless parameter that describes the type of dislocations, which is 3∼16 for screw dislocations, and > 16 for edge dislocations, here we use α=16, a_0 is the lattice constant of the C0 alloy, and a_{int} is the lattice constant of the C containing alloys. The C solid solution strengthening is ∼1 MPa and ∼85 MPa for C0.5N3 and C2N3 alloys, respectively, which is comparable with the experimental values of 9 MPa and 110 MPa obtained from the measured yield strength of the as-cast alloys (Table 6.1).

Furthermore, C segregation at GBs of nano-grains revealed in C2N3 alloy likely also contributes to the increased yield strength. Meanwhile, published studies show that that GB segregation, formed during SPD in some alloys, provide an additional strengthening mechanism. For example, in related work, Mo atoms segregating on GBs in nano-structured Ni-Mo alloy contributed to ultrahigh hardness and increased GB stability [303]; Mo, Si and Cr segregated on GBs in UFG 316 steel were produced by HPT at 400 °C while the segregation was not detected at RT and the segregation provided the comparable strength to that of RT processed alloy [304]; Xu et.al reported that ultrahigh strength with stable nanostructures was achieved in Al alloys with deformation-induced GB segregation of Cu [305]. Bobylev et al. proposed a model to explain the enhanced strength of UFG Al alloys provided by Mg segregation. In this model, segregated Mg atoms were treated as homogeneous ellipsoidal inclusions acting as the sources of elastic stresses affecting the emission of lattice dislocations from GBs [306]. It is plausible that in the present study, the interstitial C atoms segregating on GBs in the C2N3 alloy provided extra strength comparing with that of the C0 alloy after HPT processing, however, it is difficult to estimate this effect as the physical mechanisms behind it are still not clear.

Finally, the calculated grain boundaries strengthening, dislocation strengthening contributions in comparison with experimentally measured yield strengths are shown in Figure 6.6. The solid solution strengthening is not shown due to its small value. It is clearly seen that GB strengthening alone is already higher than the experimentally measured yield strength in all three HPT-processed alloys. These results indicate that the values of grain boundary strengthening obtained using the Hall-Petch equation are overestimated, and a deviation from the Hall-Petch law is observed in nanocrystalline C-doped CoCrFeMnNi alloys. Such deviations are well documented in literature for many pure nanocrystalline metals because Hall-Petch coefficient of bulk nano-crystalline alloys is anticipated to be smaller than that in coarse grained alloys and finally the inverse Hall-Petch was observed with the grain size deceasing to a few nanometers grain size [182,307–309]. For instance, in pure copper at the grain size below 10nm, the flow stress decreases sharply with decreasing grain size while increases for grain sizes larger than 15 nm, which indicates nanocrystalline copper has a strongest grain size effect at of 10-15 nm [307]. Furthermore, the inverse Hall-Petch relationship for a nanocrystalline FeNiCrCoCu HEA was predicted recently using molecular dynamics simulations [310]. In our case, the yield strength of the studied alloys after three rotations keeps increasing with increasing C content while the grain size decreases from 45 to 18 nm.

The dislocation strengthening contribution is around 0.8 GPa in the C0N3 alloy, approximately half of the measured yield strength, which is common in SPD processed HEAs [250]. The dislocation strengthening of the C0.5N3 and C2N3 alloys achieved 1.6GPa and 3.3GPa, respectively. Especially, the calculated dislocation strengthening in the C2N3 alloy is even higher than its experimental yield strength which points towards the operation of totally different strengthening mechanisms than the conventional Taylor and Hall-Petch ones.

In the interstitial HEAs with the fine, micron-scaled grains, GBs provide the major contribution to the strength as they serve as effective obstacles for dislocation slip [289,311]. The estimations made in this work demonstrate that in nanostructured HEAs dislocation slip and grain boundary strengthening become less important. The smaller is the grain size, the larger is the discrepancy between the calculated and experimental yield strength values, that means the less dislocation slip contributed to plasticity. However, we still observe the higher YS for smaller grain size and not the opposite as it is expected from the inverse Hall-Petch relationship.

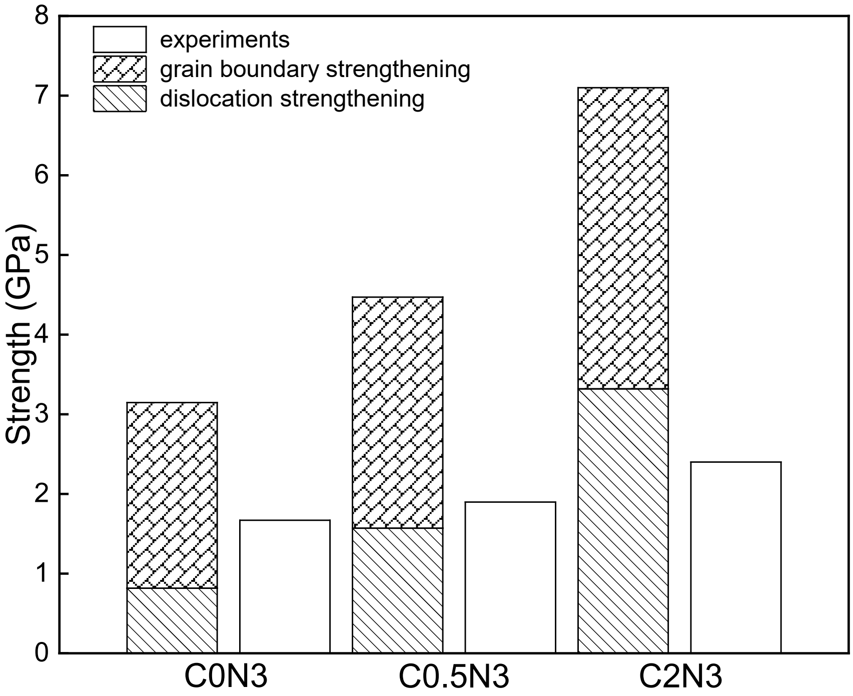

Figure 6.6 The estimated contribution of GBs and dislocation strengthening to the yield strength and corresponding measured values.

Obviously, C plays an important role in hardening in both the as-cast and HPT-processed alloys. For the as-cast alloys, the mechanical properties were mostly affected by the C concentration in the solid solution. For nanocrystalline alloys, impact of C alloying on mechanical behavior is more complicated. Generally, the plastic deformation of polycrystalline alloys is dominated by dislocation pile-ups. As the grain size is decreased, the number of dislocations piled up against a grain boundary decreases since this number is a function of applied stress and of the distance to the source [182]. As it has been already mentioned, for nanocrystalline materials, an additional plasticity mechanism has been proposed to operate: grain-boundary sliding [312]. In the C0N3 alloy, relatively large grain size (45 nm) and relatively low dislocation density (0.57×10^{16} m^{-2}) provided the possibility of dislocation pile-up during the plastic deformation. As a result, the C0N3 alloy presents some uniform elongation of 3.8 % and 8 % elongation to fracture which correlates well with the fracture surface shown in Figure 6.5 (a). The C0.5N3 alloy exhibited a similar tendency: the pile-ups formation is restricted by the higher dislocation density (1.85×10^{16} m^{-2}) and smaller grain size (29 nm), which leaded to a lower ductility and higher strength comparing with the C0N3 alloy, and probably to the emergence of grain boundary sliding. From the morphology of fracture surfaces in Figure 6.5 (a, b) these two alloys indicated the same ductile fracture condition. The formations of fine dimples may occur via the following steps: at the early stages of deformation, dislocations are emitted from GBs under the influence of applied stress, when intragranular slip is coupled with unaccommodated grain boundary sliding to facilitate voids formation at the GBs; triple junction voids and wedge cracks can also result from grain boundary sliding if resulting displacements at the boundary are not accommodated by diffusional or power law creep. These voids can grow and partially relieve the constraints on a small group of grains, individual single-crystal ligaments so created deform extensively and finally experience the failure to dimples [312].

Nevertheless, the situation in the C2N3 alloy is completely different, as this alloy exhibits different deformation and fracture behavior. Brittle fracture without any yielding or any evidences of plastic deformation was not detected in Figure 6.2. A very small grain size and the ultra-high dislocation density (8.26×10^{16} m^{-2}) preclude the formation of pile-ups formation and planar slip; deformation twinning is also suppressed in the fine-grained Cantor alloy [313]. Thus, the only possible way to induce plasticity is GB sliding. However, grain boundaries in this alloy are decorated with C segregation. On the one hand, C segregation enhances GB cohesion [314,315], on the other hand, they simultaneously retard grain boundary sliding which leads to high fracture strength but brittle fracture in the C2N3 sample. Focusing on the fracture surface morphology (Figure 6.5(c)), the vein patterns, which are typically observed in bulk metallic glasses, appear on the fracture surface of C2N3 sample. The overall appearance of the pattern is analogous to the fracture features formed by the separation of grease between two solid plates [316]. The origin responsible for the pattern formation could be largely attributed to shear-induced structural disordering or temperature rise caused by elastic energy release in the final fracture stage [297]. High levels of tensile stresses in the crack tip lead to local dilatation and hence blunting through nonlinear viscous flow [317]. The relaxation structure which reduced the available free volume increases the relaxation time, and in turn leads to embrittlement as crack-tip stress mitigation through viscous flow becomes less viable [318–320].

Talking into account similar grain size distributions, we assume the yield strengths of C2N3 samples under RT and LNT conditions could be comparable. In this study, we confirmed that RT alloy demonstrated remarkably high yield strength of ~2.4 GPa, but zero ductility, which we attributed to carbon segregations on GBs. We argued that as grain boundary sliding is a main deformation mechanism in such nanostructured alloys, and GBs are decorated with C segregations, GB sliding is retarded in RT alloy, leading to brittle behavior in tensile test. One can expect that reduced carbon segregation to grain boundaries in LNT alloy may lead to a reasonable ductility in LNT sample.

6.3.2 Heat treatments effect on strengthening of C2N3 HEA

As discussed above, UFG or nano-grained alloys achieved by SPD processing usually show significant strength improvement, however, normally with a considerable sacrifice of ductility, e.g. Ti [321]. Despite the success in achieving a highly-refined microstructure, it is readily apparent from Figure 6.4 that the tensile properties of the HPT-processed specimens are not satisfactory when testing at RT.

Accordingly, heat treatments of nanocrystalline C-HEA are necessary for improving the ductility. The dependence of mechanical properties, anneal temperature and grain size are summarized in Figure 6.7.

Remarkably, the results show a slight hardening after annealing in temperature range from 200 to 500 °C in Figure 6.4. Schuh et al. believed that the annealing-induced hardening occurred at a relatively low temperature and the hardening behavior is mainly attributed to the formation of a nanostructured multiphase microstructure in the HPT processed Cantor alloy matrix [174]. This could be a reasonable explanation for the sample treated at 450 °C which reached the maximum of the hardness (500 °C in Figure 6.7). Later, Shahmir et al. studied annealing effect on mechanical properties of a nanocrystalline Cantor alloy and they also thought that high strength of the sample annealed from 200 to 500 °C was attributed to the newly formed precipitates providing the strengthening [173]. However, the strength continuously slightly increased from 200 to 500 °C range in our case, in which no new phases nucleation occurred. The microstructure observations in Chapter 5 confirmed that the primary precipitation behavior was observed in the 500 °C sample which demonstrates the highest hardness. Meanwhile, even large volume fraction of precipitates was found in 530 °C sample (Figure 5.10), which is already softened. Therefore, the strengthening cannot be exclusively explained by precipitation. One other mechanism that can contribute to strengthening in the low temperature range is a reduction of the dislocation density upon annealing [212,322,323]. The nanocrystalline structure provides a large fraction of grain boundaries that can absorb dislocations during annealing. According to the results of annealing on HPT processed CoCrNi MEA [323], the decrease in dislocation density without significant change in grain size indicates that only dislocation recovery has taken place. This may lead to an increase in the stress required to activate new dislocation sources during straining. The reduced number of dislocation sources after annealing is speculated to be one of the reasons for annealing-induced hardening [212]. With such a high dislocation density as in C2N3 alloy (8.26×10^{16} m^{-2} in Table 4.2), the dislocation recovery and the non-equilibrium grain boundary relaxation may occur with the low energy barrier.

It should be noted that the significant segregation of alloy constituents at the grain boundaries occurred in C2N3 alloy after 500 °C treatment. Segregation strengthening mechanism has been proposed in SPD processed alloys, such as Al-Cu alloy [305], austenitic steels [304], Ni-Mo alloy [303]. This mechanism may be applicable in our case as well. In the 500 °C sample, Ni-Mn and C-Cr co-segregations are found at the grain boundaries shown in Figure 5.4 in Chapter 5. This segregation to grain boundaries in nano-grained C-HEA stabilizes the microstructure from coarsening, perhaps resulting in substantial hardening. Furthermore, C as an interstitial, can diffuse at relatively low temperatures 150~200 °C in steels [324], especially at the presence of high density of dislocations and grain boundaries, which significantly contribute to the diffusion progress. As can be seen in Figure 6.7, the sample after 500 °C annealing contains a negligible precipitate fraction but demonstrates highest strength. Thus, it is considered that the increase of strength in the samples annealed from 200 to 500 °C may be related to the presence of grain boundary segregations. As we discussed in former subsection, grain boundaries are decorated with segregations while the grain interior may still keep a relatively high level of dislocation density in the C2N3 alloy. These factors can significantly suppress the grain boundary sliding which contribute to high strength but less ductility.

With an increase annealing temperature to 530 °C, numerous precipitates formed at the grain boundaries with a significantly destructive effect leading to a brittle fracture, as shown in Figure 6.5 (c). Subsequently, the sample annealed at 560 °C shows a reduced strength comparing with sample annealed at 530 °C. This is mainly attributed to the grain growth and decrease of volume fraction of the precipitates as can be seen in Figure 6.7. Apart from this, the decrease of the volume fraction of the precipitates is also helpful to regain the ductility, however, it is the still remarkably limited due to presence of the large size particles at grain boundaries. In the 600 °C annealed sample, both acceptable ductility and high strength were obtained in the nanocrystalline C-HEA and the strength of the alloy may obey the classic Hall-Petch relationship again, although the hardening coefficient is larger than that of the Cantor alloy [9]. The nano-duplex structure is demonstrated in the sample annealed at 600 °C shown in Figure 5.9, with roughly 91 % FCC phase grains and around 9 % M_7C_3 carbide at the grain boundary. Hence, the yield strength can be represented in terms of the rule of mixture, using the following equation [325,326]:

$$\sigma_Y = f_{MC}\sigma_Y^{MC} + f_{FCC}\sigma_Y^{FCC} \tag{6.4}$$

where f and σ_Y denote the fraction and yield strength of the duplex microstructure of the sample annealed at 600 °C. The yield strength of the FCC phase can be evaluate using equation (1.3) whereas the strength of M_7C_3 carbide is around 6.3 GPa [327]. As a consequence, the yield strength calculated with equation (6.4) can be roughly estimated to be 1.43 GPa, which is close to the experimental value of 1.41GPa shown in Table 6.2. The typical Hall-Petch relationship may not be applicable in present alloy throughout the entire anneal experiments as there are more factors, such as dislocation density, precipitation, grain boundary segregations. Therefore, the nature of the strengthening mechanism of the samples could be more complicated under the condition of behaviors of the impact factors mentioned before in the sample annealed at the intermediate temperatures.

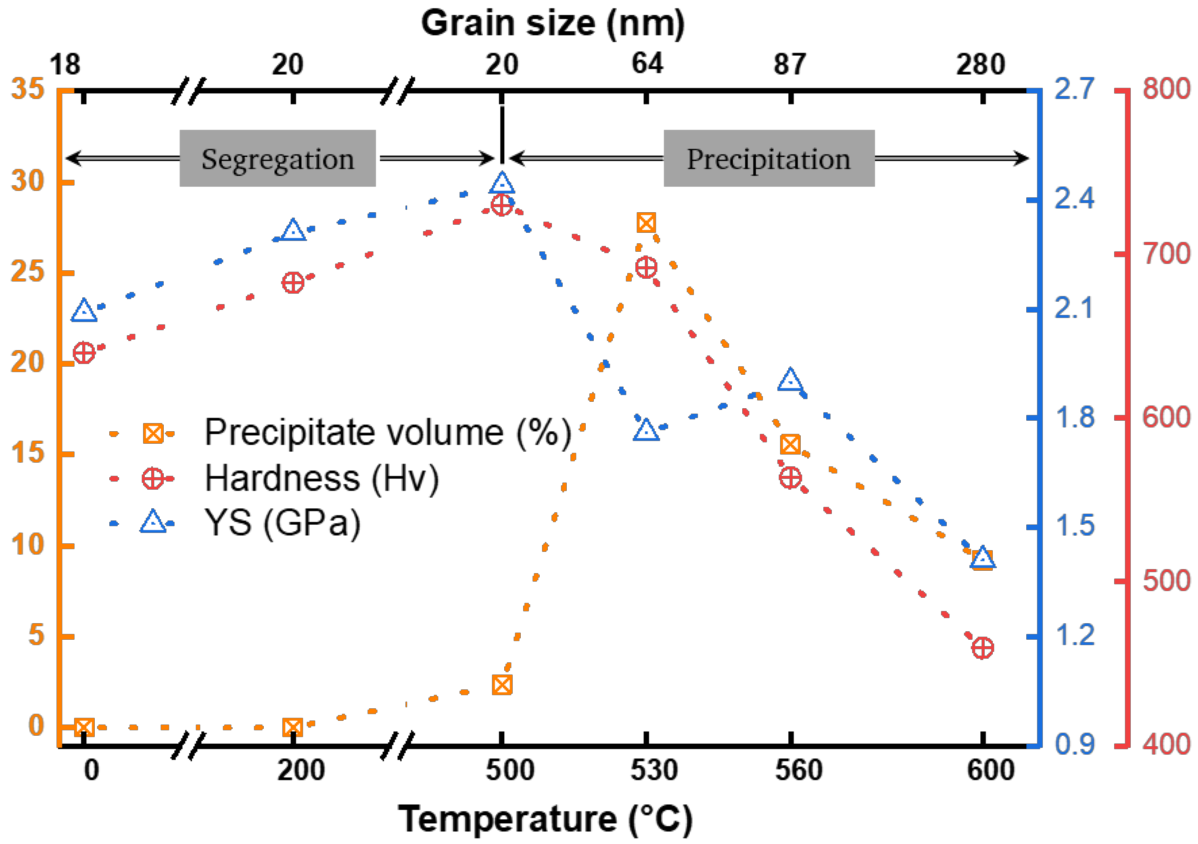

Figure 6.7 The dependence of hardness, yield strength and precipitates fraction via anneal temperature and grain size.

6.4 Conclusions

In this Chapter, hardness and tensile properties of the HPT-processed and subsequently annealed CxN3 samples were analyzed. The findings can be summarized as follows:

i) In the CxN3 alloys, the contribution of the conventional strengthening mechanism, such as grain size and dislocation strengthening via Hall-Petch and Taylor relationships, do not explain properly the overall strength of all studied nanocrystalline alloys. The deviation between experimental and calculated data increases with decreasing grain size and increasing C content suggest that the classic approach is not applicable.

ii) The mechanical behavior can be mainly attributed to the nano-grain size, high dislocation density and C segregating on the boundaries of nanograins, which lead to very high strength of 2.4 GPa but zero ductility in C2N3 alloy, and to a transition of fracture mechanism from ductile to brittle.

iii) In the annealed C2N3 samples, the hardness and yield strength slightly increase after anneal in the temperature range from 200 to 500 °C. This abnormal strengthening may be attributed to the recovery of dislocations, segregation and perhaps formation of ordered structure in the FCC matrix.

iv) Formation of numerous precipitates at 530 °C led to a brittle fracture. Subsequently, the alloy annealed at 560 °C exhibits a better balance of strength and ductility due to a grain growth and reduced fraction of precipitates. Finally, the 600 °C heat treated alloy shows high strength and resealable ductility attributed to the large grain size and the absence of embrittlement phases.

7 Summary and outlook

7.1 Summary

In this thesis, $Co_1Cr_{0.25}Fe_1Mn_1Ni_1$ high entropy alloys with 0, 0.5 and 2 at. % C addition were processed by high pressure torsion. Nanocrystalline HEAs were successfully obtained by means of severe plastic deformation. After obtaining nanocrystalline HEAs, the mechanical properties were studied via microhardness and tensile tests while the corresponding microstructures were investigated using various techniques including conventional and analytic electron microscopy, atom probe tomography and XRD analysis. In addition, thermal stability and mechanical properties of the 2 at. % C alloyed nanocrystalline HEA were investigated as above.

As discussed in Chapter 4 that C interstitials facilitate an increase in dislocation density and grain refinement during high-pressure torsion processing in the C-alloyed (0, 0.5 and 2 at. %) $Co_1Cr_{0.25}Fe_1Mn_1Ni_1$ alloys. The grain sizes are reduced with increasing with C content after three HPT turns. Meanwhile, the dislocation density significant increases by more than 100 times with increasing of carbon content from 0 to 2 at.% in the alloy. The deformation mechanisms responsible for microstructure refinement involved deformation twinning and dislocation slip. It appears that the carbides were dissolved during the high-pressure torsion processing. In turn, after three rotations of high-pressure torsion segregation of C at the nanograin boundaries was detected by APT. The segregation of C was suggested to result in finer grains in the C-doped alloys due to a pinning effect.

In Chapter 5, the anneal were performed in 2 at. % C added nanocrystalline alloy in the temperature range from 200 to 600 °C. It was established that the alloy keeps a single FCC structure without any recrystallization or decomposition up to 400 °C. The grains start to grow around 530 °C, however, some decomposition and precipitation were observed at 500 °C before recrystallization. It was found that co-segregation of Ni and Mn at some grain boundaries and co-segregation Cr and C at other grain boundaries are observed in the sample heat treated at 500 °C. CoFe B2 phase, NiMn FCC phase and M_7C_3 carbide were identified by electron microscopy in samples annealed in the temperature range from 530 to 600 °C. The mechanism of the phase decomposition and nucleation of the precipitates were tackled in Chapter 5. It was proposed that carbides formed at the grain boundaries due to the co-segregations of C and Cr, in similar way as NiMn FCC phase. CoFe B2 phase formation is related to the full FCC grain decomposition.

The mechanical properties of the as-HPT-processed samples and the annealed samples were measured using tensile and microhardness tests as described in Chapter 6. In the samples after 3 turns of HPT (CxN3), the contribution of the conventional strengthening mechanism, such as grain size and dislocation strengthening via Hall-Petch and Taylor relationships, do not explain properly the overall strength of all studied nanocrystalline alloys due to the extremely small grain size and the ultra-high dislocation density. The brittle fracture of the C2-alloy after HPT with 3 turns (C2N3) is mainly due to the high dislocation density and the grain boundary C segregation. In the annealed C2N3 samples, the hardness and yield strength slightly increase after annealing in the temperature range from 200 to 500 °C. This abnormal strengthening may be attributed to the recovery of dislocations, segregation and perhaps formation of ordered structure in FCC matrix. The Hall-Petch relationship is still hardly applicable for the annealed alloys due to the complex factors mentioned above.

7.2 Outlook

Despite a relationship of the microstructure and mechanical properties of the C-alloyed nanocrystalline HEAs have been revealed in the present dissertation, some aspects presented in this work still have not been fully clarified and are worth of a deeper investigation based on further experiments.

In Chapter 4, the proposed C segregation at grain boundaries is assumed based on the concentration fluctuation distance and grain size. However, it is still a challenge to directly observe the segregation because of the small grain size in the C2N3 alloy. Combining TEM and APT measurements would be an option for the determination, with a premise of successful preparing a needle sample with a diameter less than 30 nm. In addition, it was proposed that the source for the C segregation is provided by the dissolution of carbides, which were present in the as-cast alloy. An alloy after high temperature homogenization followed by water quenching is helpful to verify if the C segregation would appear from the interstitial solid solution. In Chapter 5, the annealing experiments were performed with the HPT disc to understand the segregation behaviors, FCC phase decomposition and nucleation of the precipitates. Apart from the conventional experiments, in-situ TEM annealing would be a perfect method to reveal the nature of the segregation and precipitation processes. Besides, chemically ordered CoFe B2 phase can be characterized by atomic resolution EDX. With the help of high precision XRD, the carbon solubility in the FCC solid solution can be analyzed during annealing at each temperature to better understand the source of carbon atoms for the carbide formation. In Chapter 6, mechanical properties of all examined alloys were measured. However, due to the complex microstructures of the annealed alloys, the contributions of the hardening mechanism are still not clear. Further work on the mechanical properties may be helpful to clarify the strengthening mechanism of the annealed samples.

All of these findings will help us to unravel the fundamentals of the mechanical properties and thermal stability of the nanocrystalline FCC HEAs, which could provide guidance for further alloy design, processing and application.

List of Figures

Figure 1.1 Configurational entropies calculated for typical alloys at random state [5]. 2
Figure 1.2 Compilation of yield stress data for several metallic systems [21]. 3
Figure 2.1 Schematic illustration of an ideal monatomic material (on the left) and of HEA (on the right). Colored spheres with different atomic radii indicate individual atomic species [27]. 6
Figure 2.2 The temperature dependence of the 0.2 % offset yield stress of the equiatomic alloys and pure Ni [51]. 9
Figure 2.3 Strength-ductility profiles of various classes of metallic materials including HEAs [56]. 10
Figure 2.4 (a) Tensile engineering stress-strain curves of the fully recrystallized CoCrFeMnNi HEA with different grain sizes. (b) Plots of yield strength against inverse square root of grain sizes for the CoCrFeMnNi[59]. 11
Figure 2.5 Microstructure related parameters dislocation density as a function of engineering strain in MEAs at indicated temperatures [72]. 13
Figure 2.6 (a) Typical bright-field micrograph showing the microstructure of the $(NiCoFeCr)_{92}Al_4Nb_4$ HEA. (b) Dark-field micrograph obtained from the superlattice spot corresponding to the ordered structure. (c) Ion maps of the individual elements from APT [80]. 14
Figure 2.7 Intragranular nanoscale NbC precipitates in the $CoCrFeNiNb_{0.8}C_{0.8}$ HEA: (a) BF-TEM image and (b) HRTEM image showing coherency between the matrix and NbC particle [77] . 15
Figure 2.8 ECC images showing nano-twins in specimens annealed at (a) 650 °C for 3 min, (b) 650 °C for 10 min and (c) 750 °C for 3 min. (d) Relations of the increase of the yield strength with grain size and twin spacing of the annealed specimens and (e) increase of the yield strength due to nanograins, SRX, twins and dislocations of the specimens subjected to tempering and annealing [94]. 17
Figure 2.9 Schematic illustration of HPT processing[106]. 18
Figure 2.10 BSE micrographs in axial direction (deformed at 2 GPa, RT), magnification is the same in all micrographs [108]. 19
Figure 2.11 Schematic illustration of ECAP die including inner angle Φ and outer angle Ψ[109]. 20
Figure 2.12 Schematic illustration of the accumulative roll-bonding (ARB) process [17]. 21
Figure 2.13 Schematic diagram of the HPTE process [112]. 22
Figure 2.14 Schematic illustration of the five grain refinement stages, formed sequentially throughout the microstructural evolution during SPD [126]. 25
Figure 2.15 Schematic illustration of the grain refinement mechanism for the Cu–30 wt. % Zn alloy processed by HPT [149]. 26
Figure 2.16 BSE images of saturation microstructure of Ni99.99 and Ni99.79 at -196 and 400 °C [154]. 28
Figure 2.17 Plots showing the trend of yield stress with grain size for different metals as compared to the conventional Hall–Petch response: (a) copper, (b) iron, (c) nickel and (d) titanium [182]. 30
Figure 2.18 Model of (a) the rotation of nano grains, (b) annihilation of grain boundary, and (c) coalescence of nano grains [182]. 32
Figure 2.19 Various stages in the recovery of a plastically deformed material [206]. 34
Figure 2.20 Boundaries of the single FCC phase field in the carbon-doped $Co_1Cr_xFe_1Mn_1Ni_1$ alloys (subscripts indicate the molar concentrations of the respective elements) depending on the Cr and C concentrations [99]. 36
Figure 3.1 (a) HPT machine and (b) samples demo before and after HPT (black grids indicate 5×5 mm^2). 39
Figure 3.2 Schematic cross-section of two types of differentials a heat flux DSC. (a) heat flux DSC, (b) power compensation DSC [215]. 40
Figure 3.3 Schematic of the SEM and FIB machines, shown in a two-beam configuration [221]. 42

Figure 3.4 The two basic operations of the TEM imaging system involve (a) diffraction mode: projecting the DP onto the viewing screen and (b) image mode: projecting the image onto the screen[226]. 44

Figure 3.5 (a) Ray diagram showing hollow-cone illumination conditions. The direct beam is always off axis but electrons diffracted at the cone angle are always scattered on axis. (b) A BF image of a nanocrystalline Al film. (c) A hollow-cone SAD pattern from the film. Thus, while a single (220) CDF image (d) reveals only a couple of strongly diffracting crystals, a hollow-cone DF image (e) from all the {220} reflections show diffracted intensity from dozens of grains. The scale bar is 500 nm[226]. 45

Figure 3.6 Interaction of an isolated atom with electrons including inelastic scattering and elastic scattering. 46

Figure 3.7 HR-STEM HAADF image of Al2Cu precipitate in Al matrix. 47

Figure 3.8 A TEM sample preparation procedure: from Pt deposition to lift out and finial thin lamella. 48

Figure 3.9 Schematic representation of the field ion microscope [232]. 49

Figure 3.10 Principle of the ATP technique. Atoms at the surface of the specimen are evaporated by field effect and fly towards a detection system [236]. 50

Figure 3.11 Photograph of a LEAP 4000X HR system. 51

Figure 3.12 Step by step procedures of APT tips preparation onto the TEM grid. 51

Figure 3.13 Schematic representation showing cutting position of tensile specimens in HPT-disks and specimens before test. 53

Figure 4.1 (a-c) BES images of the microstructure of the as-cast CoCrFeMnNiCx HEAs: (a) x= 0; (b) x=0.5; (c) x=2; (d) corresponding enlarged region in (c). 55

Figure 4.2 APT reconstruction of the carbide at a grain boundary in the as-cast C2 sample shown in Figure.4.1(d): (a) overview of the reconstruction with Cr, Co, Fe, Ni, Mn and C maps (b) iso-concentration surfaces show areas with element concentration exceeding 36 at. %. 57

Figure 4.3 Microstructure evolution of the C0 alloy during HPT: (a) center position without shear strain; (b) deformation structure with twinning, the equivalent strain ~0.6; (c) the microstructure at the edge of HPT disk, the equivalent strain ~4; (d-f) the EDX elemental maps corresponding to areas shown in (a-c). 58

Figure 4.4 Microstructures and distribution of chemical elements of C2N3 alloy. (a) EDX maps of metallic elements and the selected area in original TEM lamella; (b) HAADF-STEM image of the microstructure of the C2N3 alloy and inserted SAED; (c) a concentration profile created along the white arrow in (a). 59

Figure 4.5 DF-TEM images and corresponding SAED patterns (inserts) of HEAs processed by HPT with 3 turns: (a) C0N3; (b) C0.5N3; (c) C2N3; (d, e) higher magnification BF-TEM images for C0.5N3 and C2N3 alloys, respectively. 60

Figure 4.6 XRD diffraction patterns for the high entropy alloys with different C contents after three turns of HPT. The insert shows enlarged (311) peaks. 61

Figure 4.7 The crystallite size vs. shear strain γ; (b) the dislocation density vs. shear strain γ. 62

Figure 4.8 APT reconstruction the C2N3 alloy at saturation: an overview of the reconstruction with Cr, Co, Fe, Ni, Mn and C maps. 62

Figure 4.9 TEM characterization of CoCrFeMnNiC2 deformed at room (a-c) and cryogenic temperature (d-f). (a) and (d) show the BF-TEM image with inserted selected area diffraction patterns;(b) and (e) are orientation maps evaluated from ACOM and corresponding grain size histogram; (c) and (f) show the HR-TEM image with enlarged area and corresponding FFT. 63

Figure 4.10 APT reconstructions in (a) RT and (b) LNT alloys. Co, Mn, Cr, Ni, Fe, and C elemental distribution were shown separately; the arrows C map (a) indicated the sites of carbon segregation. 65

Figure 4.11 Schematic of microstructure evolution during HPT of: (a) C0 alloy; (b) C2 alloy. 67

Figure 4.12 Linear concentration profiles of C atoms evaluated from the APT measurements of the samples processed by HPT at (a) RT and (b) LNT. 69

Figure 4.13 HRTEM image obtained at grain triple junction in LNT sample. (a) marked grain boundaries of Grain 1 and Grain 2 showing [011] and [001] ZA and corresponding FFTs. (b) FFT from the grain boundaries region. (c) shows the inverse FFT image of (b) filtered with these additional spots. 70

Figure 5.1 DSC heating curve of the C2N3 alloy, a strong exothermic peak on 600 °C and one around ~530 °C. 72

Figure 5.2 BF-TEM images and corresponding SAED of the C2N3 alloy after annealing from 200-600 °C. 73

Figure 5.3 STEM-EELS elemental maps of C2N3 alloy after annealing at 500°C for 1 h. (a) The ADF image of spectrum imaging region and corresponding metallic elements distribution maps; (b) Magnified color mix map of Cr, Ni and Fe with inserted concentration profile crossing a grain along the white arrows displaying the fluctuations of Cr and Ni. 74

Figure 5.4 APT reconstruction of C2N3 sample after annealing at 500 °C for 1h shows segregation of C, Cr and Ni. (a) 6 at. % C iso-surface, 10 at. % Cr iso-surface and 29.8 % Ni iso-surface; The 1-D composition profiles taken along the direction indicated by the purple arrow (b) and the orange arrow (c). 75

Figure 5.5 STEM-EELS elemental maps of C2N3 alloy after annealing at 530°C for 1 h at a low magnification. The dashed line in the Fe and Mn elemental maps indicate the border between DB and IDB. 76

Figure 5.6 STEM-EELS elemental maps of C2N3 alloy after annealing at 530°C for 1 h at high magnification in DB region. (a) STEM spectrum image and elemental distribution maps with a step size of 0.5 nm (b) a concentration profile along the white arrow in the overall map. 78

Figure 5.7 (a) APT 3D reconstruction volume of C2N3 alloy after annealing at 530°C for 1 h in DB region showing inhomogeneous elements distribution; (b) the iso-composition of 55 at. % (C, Cr), 75 at. % (Co, Fe), 90 at. % (Ni, Mn) and 35 at. % Ni; Proxigrams (d-e) created for the NiMn, CoFe and C,Cr iso-surface, respectively. 79

Table 5.1 The chemical compositions of all phases present in the analyzed APT volume in Figure 5.8. 79

Figure 5.9 STEM-EELS elemental maps of C2N3 alloy after annealing at 600°C for 1 h. (a) STEM spectrum image and elemental distribution maps; (b) a concentration profile along the white arrow in Ni map, and white circles indicate position where is a Cr enriched particle. 81

Figure 5.10 Statistics on the precipitates of CoFe B2 phase, NiMn phase and carbides from the C2N3 alloy annealed from 500 to 600 °C. (a) equivalent diameter and (b) the volume fraction of each precipitate. 82

Figure 5.11 HRSTEM images of (a) a CoFe phase, (b) a NiMn phase in C2N3 alloy after annealing at 530 °C for 1 h . (c) HRTEM image of carbide on the FCC grain boundary in C2N3 alloy after annealing at 600 °C for 1 h; (d) is the FFT of (a) indexed with [001] zone axis; (e) is the FFT of (b) indexed with [-110] zone axis based on FCC structure; (f) is the FFT of (c) showing an orientation relationship of (111) FCC // (212) M7C3;(g) and (h) are the CBED of (a) CoFe phase and (b) NiMn phase, respectively; (i) shows the schematic of a chemically ordered NiMn FCT $L1_0$ structure. 83

Figure 5.12 Temperature range of various phases precipitation in CoCrFeMnNi from literatures [172,196,280–284] and our experimental C2N3 alloy. 84

Figure 5.13 A schematic shows the progress of segregation, depletion and nucleation during the annealing process of C2N3 alloy from as-deformed state to the sample annealed at 530 °C for 1 h. 88

Figure 6.1 The variation of Vickers microhardness along the HPT samples' diameter for (a) C2Ny alloys; (b) CxN3 alloys; (c) Hardness evolution of C0 and C2 samples as a function of Von Mises equivalent strain, the hardness evolution of C0.5 alloy is not shown here because of the plots overlapping, but it has the same tendency; (d) hardness of C2N3 alloy processed by HPT at RT (293 K) and at cryogenic temperature (77 K). 91

Figure 6.2 The tensile stress-strain curves of the studied alloys: (a) as-cast state; (b) CxN3 alloys. 92

Figure 6.3 Fracture morphology of tensile samples of C0N3 (a), C0.5N3 (b) and C2N3 (c) alloys. Scale bars indicate 1 μm. 93

Figure 6.4 Mechanical properties of nanocrystalline 2 at. % C-HEAs after annealing process from 200 to 600 °C: (a) dependence of Vickers hardness on heat treatments temperatures; (b) engineering strain-stress curves. 94
Figure 6.5 Fracture surface morphology of the samples annealed at (a) 200 °C, (b) 500 °C, (c) 530 °C, (d) 560 °C and (e) 600 °C. 95
Figure 6.6 The estimated contribution of GBs and dislocation strengthening to the yield strength and corresponding measured values. 98
Figure 6.7 The dependence of hardness, yield strength and precipitates fraction via anneal temperature and grain size. 102

List of Tables

Table 2.1 Common slip systems in FCC and BCC structures [111]. 22
Table 2.2 Effect of different parameters on the onset strain of saturation and the size of the structural elements, grain size, in the saturation region [154]. 28
Table 3.1 Chemical composition of the as-cast alloys (at. %). 38
Table 4.1 The composition and volume fraction of DB and IDB regions 59
Table 4.2 The grain/crystallite sizes determined by STEM/CMWP method, the dislocation density ρ, the lattice parameter a. 61
Table 5.1 The chemical compositions of all phases present in the analyzed APT volume. 79
Table 6.1 Mechanical properties of the as-casted and CxN3 alloys: yield strength (YS), ultimate tensile strength (UTS), uniform strain (ε_u), strain at fracture (ε_f) and Vickers hardness. 92
Table 6.2 Mechanical properties of annealed C2 alloys: YS, fracture strain (ε_f) and Vickers hardness 94

List of abbreviations

ACOM	Automated crystal orientation mapping
ADF	Annular dark-field
APT	Atom Probe Tomography
ARB	Accumulative rill-bonding
BSE	Backscattered electrons
BF-TEM	Bright field TEM
CMWP	Convolutional Multiple Whole Profile
CBED	Converged beam electron diffraction
DB	Dendritic band
DF-TEM	Dark field TEM
DSC	Differential scanning calorimetry
ECAP	Equal-channel angular pressing
EDX	Energy-dispersive X-ray spectroscopy
EELS	Electron energy-loss spectroscopy
FCC	Face centered cubic
FCT	Face-centered tetragonal
FFT	Fast Fourier transform
FIB	Focused ion beam
HAADF	High-angle annular dark-field
HPT	High-pressure torsion
HPTE	High Pressure Torsion Extrusion
HRTEM	High-resolution transmission electron microscopy
IDB	Interdendritic band
LEAP	Local Electrode Atom Probe
LNT	Liquid nitrogen temperature

MEA	Medium entropy alloy
RT	Room temperature
SAED	Selected Area Electron Diffraction
SEM	Scanning Electron Microscopy
SFE	Stacking fault energy
SPD	Severe plastic deformation
STEM	Scanning transmission electron microscopy
TEM	Transmission electron microscopy
UFG	Ultrafine-grained
UTS	Ultimate tensile strength
XRD	X-Ray Diffraction
YS	Yield strength

References

[1] P.A. Cohen, Speaking to History: The Story of King Goujian in Twentieth-Century China, Univ of California Press, 2008.

[2] J.W. Yeh, S.K. Chen, S.J. Lin, J.Y. Gan, T.S. Chin, T.T. Shun, C.H. Tsau, S.Y. Chang, Adv. Eng. Mater. 6 (2004) 299–303.

[3] R. A. Swalin, In Thermodynamics of Solids, 2nd ed., Wiley, 1991.

[4] B.S. Murty, High Entropy Alloys, n.d.

[5] J.-W. Yeh, JOM 65 (2013) 1759–1771.

[6] S. Gorsse, D.B. Miracle, O.N. Senkov, Acta Mater. 135 (2017) 177–187.

[7] B. Cantor, I.T.H. Chang, P. Knight, A.J.B. Vincent, Mater. Sci. Eng. A 375–377 (2004) 213–218.

[8] G. Laplanche, A. Kostka, O.M. Horst, G. Eggeler, E.P. George, Acta Mater. 118 (2016) 152–163.

[9] F. Otto, A. Dlouhý, C. Somsen, H. Bei, G. Eggeler, E.P. George, Acta Mater. 61 (2013) 5743–5755.

[10] A. Gali, E.P. George, Intermetallics 39 (2013) 74–78.

[11] W. Li, D. Xie, D. Li, Y. Zhang, Y. Gao, P.K. Liaw, Prog. Mater. Sci. 118 (2021) 100777.

[12] M.V. Klimova, A.O. Semenyuk, D.G. Shaysultanov, G.A. Salishchev, S.V. Zherebtsov, N.D. Stepanov, J. Alloys Compd. 811 (2019) 152000.

[13] J. Chen, Z. Yao, X. Wang, Y. Lu, X. Wang, Y. Liu, X. Fan, Mater. Chem. Phys. 210 (2018) 136–145.

[14] Z. Wu, C.M. Parish, H. Bei, J. Alloys Compd. 647 (2015) 815–822.

[15] P.W. Bridgman, Phys. Rev. 48 (1935) 825.

[16] V.M. Segal, Mater. Sci. Eng. A 271 (1999) 322–333.

[17] Y. Saito, H. Utsunomiya, N. Tsuji, T. Sakai, Acta Mater. 47 (1999) 579–583.

[18] R.Z. Valiev, N.A. Krasilnikov, N.K. Tsenev, Mater. Sci. Eng. A 137 (1991) 35–40.

[19] E.O. Hall, Proc. Phys. Soc. Sect. B 64 (1951) 742–747.

[20] N.J. Petch, J. Iron Steel Inst. 174 (1953) 25–28.

[21] R.A. Masumura, P.M. Hazzledine, C.S. Pande, Acta Mater. 46 (1998) 4527–4534.

[22] J. Chen, X. Jiang, H. Sun, Z. Shao, Y. Fang, R. Shu, Nanotechnol. Rev. 10 (2021) 1116–1139.

[23] D.B. Miracle, J.D. Miller, O.N. Senkov, C. Woodward, M.D. Uchic, J. Tiley, Entropy 16 (2014) 494–525.

[24] Q. Wang, Y. Lu, Q. Yu, Z. Zhang, Sci. Rep. 8 (2018) 1–7.

[25] Y. Yang, T. Chen, L. Tan, J.D. Poplawsky, K. An, Y. Wang, G.D. Samolyuk, K. Littrell, A.R. Lupini, A. Borisevich, E.P. George, Nature 595 (2021) 245–249.

[26] F. Otto, Y. Yang, H. Bei, E.P. George, Acta Mater. 61 (2013) 2628–2638.

[27] L.R. Owen, N.G. Jones, J. Mater. Res. 33 (2018) 2954–2969.

[28] J.W. Yeh, Jom 65 (2013) 1759–1771.

[29] J.W. Yeh, S.Y. Chang, Y. Der Hong, S.K. Chen, S.J. Lin, Mater. Chem. Phys. 103 (2007) 41–46.

[30] E.J. Pickering, N.G. Jones, Int. Mater. Rev. 61 (2016) 183–202.

[31] L.R. Owen, E.J. Pickering, H.Y. Playford, H.J. Stone, M.G. Tucker, N.G. Jones, Acta Mater. 122 (2017)

11–18.

[32] Y. Tong, G. Velisa, T. Yang, K. Jin, C. Lu, H. Bei, J.Y.P. Ko, D.C. Pagan, R. Huang, Y. Zhang, L. Wang, F.X. Zhang, ArXiv (2017).

[33] A. Mehta, Y.H. Sohn, Diffus. Found. 29 (2021) 75–93.

[34] K.Y. Tsai, M.H. Tsai, J.W. Yeh, Acta Mater. 61 (2013) 4887–4897.

[35] T.T. Shun, C.H. Hung, C.F. Lee, J. Alloys Compd. 493 (2010) 105–109.

[36] C.Y. Hsu, C.C. Juan, W.R. Wang, T.S. Sheu, J.W. Yeh, S.K. Chen, Mater. Sci. Eng. A 528 (2011) 3581–3588.

[37] A. Paul, Scr. Mater. 135 (2017) 153–157.

[38] A. Mehta, Y. Sohn, Mater. Res. Lett. 9 (2021) 239–246.

[39] M. Vaidya, K.G. Pradeep, B.S. Murty, G. Wilde, S. V. Divinski, Acta Mater. 146 (2018) 211–224.

[40] M. Vaidya, S. Trubel, B.S. Murty, G. Wilde, S. V. Divinski, J. Alloys Compd. 688 (2016) 994–1001.

[41] J. Kottke, M. Laurent-Brocq, A. Fareed, D. Gaertner, L. Perrière, Ł. Rogal, S. V. Divinski, G. Wilde, Scr. Mater. 159 (2019) 94–98.

[42] J. Dąbrowa, W. Kucza, G. Cieślak, T. Kulik, M. Danielewski, J.W. Yeh, J. Alloys Compd. 674 (2016) 455–462.

[43] Q. Li, W. Chen, J. Zhong, L. Zhang, Q. Chen, Z.K. Liu, Metals (Basel). 8 (2018).

[44] K. Jin, C. Zhang, F. Zhang, H. Bei, Mater. Res. Lett. 6 (2018) 293–299.

[45] J. Dąbrowa, M. Zajusz, W. Kucza, G. Cieślak, K. Berent, T. Czeppe, T. Kulik, M. Danielewski, J. Alloys Compd. 783 (2019) 193–207.

[46] S. V. Divinski, A. V. Pokoev, N. Esakkiraja, A. Paul, Diffus. Found. 17 (2018) 69–104.

[47] S. Ranganathan, Curr. Sci. 85 (2003) 1404–1406.

[48] B.X. Cao, C. Wang, T. Yang, C.T. Liu, Scr. Mater. 187 (2020) 250–255.

[49] P.F. Koshelev, Strength Mater. 3 (1971) 286–291.

[50] X. Bai, W. Fang, R. Chang, H. Yu, X. Zhang, F. Yin, Mater. Sci. Eng. A 767 (2019) 138403.

[51] Z. Wu, H. Bei, G.M. Pharr, E.P. George, Acta Mater. 81 (2014) 428–441.

[52] A. Gali, E.P. George, Intermetallics 39 (2013) 74–78.

[53] N.L. Okamoto, S. Fujimoto, Y. Kambara, M. Kawamura, Z.M.T. Chen, H. Matsunoshita, K. Tanaka, H. Inui, E.P. George, Sci. Rep. 6 (2016) 1–10.

[54] Z. Lei, X. Liu, Y. Wu, H. Wang, S. Jiang, S. Wang, X. Hui, Y. Wu, B. Gault, P. Kontis, D. Raabe, L. Gu, Q. Zhang, H. Chen, H. Wang, J. Liu, K. An, Q. Zeng, T.G. Nieh, Z. Lu, Nature 563 (2018) 546–550.

[55] R.L. Fleischer, Acta Metall. 15 (1967) 1513–1519.

[56] Z. Li, C.C. Tasan, H. Springer, B. Gault, D. Raabe, Sci. Rep. 7 (2017) 1–7.

[57] N.D. Stepanov, N.Y. Yurchenko, M.A. Tikhonovsky, G.A. Salishchev, J. Alloys Compd. 687 (2016) 59–71.

[58] W.H. Liu, Y. Wu, J.Y. He, T.G. Nieh, Z.P. Lu, Scr. Mater. 68 (2013) 526–529.

[59] S.J. Sun, Y.Z. Tian, H.R. Lin, X.G. Dong, Y.H. Wang, Z.J. Zhang, Z.F. Zhang, Mater. Des. 133 (2017) 122–127.

[60] S. Yoshida, T. Bhattacharjee, Y. Bai, N. Tsuji, Scr. Mater. 134 (2017) 33–36.

[61] Z.C. Cordero, B.E. Knight, C.A. Schuh, Int. Mater. Rev. 61 (2016) 495–512.

[62] N. Hansen, Scr. Mater. 51 (2004) 801–806.

[63] B. Kang, J. Lee, H.J. Ryu, S.H. Hong, J. Alloys Compd. 767 (2018) 1012–1021.

[64] D. Wu, J. Zhang, J.C. Huang, H. Bei, T.G. Nieh, Scr. Mater. 68 (2013) 118–121.

[65] Y.C. Huang, C.H. Su, S.K. Wu, C. Lin, Entropy 21 (2019).

[66] Y.H. Zhao, X.Z. Liao, Z. Jin, R.Z. Valiev, Y.T. Zhu, Acta Mater. 52 (2004) 4589–4599.

[67] R.S. Ganji, P. Sai Karthik, K. Bhanu Sankara Rao, K. V. Rajulapati, Acta Mater. 125 (2017) 58–68.

[68] J.Y. He, H. Wang, H.L. Huang, X.D. Xu, M.W. Chen, Y. Wu, X.J. Liu, T.G. Nieh, K. An, Z.P. Lu, Acta Mater. 102 (2016) 187–196.

[69] G.K. Williamson, R.E. Smallman, Philos. Mag. A J. Theor. Exp. Appl. Phys. 1 (1956) 34–46.

[70] G.K. Williamson, W.H. Hall, Acta Metall. 1 (1953) 22–31.

[71] R.K. Ham, Philos. Mag. A J. Theor. Exp. Appl. Phys. 6 (1961) 1183–1184.

[72] W. Woo, M. Naeem, J.S. Jeong, C.M. Lee, S. Harjo, T. Kawasaki, H. He, X.L. Wang, Mater. Sci. Eng. A 781 (2020) 139224.

[73] P. Thirathipviwat, G. Song, J. Jayaraj, J. Bednarcik, H. Wendrock, T. Gemming, J. Freudenberger, K. Nielsch, J. Han, J. Alloys Compd. 790 (2019) 266–273.

[74] Z. Fu, W. Chen, H. Wen, D. Zhang, Z. Chen, B. Zheng, Y. Zhou, E.J. Lavernia, Acta Mater. 107 (2016) 59–71.

[75] G.E. Dieter, D. Bacon, Mechanical Metallurgy, McGraw-hill New York, 1976.

[76] I. Moravcik, V. Hornik, P. Minárik, L. Li, I. Dlouhy, M. Janovska, D. Raabe, Z. Li, Mater. Sci. Eng. A 781 (2020) 1–14.

[77] N. Gao, D.H. Lu, Y.Y. Zhao, X.W. Liu, G.H. Liu, Y. Wu, G. Liu, Z.T. Fan, Z.P. Lu, E.P. George, J. Alloys Compd. 792 (2019) 1028–1035.

[78] T. Yang, Y.L. Zhao, J.H. Luan, B. Han, J. Wei, J.J. Kai, C.T. Liu, Scr. Mater. 164 (2019) 30–35.

[79] L. Fan, T. Yang, J.H. Luan, Z.B. Jiao, J. Alloys Compd. 832 (2020) 154903.

[80] Y.L. Zhao, T. Yang, Y.R. Li, L. Fan, B. Han, Z.B. Jiao, D. Chen, C.T. Liu, J.J. Kai, Acta Mater. 188 (2020) 517–527.

[81] W. Lu, X. Luo, Y. Yang, W. Le, B. Huang, P. Li, J. Alloys Compd. 833 (2020).

[82] S. Dasari, A. Jagetia, Y.J. Chang, V. Soni, B. Gwalani, S. Gorsse, A.C. Yeh, R. Banerjee, J. Alloys Compd. 830 (2020) 154707.

[83] L. Zhang, X. Huo, A. Wang, X. Du, L. Zhang, W. Li, N. Zou, G. Wan, G. Duan, B. Wu, Intermetallics 122 (2020) 106813.

[84] J.W. Bae, J.M. Park, J. Moon, W.M. Choi, B.J. Lee, H.S. Kim, J. Alloys Compd. 781 (2019) 75–83.

[85] D.N. Seidman, E.A. Marquis, D.C. Dunand, Acta Mater. 50 (2002) 4021–4035.

[86] K. Ma, H. Wen, T. Hu, T.D. Topping, D. Isheim, D.N. Seidman, E.J. Lavernia, J.M. Schoenung, Acta Mater. 62 (2014) 141–155.

[87] H. Wen, T.D. Topping, D. Isheim, D.N. Seidman, E.J. Lavernia, Acta Mater. 61 (2013) 2769–2782.

[88] Y.F. Shen, L. Lu, Q.H. Lu, Z.H. Jin, K. Lu, Scr. Mater. 52 (2005) 989–994.

[89] J.W. Christian, S. Mahajan, Prog. Mater. Sci. 39 (1995) 1–157.

[90] O. Bouaziz, S. Allain, C. Scott, Scr. Mater. 58 (2008) 484–487.

[91] L. Remy, Acta Metall. 26 (1978) 443–451.

[92] O. Bouaziz, N. Guelton, Mater. Sci. Eng. A 319–321 (2001) 246–249.

[93] I. Karaman, H. Sehitoglu, A.J. Beaudoev, Y.I. Chumlyakov, H.J. Maier, C.N. Tomé, Acta Mater. 48 (2000) 2031–2047.

[94] J. Su, D. Raabe, Z. Li, Acta Mater. 163 (2019) 40–54.

[95] M. Dao, L. Lu, Y.F. Shen, S. Suresh, Acta Mater. 54 (2006) 5421–5432.

[96] E.B. Tadmor, N. Bernstein, J. Mech. Phys. Solids 52 (2004) 2507–2519.

[97] G. Laplanche, A. Kostka, C. Reinhart, J. Hunfeld, G. Eggeler, E.P. George, Acta Mater. 128 (2017) 292–303.

[98] A.J. Zaddach, C. Niu, C.C. Koch, D.L. Irving, JOM 65 (2013) 1780–1789.

[99] N. Stepanov, M. Tikhonovsky, N. Yurchenko, D. Zyabkin, M. Klimova, S. Zherebtsov, A. Efimov, G. Salishchev, Intermetallics 59 (2015) 8–17.

[100] E. El-Danaf, S.R. Kalidindi, R.D. Doherty, Metall. Mater. Trans. A 30 (1999) 1223–1233.

[101] K. Edalati, A. Bachmaier, V.A. Beloshenko, Y. Beygelzimer, V.D. Blank, W.J. Botta, K. Bryła, J. Čížek, S. Divinski, N.A. Enikeev, Y. Estrin, G. Faraji, R.B. Figueiredo, M. Fuji, T. Furuta, T. Grosdidier, J. Gubicza, A. Hohenwarter, Z. Horita, J. Huot, Y. Ikoma, M. Janeček, M. Kawasaki, P. Král, S. Kuramoto, T.G. Langdon, D.R. Leiva, V.I. Levitas, A. Mazilkin, M. Mito, H. Miyamoto, T. Nishizaki, R. Pippan, V. V. Popov, E.N. Popova, G. Purcek, O. Renk, Á. Révész, X. Sauvage, V. Sklenicka, W. Skrotzki, B.B. Straumal, S. Suwas, L.S. Toth, N. Tsuji, R.Z. Valiev, G. Wilde, M.J. Zehetbauer, X. Zhu, Mater. Res. Lett. 10 (2022) 163–256.

[102] V.M. Segal, V.I. Reznikov, A.E. Dobryshevshiy, V.I. Kopylov, Russ. Metall. (1981) 99–105.

[103] Y. Saito, N. Tsuji, H. Utsunomiya, T. Sakai, R.G. Hong, Scr. Mater. 39 (1998) 1221–1227.

[104] P.W. Bridgman, Studies in Large Plastic Flow and Fracture, Harvard University Press, 2013.

[105] A.P. Zhilyaev, G. V. Nurislamova, B.K. Kim, M.D. Baró, J.A. Szpunar, T.G. Langdon, Acta Mater. 51 (2003) 753–765.

[106] R. Wadsack, R. Pippan, B. Schedler, Fusion Eng. Des. 66–68 (2003) 265–269.

[107] V.D. Blank, M.Y. Popov, B.A. Kulnitskiy, Mater. Trans. 60 (2019) 1500–1505.

[108] T. Hebesberger, H.P. Stüwe, A. Vorhauer, F. Wetscher, R. Pippan, Acta Mater. 53 (2005) 393–402.

[109] S. Attarilar, M.T. Salehi, K.J. Al-Fadhalah, F. Djavanroodi, M. Mozafari, PLoS One 14 (2019) 1–18.

[110] Y. Iwahashi, Z. Horita, M. Nemoto, J. Wang, T.G. Langdon, Scr. Mater. 35 (1996).

[111] W. Skrotzki, Mater. Trans. 60 (2019) 1331–1343.

[112] Y. Ivanisenko, R. Kulagin, V. Fedorov, A. Mazilkin, T. Scherer, B. Baretzky, H. Hahn, Mater. Sci. Eng. A 664 (2016) 247–256.

[113] J.P. Hirth, J. Lothe, T. Mura, J. Appl. Mech. 50 (1983) 476.

[114] Y. Estrin, A. Vinogradov, Acta Mater. 61 (2013) 782–817.

[115] U.F. Kocks, H. Mecking, Prog. Mater. Sci. 48 (2003) 171–273.

[116] H. Mughrabi, Rev. Phys. Appliquée 23 (1988) 367–379.

[117] W.D. Nix, J.C. Gibeling, D.A. Hughes, Metall. Trans. A 16 (1985) 2215–2226.

[118] H. Mughrabi, Acta Metall. 31 (1983) 1367–1379.

[119] F.B. Prinz, A.S. Argon, Acta Metall. 32 (1984) 1021–1028.

[120] L.S. To´th, A. Molinari, Y. Estrin, J. Eng. Mater. Technol. 124 (2001) 71–77.

[121] M. Zehetbauer, V. Seumer, Acta Metall. Mater. 41 (1993) 577–588.

[122] Y. Estrin, L.S. Tóth, A. Molinari, Y. Bréchet, Acta Mater. 46 (1998) 5509–5522.

[123] B. Bay, N. Hansen, D. Kuhlmann-Wilsdorf, Mater. Sci. Eng. A 113 (1989) 385–397.

[124] D. Kuhlmann-Wilsdorf, N. Hansen, Scr. Metall. Mater. 25 (1991) 1557–1562.

[125] B. Bay, N. Hansen, D.A. Hughes, D. Kuhlmann-Wilsdorf, Acta Metall. Mater. 40 (1992) 205–219.

[126] Y. Cao, S. Ni, X. Liao, M. Song, Y. Zhu, Mater. Sci. Eng. R Reports 133 (2018) 1–59.

[127] B. N⊘st, Philos. Mag. A J. Theor. Exp. Appl. Phys. 11 (1965) 183–184.

[128] S. Howe, C. Elbaum, Philos. Mag. A J. Theor. Exp. Appl. Phys. 6 (1961) 1227–1240.

[129] Q. Liu, N. Hansen, Scr. Metall. Mater. 32 (1995) 1289–1295.

[130] N. Hansen, C.Y. Barlow, Phys. Metall. Fifth Ed. 1 (2014) 1681–1764.

[131] D. Kuhlmann-Wilsdorf, Scr. Mater. 36 (1997) 173–181.

[132] A. Godfrey, Q. Liu, Scr. Mater. 60 (2009) 1050–1055.

[133] X. Huang, G. Winther, Philos. Mag. 87 (2007) 5189–5214.

[134] G. Winther, X. Huang, Philos. Mag. 87 (2007) 5215–5235.

[135] D.A. Hughes, N. Hansen, Acta Mater. 45 (1997) 3871–3886.

[136] D.A. Hughes, N. Hansen, Scr. Metall. Mater. 33 (1995) 315–321.

[137] C.S. Hong, N.R. Tao, X. Huang, K. Lu, Acta Mater. 58 (2010) 3103–3116.

[138] X.H. An, S.D. Wu, Z.F. Zhang, Mater. Sci. Forum 667–669 (2011) 379–384.

[139] H.W. Zhang, Z.K. Hei, G. Liu, J. Lu, K. Lu, Acta Mater. 51 (2003) 1871–1881.

[140] C. Zener, J.H. Hollomon, J. Appl. Phys. 15 (1944) 22–32.

[141] N.R. Tao, K. Lu, Scr. Mater. 60 (2009) 1039–1043.

[142] X.H. An, S.D. Wu, Z.G. Wang, Z.F. Zhang, Prog. Mater. Sci. 101 (2019) 1–45.

[143] F. Huang, N.R. Tao, K. Lu, J. Mater. Sci. Technol. 27 (2011) 628–632.

[144] F. Huang, N.R. Tao, J. Mater. Sci. Technol. 27 (2011) 1–7.

[145] Z.P. Luo, H.W. Zhang, N. Hansen, K. Lu, Acta Mater. 60 (2012) 1322–1333.

[146] Y.S. Li, Y. Zhang, N.R. Tao, K. Lu, Acta Mater. 57 (2009) 761–772.

[147] Y. Zhang, N.R. Tao, K. Lu, Scr. Mater. 60 (2009) 211–213.

[148] Y. Zhang, N.R. Tao, K. Lu, Acta Mater. 59 (2011) 6048–6058.

[149] Y.B. Wang, X.Z. Liao, Y.H. Zhao, E.J. Lavernia, S.P. Ringer, Z. Horita, T.G. Langdon, Y.T. Zhu, Mater. Sci. Eng. A 527 (2010) 4959–4966.

[150] F. Wetscher, A. Vorhauer, R. Pippan, Mater. Sci. Eng. A 410–411 (2005) 213–216.

[151] A.P. Zhilyaev, G. V. Nurislamova, B.K. Kim, M.D. Baró, J.A. Szpunar, T.G. Langdon, Acta Mater. 51 (2003) 753–765.

[152] A. Mishra, B.K. Kad, F. Gregori, M.A. Meyers, Acta Mater. 55 (2007) 13–28.

[153] R. Pippan, S. Scheriau, A. Taylor, M. Hafok, A. Hohenwarter, A. Bachmaier, Annu. Rev. Mater. Res. 40 (2010) 319–343.

[154] G.B. Rathmayr, R. Pippan, Acta Mater. 59 (2011) 7228–7240.

[155] Y.Y. Wang, P.L. Sun, P.W. Kao, C.P. Chang, Scr. Mater. 50 (2004) 613–617.

[156] R. Pippan, F. Wetscher, M. Hafok, A. Vorhauer, I. Sabirov, Adv. Eng. Mater. 8 (2006) 1046–1056.

[157] R.B. Godiksen, Z.T. Trautt, M. Upmanyu, J. Schiøtz, D.J. Jensen, S. Schmidt, Acta Mater. 55 (2007) 6383–6391.

[158] E.I. Galindo-Nava, C.M.F. Rae, Mater. Sci. Eng. A 636 (2015) 434–445.

[159] U. Andrade, M.A. Meyers, K.S. Vecchio, A.H. Chokshi, Acta Metall. Mater. 42 (1994) 3183–3195.

[160] E.I. Galindo-Nava, P.E.J. Rivera-Díaz-del-Castillo, Mater. Sci. Eng. A 558 (2012) 641–648.

[161] K. Edalati, J.M. Cubero-Sesin, A. Alhamidi, I.F. Mohamed, Z. Horita, Mater. Sci. Eng. A 613 (2014) 103–110.

[162] F. Otto, N.L. Hanold, E.P. George, Intermetallics 54 (2014) 39–48.

[163] G. Laplanche, O. Horst, F. Otto, G. Eggeler, E.P. George, J. Alloys Compd. 647 (2015) 548–557.

[164] W. Abuzaid, H. Sehitoglu, Mater. Charact. 129 (2017) 288–299.

[165] J.W. Won, S. Lee, S.H. Park, M. Kang, K.R. Lim, C.H. Park, Y.S. Na, J. Alloys Compd. 742 (2018) 290–295.

[166] X. Ma, J. Chen, X. Wang, Y. Xu, Y. Xue, J. Alloys Compd. 795 (2019) 45–53.

[167] Z.H. Han, S. Liang, J. Yang, R. Wei, C.J. Zhang, Mater. Charact. 145 (2018) 619–626.

[168] H. Kwon, P. Asghari-Rad, J.M. Park, P. Sathiyamoorthi, J.W. Bae, J. Moon, A. Zargaran, Y.T. Choi, S. Son, H.S. Kim, Intermetallics (2021).

[169] W. Skrotzki, A. Pukenas, E. Odor, B. Joni, T. Ungar, B. Völker, A. Hohenwarter, R. Pippan, E.P. George, Crystals 10 (2020).

[170] J. Gubicza, P.T. Hung, M. Kawasaki, J.K. Han, Y. Zhao, Y. Xue, J.L. Lábár, Mater. Charact. 154 (2019) 304–314.

[171] H. Shahmir, T. Mousavi, J. He, Z. Lu, M. Kawasaki, T.G. Langdon, Mater. Sci. Eng. A 705 (2017) 411–419.

[172] Q. Tang, Y. Huang, H. Cheng, X. Liao, T.G. Langdon, P. Dai, Mater. Des. 105 (2016) 381–385.

[173] H. Shahmir, J. He, Z. Lu, M. Kawasaki, T.G. Langdon, Mater. Sci. Eng. A 676 (2016) 294–303.

[174] B. Schuh, F. Mendez-Martin, B. Völker, E.P. George, H. Clemens, R. Pippan, A. Hohenwarter, Acta Mater. 96 (2015) 258–268.

[175] Q.H. Tang, Y. Huang, Y.Y. Huang, X.Z. Liao, T.G. Langdon, P.Q. Dai, Mater. Lett. 151 (2015) 126–129.

[176] V.H. Hammond, M.A. Atwater, K.A. Darling, H.Q. Nguyen, L.J. Kecskes, Jom 66 (2014) 2021–2029.

[177] A.H. Chokshi, A. Rosen, J. Karch, H. Gleiter, Scr. Metall. 23 (1989) 1679–1683.

[178] K. Lu, M.L. Sui, in: Scr. Met. Mater, Citeseer, 1993.

[179] H.W. Song, S.R. Guo, Z.Q. Hu, Nanostructured Mater. 11 (1999) 203–210.

[180] D.A. Konstantinidis, E.C. Aifantis, Nanostructured Mater. 10 (1998) 1111–1118.

[181] H. Conrad, J. Narayan, Scr. Mater. 42 (2000) 1025–1030.

[182] M.A. Meyers, A. Mishra, D.J. Benson, Prog. Mater. Sci. 51 (2006) 427–556.

[183] G.D. Hughes, S.D. Smith, C.S. Pande, H.R. Johnson, R.W. Armstrong, Scr. Metall. 20 (1986) 93–97.

[184] C.S. Pande, R.A. Masumura, R.W. Armstrong, Nanostructured Mater. 2 (1993) 323–331.

[185] T.G. Nieh, J. Wadsworth, Scr. Metall. Mater. 25 (1991) 955–958.

[186] A. Ball, M.M. Hutchison, Met. Sci. J. 3 (1969) 1–7.

[187] H. Hahn, P. Mondal, K.A. Padmanabhan, Nanostructured Mater. 9 (1997) 603–606.

[188] H.S. Kim, Y. Estrin, M.B. Bush, Acta Mater. 48 (2000) 493–504.

[189] H. Van Swygenhoven, P.M. Derlet, A. Hasnaoui, Adv. Eng. Mater. 5 (2003) 345–350.

[190] Y. Wang, M. Chen, F. Zhou, E. Ma, Nature 419 (2002) 912–915.

[191] D. Jia, K.T. Ramesh, E. Ma, Scr. Mater. 42 (1999) 73–78.

[192] D. Jia, Y.M. Wang, K.T. Ramesh, E. Ma, Y.T. Zhu, R.Z. Valiev, Appl. Phys. Lett. 79 (2001) 611–613.

[193] M. Murayama, J.M. Howe, H. Hidaka, S. Takaki, Science (80-.). 295 (2002) 2433–2435.

[194] Q. Wei, L. Kecskes, T. Jiao, K.T. Hartwig, K.T. Ramesh, E. Ma, Acta Mater. 52 (2004) 1859–1869.

[195] M.A. Meyers, O. Vöhringer, V.A. Lubarda, Acta Mater. 49 (2001) 4025–4039.

[196] A. Hasnaoui, P.M. Derlet, H. Van Swygenhoven, Acta Mater. 52 (2004) 2251–2258.

[197] A. Frøseth, H. Van Swygenhoven, P.M. Derlet, Acta Mater. 52 (2004) 2259–2268.

[198] F. Otto, A. Dlouhý, K.G. Pradeep, M. Kuběnová, D. Raabe, G. Eggeler, E.P. George, Acta Mater. 112 (2016) 40–52.

[199] A. Hohenwarter, M. Faller, B. Rashkova, R. Pippan, Philos. Mag. Lett. 94 (2014) 342–350.

[200] B.B. Straumal, B. Baretzky, A.A. Mazilkin, F. Phillipp, O.A. Kogtenkova, M.N. Volkov, R.Z. Valiev, Acta Mater. 52 (2004) 4469–4478.

[201] L.S. Mantha, B.E. MacDonald, X. Mu, A. Mazilkin, J. Ivanisenko, H. Hahn, E.J. Lavernia, S. Katnagallu, C. Kübel, Acta Mater. 220 (2021) 117281.

[202] L. Li, Z. Li, A. Kwiatkowski da Silva, Z. Peng, H. Zhao, B. Gault, D. Raabe, Acta Mater. 178 (2019) 1–9.

[203] H. Gleiter, Acta Mater. 48 (2000) 1–29.

[204] C.C. Koch, R.O. Scattergood, K.A. Darling, J.E. Semones, J. Mater. Sci. 43 (2008) 7264–7272.

[205] H.R. Peng, M.M. Gong, Y.Z. Chen, F. Liu, Int. Mater. Rev. 62 (2017) 303–333.

[206] J. Humphreys, G.S. Rohrer, A. Rollett, Recovery After Deformation, 2017.

[207] L.B. Chen, R. Wei, K. Tang, J. Zhang, F. Jiang, L. He, J. Sun, Mater. Sci. Eng. A 716 (2018) 150–156.

[208] A. Bachmaier, R. Pippan, O. Renk, Adv. Eng. Mater. 22 (2020).

[209] A. Hohenwarter, M.W. Kapp, B. Völker, O. Renk, R. Pippan, IOP Conf. Ser. Mater. Sci. Eng. 219 (2017) 12003.

[210] Y. Ivanisenko, X. Sauvage, A. Mazilkin, A. Kilmametov, J.A. Beach, B.B. Straumal, Adv. Eng. Mater. 20 (2018) 1–6.

[211] P. Sathiyamoorthi, J. Basu, S. Kashyap, K.G. Pradeep, R.S. Kottada, Mater. Des. 134 (2017) 426–433.

[212] X. Huang, N. Hansen, N. Tsuji, Science (80-.). 312 (2006) 249–251.

[213] O.A. Lukianova, Z. Rao, V. Kulitckii, Z. Li, G. Wilde, S. V. Divinski, Scr. Mater. 188 (2020) 264–268.

[214] K.E. Van Holde, W.C. Johnson, P.S. Ho, (2006).

[215] N. Gao, M.J. Starink, T.G. Langdon, Mater. Sci. Technol. 25 (2009) 687–698.

[216] W.H. Bragg, W.L. Bragg, Proc. R. Soc. London. Ser. A, Contain. Pap. a Math. Phys. Character 88 (1913) 428–438.

[217] H.M. Rietveld, J. Appl. Crystallogr. 2 (1969) 65–71.

[218] G. Ribárik, J. Gubicza, T. Ungár, Mater. Sci. Eng. A 387–389 (2004) 343–347.

[219] J.I. Goldstein, D.E. Newbury, J.R. Michael, N.W.M. Ritchie, J.H.J. Scott, D.C. Joy, Scanning Electron Microscopy and X-Ray Microanalysis, Springer, 2017.

[220] T.L. Burnett, R. Kelley, B. Winiarski, L. Contreras, M. Daly, A. Gholinia, M.G. Burke, P.J. Withers, Ultramicroscopy 161 (2016) 119–129.

[221] N. Yao, Focused Ion Beam Systems: Basics and Applications, Cambridge University Press, 2007.

[222] M. Knoll, E. Ruska, Zeitschrift Für Phys. 78 (1932) 318–339.

[223] J.C. Russ, X-Ray Spectrom. 2 (1973) 11–14.

[224] R.M. Henkelman, F.P. Ottensmeyer, J. Microsc. 102 (1974) 79–94.

[225] M. Haider, S. Uhlemann, E. Schwan, H. Rose, B. Kabius, K. Urban, Nature 392 (1998) 768–769.

[226] D.B. Williams, C.B. Carter, in: D.B. Williams, C.B. Carter (Eds.), Transm. Electron Microsc. A Textb. Mater. Sci., Springer US, Boston, MA, 2009, pp. 1–760.

[227] D.B. Williams, C.B. Carter, in: D.B. Williams, C.B. Carter (Eds.), Springer US, Boston, MA, 2009, pp. 53–71.

[228] E.W. Müller, Zeitschrift Für Phys. 106 (1937) 541–550.

[229] E.W. Müller, J. Appl. Phys. 27 (1956) 474–476.

[230] J.A. Panitz, Rev. Sci. Instrum. 44 (1973) 1034–1038.

[231] A. Cerezo, T.J. Godfrey, G.D.W. Smith, Rev. Sci. Instrum. 59 (1988) 862–866.

[232] F. Danoix, F. Vurpillot, Chapter 3 - Basics of Field Ion Microscopy, Elsevier Inc., 2016.

[233] D. Blavette, X. Sauvage, Chapter 1 - Early Developments and Basic Concepts, Elsevier Inc., 2016.

[234] T.F. Kelly, P.P. Camus, D.J. Larson, L.M. Holzman, S.S. Bajikar, Ultramicroscopy 62 (1996) 29–42.

[235] T.F. Kelly, D.J. Larson, Mater. Charact. 44 (2000) 59–85.

[236] A. Vella, J. Houard, Chapter 8 - Laser-Assisted Field Evaporation, Elsevier Inc., 2016.

[237] G. Da Costa, Chapter 6 - Atom Probe Tomography: Detector Issues and Technology, Elsevier Inc., 2016.

[238] R.L. Smith, G.E. Sandly, Proc. Inst. Mech. Eng. 102 (1922) 623–641.

[239] A.P. Zhilyaev, T.G. Langdon, Prog. Mater. Sci. 53 (2008) 893–979.

[240] R.Z. Valiev, Y.V. Ivanisenko, E.F. Rauch, B. Baudelet, Acta Mater. 44 (1996) 4705–4712.

[241] S.M. Bruemmer, B.W. Arey, L.A. Charlot, Corrosion 48 (1992) 42–49.

[242] F.R. Beckitt, B.R. Clark, Acta Metall. 15 (1967) 113–129.

[243] L.K. Singhal, J.W. Martin, Acta Metall. 15 (1967) 1603–1610.

[244] H.U. Hong, B.S. Rho, S.W. Nam, Mater. Sci. Eng. A 318 (2001) 285–292.

[245] T. Thorvaldsson, G.L. Dunlop, J. Mater. Sci. 18 (1983) 793–803.

[246] K. Kaneko, T. Fukunaga, K. Yamada, N. Nakada, M. Kikuchi, Z. Saghi, J.S. Barnard, P.A. Midgley, Scr. Mater. 65 (2011) 509–512.

[247] N. Zhu, Y. He, W. Liu, L. Li, S. Huang, J. Vleugels, O. Van der Biest, J. Mater. Sci. Technol. 27 (2011) 725–728.

[248] L. Mújica Roncery, S. Weber, W. Theisen, Acta Mater. 59 (2011) 6275–6286.

[249] G.S. Was, R.M. Kruger, Acta Metall. 33 (1985) 841–854.

[250] A. Heczel, M. Kawasaki, J.L. Lábár, J. il Jang, T.G. Langdon, J. Gubicza, J. Alloys Compd. 711 (2017) 143–154.

[251] B.R. Pippan, F. Wetscher, M. Hafok, A. Vorhauer, (2006) 1046–1056.

[252] N. Hansen, R.F. Mehl, Metall. Mater. Trans. A Phys. Metall. Mater. Sci. 32 (2001) 2917–2935.

[253] R.Z. Valiev, R.K. Islamgaliev, I. V. Alexandrov, Prog. Mater. Sci. 45 (2000) 103–189.

[254] S.V. Zherebtsov, G.S. Dyakonov, A.A. Salem, V.I. Sokolenko, G.A. Salishchev, S.L. Semiatin, Acta Mater. 61 (2013) 1167–1178.

[255] S. Huang, W. Li, S. Lu, F. Tian, J. Shen, E. Holmström, L. Vitos, Scr. Mater. 108 (2015) 44–47.

[256] Y. Ikeda, I. Tanaka, J. Neugebauer, F. Körmann, Under Rev. Phys. Rev. Mater. 113603 (2019) 68–71.

[257] Y.Y. Shang, Y. Wu, J.Y. He, X.Y. Zhu, S.F. Liu, H.L. Huang, K. An, Y. Chen, S.H. Jiang, H. Wang, X.J. Liu, Z.P. Lu, Intermetallics 106 (2019) 77–87.

[258] X. Sauvage, A. Duchaussoy, G. Zaher, Mater. Trans. 60 (2019) 1151–1158.

[259] X. Sauvage, Y. Ivanisenko, J. Mater. Sci. 42 (2007) 1615–1621.

[260] X. Sauvage, G. Wilde, S.V. Divinski, Z. Horita, R.Z. Valiev, Mater. Sci. Eng. A 540 (2012) 1–12.

[261] D. Setman, E. Schafler, E. Korznikova, M.J. Zehetbauer, Mater. Sci. Eng. A 493 (2008) 116–122.

[262] A. V. Kazantzis, Z.G. Chen, J.T.M. De Hosson, J. Mater. Sci. 48 (2013) 7399–7408.

[263] M. Fiebig, Y. Tokura, T. Kimura, J.C. Lashley, a P. Ramirez, S. Park, Y.J. Choi, C.L. Zhang, T. Arima, H. Katsura, N. Nagaosa, a V Balatsky, I. a Sergienko, E. Dagotto, M. Mostovoy, a B. Harris, T. Yildirim, a Aharony, G. Lawes, N. Momozawa, Y. Yamaguchi, M. Mita, Y. Nagao, S. Utsumi, M. Abe, Science (80-.). (2008) 1646–1649.

[264] O. Renk, R. Pippan, Scr. Mater. 154 (2018) 212–215.

[265] O. Renk, P. Ghosh, R. Pippan, Scr. Mater. 137 (2017) 60–63.

[266] Y. Amouyal, S.V. Divinski, L. Klinger, E. Rabkin, Acta Mater. 56 (2008) 5500–5513.

[267] D.A. Hughes, N. Hansen, Acta Mater. 48 (2000) 2985–3004.

[268] R.A. Jago, N. Hansen, Acta Metall. 34 (1986) 1711–1720.

[269] Z. Wang, I. Baker, Z. Cai, S. Chen, J.D. Poplawsky, W. Guo, Acta Mater. 120 (2016) 228–239.

[270] I. Gutierrez-Urrutia, D. Raabe, Acta Mater. 60 (2012) 5791–5802.

[271] R. Pippan, S. Scheriau, A. Taylor, M. Hafok, A. Hohenwarter, A. Bachmaier, Annu. Rev. Mater. Res. 40 (2010) 319–343.

[272] T. Müller, M.W. Kapp, A. Bachmaier, P. Felfer, R. Pippan, Acta Mater. 166 (2019) 168–177.

[273] A. Pichler, E. Arzt, Acta Metall. Mater. 42 (1994) 3785–3800.

[274] G.R. Love, Acta Metall. 12 (1964) 731–737.

[275] K. Lu, C.F. Huo, Y. He, J. Yin, J. Liu, Q. Peng, W.P. Guo, Y. Yang, Y.W. Li, X.D. Wen, J. Phys. Chem. C 122 (2018) 23191–23199.

[276] I. V. Kireeva, Y.I. Chumlyakov, A. V. Vyrodova, Z. V. Pobedennaya, I. Karaman, Mater. Sci. Eng. A 784 (2020) 139315.

[277] W. Abuzaid, H. Sehitoglu, Mater. Charact. 129 (2017) 288–299.

[278] Q. Ding, H. Bei, X. Wei, Y. Gao, Z. Zhang, Mater. Today Nano 14 (2021) 100110.

[279] T.M. Smith, M.S. Hooshmand, B.D. Esser, F. Otto, D.W. McComb, E.P. George, M. Ghazisaeidi, M.J. Mills, Acta Mater. 110 (2016) 352–363.

[280] E. Castle, T. Csanádi, S. Grasso, J. Dusza, M. Reece, Sci. Rep. 8 (2018) 1–12.

[281] D.B. Williams, C.B. Carter, in: Transm. Electron Microsc., Springer US, Boston, MA, 1996, pp. 3–17.

[282] P. Bayliss, Can. Mineral. 28 (1990) 751–755.

[283] H. Okamoto, J. Phase Equilibria Diffus. 28 (2007) 406–407.

[284] V.E. Egorushkin, S.N. Kulkov, S.E. Kulkova, Phys. B+C 123 (1983) 61–68.

[285] F. Ye, Z. Jiao, Y. Yuan, Mater. Chem. Phys. 236 (2019) 121801.

[286] K. Cho, Y. Fujioka, T. Nagase, H.Y. Yasuda, Mater. Sci. Eng. A 735 (2018) 191–200.

[287] K.H. Lee, S.K. Hong, S.I. Hong, Materialia 8 (2019).

[288] X. Zhu, X. Zhou, S. Yu, C. Wei, J. Xu, Y. Wang, J. Magn. Magn. Mater. 430 (2017) 59–64.

[289] M. Klimova, D. Shaysultanov, A. Semenyuk, S. Zherebtsov, N. Stepanov, J. Alloys Compd. 851 (2021) 156839.

[290] O.A. Lukianova, V. Kulitckii, Z. Rao, Z. Li, G. Wilde, S. V. Divinski, Acta Mater. 237 (2022) 118136.

[291] J. PENG, Z. yong LI, X. bo JI, Y. le SUN, L. ming FU, A. dang SHAN, Trans. Nonferrous Met. Soc. China (English Ed. 30 (2020) 1884–1894.

[292] D. Gaertner, J. Kottke, Y. Chumlyakov, F. Hergemöller, G. Wilde, S. V. Divinski, Scr. Mater. 187 (2020) 57–62.

[293] M. Glienke, M. Vaidya, K. Gururaj, L. Daum, B. Tas, L. Rogal, K.G. Pradeep, S. V. Divinski, G. Wilde, Acta Mater. 195 (2020) 304–316.

[294] J. Gu, M. Song, Scr. Mater. 162 (2019) 345–349.

[295] B. Gludovatz, A. Hohenwarter, D. Catoor, E.H. Chang, E.P. George, R.O. Ritchie, Science (80-.). 345 (2014) 1153–1158.

[296] B.A. Sun, W.H. Wang, Prog. Mater. Sci. 74 (2015) 211–307.

[297] M.M. Trexler, N.N. Thadhani, Prog. Mater. Sci. 55 (2010) 759–839.

[298] G.I. Taylor, Proc. R. Soc. London. Ser. A, Contain. Pap. a Math. Phys. Character 145 (1934) 388–404.

[299] C. Zhu, Z.P. Lu, T.G. Nieh, Acta Mater. 61 (2013) 2993–3001.

[300] W.F. Hosford, Mechanical Behavior of Materials, Cambridge University Press, 2005.

[301] K. Jin, Y.F. Gao, H. Bei, Mater. Sci. Eng. A 695 (2017) 74–79.

[302] Z. Wu, Y. Gao, H. Bei, Acta Mater. 120 (2016) 108–119.

[303] J. Hu, Y.N. Shi, X. Sauvage, G. Sha, K. Lu, Science (80-.). 355 (2017) 1292–1296.

[304] M.M. Abramova, N.A. Enikeev, R.Z. Valiev, A. Etienne, B. Radiguet, Y. Ivanisenko, X. Sauvage, Mater. Lett. 136 (2014) 349–352.

[305] W. Xu, X.C. Liu, X.Y. Li, K. Lu, Acta Mater. 182 (2020) 207–214.

[306] S. V. Bobylev, N.A. Enikeev, A.G. Sheinerman, R.Z. Valiev, Int. J. Plast. 123 (2019) 133–144.

[307] J. Schioøtz, K.W. Jacobsen, Science (80-.). 301 (2003) 1357–1359.

[308] S. Takeuchi, Scr. Mater. 44 (2001) 1483–1487.

[309] A.H. Chokshi, A. Rosen, J. Karch, H. Gleiter, Scr. Metall. 23 (1989) 1679–1683.

[310] L. Zhang, Y. Shibuta, Mater. Lett. 274 (2020) 128024.

[311] M. V. Klimova, D.G. Shaysultanov, R.S. Chernichenko, V.N. Sanin, N.D. Stepanov, S. V. Zherebtsov, A.N. Belyakov, Mater. Sci. Eng. A 740–741 (2019) 201–210.

[312] H. Hahn, P. Mondal, K.A. Padmanabhan, Nanostructured Mater. 9 (1997) 603–606.

[313] S.J. Sun, Y.Z. Tian, H.R. Lin, H.J. Yang, X.G. Dong, Y.H. Wang, Z.F. Zhang, Mater. Sci. Eng. A 712 (2018) 603–607.

[314] D.T. Pierce, J.A. Jiménez, J. Bentley, D. Raabe, C. Oskay, J.E. Wittig, Acta Mater. 68 (2014) 238–253.

[315] E.D. HONDROS, M.R. SEAH, S. HOFMANN, P. LEJČEK, in: Phys. Metall., Elsevier, 1996, pp. 1201–1289.

[316] L.A. Deibler, J.J. Lewandowski, Mater. Sci. Eng. A 527 (2010) 2207–2213.

[317] P.S. Steif, F. Spaepen, J.W. Hutchinson, Acta Metall. 30 (1982) 447–455.

[318] C.A. Schuh, T.C. Hufnagel, U. Ramamurty, Acta Mater. 55 (2007) 4067–4109.

[319] D. Suh, R.H. Dauskardt, J. Non. Cryst. Solids 317 (2003) 181–186.

[320] P. Murali, U. Ramamurty, Acta Mater. 53 (2005) 1467–1478.

[321] I. Semenova, G. Salimgareeva, G. Da Costa, W. Lefebvre, R. Valiev, Adv. Eng. Mater. 12 (2010) 803–807.

[322] O. Renk, A. Hohenwarter, K. Eder, K.S. Kormout, J.M. Cairney, R. Pippan, Scr. Mater. 95 (2015) 27–30.

[323] S. Praveen, J.W. Bae, P. Asghari-Rad, J.M. Park, H.S. Kim, Mater. Sci. Eng. A 734 (2018) 338–340.

[324] G. Krauss, Mater. Sci. Eng. A 273–275 (1999) 40–57.

[325] H.T. Wang, N.R. Tao, K. Lu, Acta Mater. 60 (2012) 4027–4040.

[326] J. Zhang, D. Raabe, C.C. Tasan, Acta Mater. 141 (2017) 374–387.

[327] C. Chen, J. Wang, Y. Ge, L. Ma, Coatings 12 (2022).

Curriculum Vitae

Personal Information:

Name: Yemao Lu

Date of Birth: August 17, 1992

Place of Birth: Hubei, China

Nationality: P.R. China

Education:

- **Ph.D.** in Materials Science 10.2018 - 05.2023
  Technical University of Darmstadt, Darmstadt, Germany

- **Master of Engineering** in Materials Science and Engineering 09.2015 - 06.2018
  College of Materials and Metallurgy, Guizhou University, Guiyang, China

- **Bachelor of Engineering** in Material Chemistry 09.2010 - 06.2014
  Nanchang Hangkong University, Nanchang, China

List publications

1. **Yemao Lu**, Andrey Mazilkin, Torben Boll, Nikita Stepanov, Sergei Zherebtzov, Gennady Salishchev, Éva Ódor, Tamas Ungar, Enrique Lavernia, Horst Hahn, Yulia Ivanisenko. Influence of carbon on the mechanical behavior and microstructure evolution of CoCrFeMnNi processed by high pressure torsion. *Materialia,* 2021, 16: 101059. doi.org/10.1016/j.mtla.2021.101059.
2. **Yemao Lu**, Horst Hahn, Yulia Ivanisenko. Carbon segregation in CoCrFeMnNi high entropy alloy driven by high pressure torsion at room and cryogenic temperature. *Advanced Engineering Materials*, 2023, 23(9): 2201473. doi.org/10.1002/adem.202201473.
3. **Yemao Lu**, Horst Hahn, Yulia Ivanisenko. Thermal stability and mechanical properties of nanocrystalline carbon alloyed high entropy alloy. (in submission)
4. Zhenfei Jiang, Weiping Chen, Chenliang Chu, Zhiqiang Fu, Julia Ivanisenko, Hao Wang, Siyuan Peng, **Yemao Lu**, Enrique J. Lavernia, Horst Hahn. Directly cast fibrous heterostructured FeNi0.9Cr0.5Al0.4 high entropy alloy with low-cost and remarkable tensile properties. *Scripta Materialia*, 2023, 230: 115421. doi.org/10.1016/j.scriptamat.2023.115421.
5. Zhenfei Jiang, Weiping Chen, Junchen Liu, **Yemao Lu**, Chenliang Chu, Siyuan Peng, Zhiqiang Fu, Yulia Ivanisenko. Lamellar-structured low-cost FeMn0.7Ni0.6Cr0.4Al0.3 high entropy alloy with excellent tensile properties. *Vacuum*, 2023, 209: 111767. doi.org/10.1016/j.vacuum.2022.111767.
6. Michael K. Eusterholz, Torben Boll, Vincent Ott, Michael Stüber, **Yemao Lu**, Julian Gebauer, Sven Ulrich, Hans Jürgen Seifert, Alexander Kauffmann, Martin Heilmaier. Nanoscale oxide formation at α-Al2O3 – Nb layer composite interfaces. *Advanced Engineering Materials*, 2023: 2201441. doi.org/10.1002/adem.202201441.
7. Bo Lin, Xiangxiang He, Yuliang Zhao, Rui Xu, **Yemao Lu**. Evolution of Iron-Rich Intermetallics and its Effect on the Mechanical Properties of Al-Cu-Mn-Fe-Si Alloys after Thermal Exposure and High-Temperature Tensile Testing. *Journal of Materials Research and Technology*, 2023, 23: 2527-2541. doi.org/10.1016/j.jmrt.2023.01.172.

Acknowledgements

How Time flies! It has been almost four and half years since I came to Karlsruhe, Germany. I would like to appreciate a lot of people who helped, supported and encouraged me during the entire Ph.D. studies.

Firstly, I would like to thank my supervisor Prof. Horst Hahn who provided the opportunity to be a Ph.D candidate in Technische Universität Darmstadt and work at Institut für Nanotechnologie, Karlsruher Institut für Technologie. He provided me with helpful advice, support and guidance which enabled me to solve many scientific problems in researches.

I would like to express my greatest thanks to my daily superior Dr. Julia Ivanisenko, who is leading me to the way of scientific research. Her optimistic and friendly attitude towards life has created a pleasant and comfortable research environment for me during my PhD period. Her patient and positive attitude towards scientific research would benefit me during all my life. Without her help and encourage in researches, I would not have finished this dissertation. Without her concern in the life, I would not have overcome obstacles in daily life.

I would like to thank Prof. Christian Kübel and the members of the electron microscopy & spectroscopy group (EMSG) for their help and advices. Owing to their support in TEM, I learnt a lot of in the field of electron microscopies, which is really beneficial to me for a long term.

I would like to thank Dr. Torben Boll and the members of atom probe tomography group for their assistance of APT measurements. Also, I would also like to thank Dr. Xavier Sauvage for the discussion of APT results and Le Groupe de Physique des Matériaux (GPM) for opening the door of APT for me. I would like to thank Prof. Tamás Ungár for the help of X-ray line profile analysis in this dissertation.

I am very grateful to Dr. Chujun Zhang. We have been well acquainted, known, and accompanied by each other since high school. Without out her encouragement, accompanying and love, I cannot make it in past decade. Hope we can continue walking hand in hand for the rest of life and greet the new starting point soon.

Besides, I would like to thank the China Scholarship Council (CSC) for the financial support during my Ph.D research in Germany. And I'm also thankful to my friends, Rui, Miao, and members of BAV (bav-alpine.com) for bringing me a lot of fun in the past years.

最后，我想感谢我的父母、姐姐和亲人们。有你们的背后支持和鼓励，我才能顺利完成博士工作成功毕业，长期的分别是为了迎接更美好的重逢。

记于 2022-12-12,壬寅年冬月十九, Stutensee, 76297.